DESY-THESIS-2002-026
July 2002

Absolute Calibration of a Polarized Deuterium Gas Target

by

M. Henoch

ISSN 1435-8085

Absolute Calibration of a Polarized Deuterium Gas Target

Den Naturwissenschaftlichen Fakultäten

der Friedrich-Alexander-Universität Erlangen-Nürnberg

zur

Erlangung des Doktorgrades

vorgelegt von

Mark Henoch

aus

Hagen

Als Dissertation genehmigt von den Naturwissenschaftlichen Fakultäten der Universität Erlangen-Nürnberg

Tag der mündlichen Prüfung: 17. Juli 2002

Vorsitzender der Promotionskommission: Prof. Dr. A. Magerl

Erstberichterstatter: Prof. Dr. E. Steffens

Zweitberichterstatter: Prof Dr. G. Graw

Now focus your mind vigorously on this paragraph and on all its words. What's so unusual about it? Don't just zip through it quickly. Go through it slowly. Tax your brain as much as you can.

Contents

Chapter 1

Introduction

1.1 Spin Structure of the Nucleon

During the last years many physics experiments using deep inelastic lepton-nucleon scattering were carried out to increase the understanding of the spin structure of the nucleon. In 1974 J. Ellis and R. Jaffe derived separated sum rules for proton and neutron from the Bjorken sum rule [Bjo 66, Bjo 70] by comparing the beta decays of Ξ^- and neutron with the assumptions of an unpolarized strange quark sea ($\Delta s = 0$) and fulfilled SU(3) flavour symmetry [Ell 74]:

$$\Gamma_1^p(Q^2) = \int_0^1 g_1^p(x, Q^2)\mathrm{d}x = 0.160 \pm 0.006 \tag{1.1}$$

$$\Gamma_1^n(Q^2) = \int_0^1 g_1^n(x, Q^2)\mathrm{d}x = -0.021 \pm 0.018\,, \tag{1.2}$$

where $g_1(x, Q^2)$ is one of the most studied spin structure functions which can be interpreted in the parton model by superimposing the quark distributions $q_f^+(x, Q^2)$ and $q_f^-(x, Q^2)$ and summing over all flavours f:

$$g_1(x, Q^2) = \frac{1}{2}\sum_f e_f^2[q_f^+(x, Q^2) - q_f^-(x, Q^2)] = \frac{1}{2}\sum_f e_f^2[\Delta q_f(x, Q^2)]\ . \tag{1.3}$$

Q^2 is the negative square of the invariant mass of the exchanged virtual photon during the scattering process and with the mass of the nucleon M and an energy tranfer of ν, x is defined as $x = Q^2/2M\nu$ and called the Bjoerken skaling variable. The values for $\Gamma_1^p(Q^2)$ and $\Gamma_1^n(Q^2)$ have been taken from [E143 95] and [E142 93].

A violation of the sum rule for protons (1.1) has been found in an experiment with access to $0.01 < x < 0.1$ by the European Muon Collaboration (EMC) in 1988 with a significance of two standard deviations [EMC 88, EMC 89]. This result initiated further experiments to prove the violation and finally understand the different contributions to the nucleons spin. EMC was

followed by SMC (Spin Muon Collaboration) [SMC 94a, SMC 97a] and other experiments have been carried out at SLAC [E142 93, E143 95, E154 97, E155 98] all using external polarized targets. Their results were all consistent with the violation of the Ellis-Jaffe sum rule.
Another important structure function is $g_2(x, Q^2)$ that can be measured using a transversally polarized target. The sum rule to this structure function has been derived by H. Burkhardt and W.N. Cottingham [Bur 70]:

$$\Gamma_2 = \int_0^1 g_2(x, Q^2)\mathrm{d}x = 0. \tag{1.4}$$

Experimental results confirming this sum rule have been published by SMC [SMC 94b].

1.2 The HERMES Experiment

The HERMES (HERa MEasurement of Spin) experiment [HER 90, HER 93] extends the results of EMC, SMC and SLAC using a polarized hydrogen and deuterium gas target internal to the HERA electron storage ring. In this way the usable beam current is a lot higher but also the thickness of the target is lower so that the total luminosity is comparable to that of experiments using an external target. A major advantage of this gaseous target type is the fact that the target polarization is not diluted by other unpolarized nuclei. The polarized hydrogen and deuterium gas target of HERMES will be explained in more detail in chapter 1.3. This technique is also used by other recent experiments at IUCF [Rat 98, Prz 98, Mey 98] and at COSY [Alb 97].
The HERMES experiment is located in the eastern straight section of the HERA storage ring at DESY in Hamburg (see figure 1.1). Via deep-inelastic scattering of polarized positrons and electrons at 27.5 GeV impinging on the polarized nucleons of the internal gas targets using hydrogen and deuterium gas, HERMES studies the spin structure of the proton and the neutron. Besides the possibility to detect and identify the scattered lepton (*inclusive* physics) the HERMES spectrometer [HER 98a] allows the additional identification of hadronic scattering

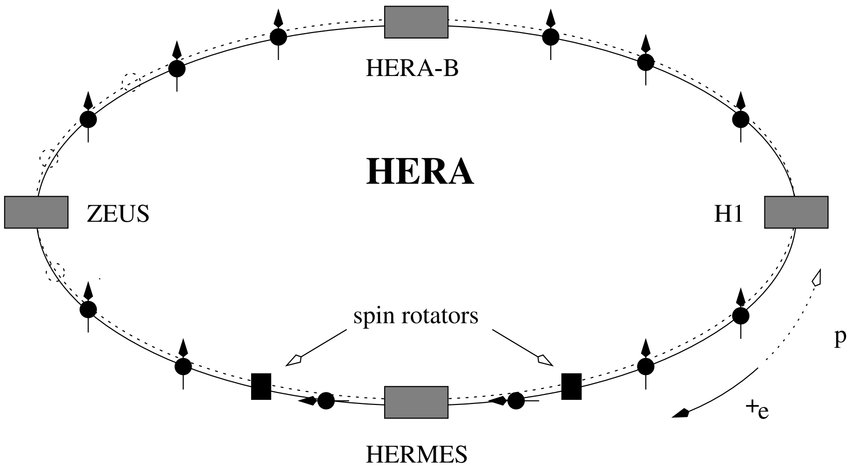

Figure 1.1: Scheme of the HERA ring with its four experiments at DESY. North is to the right of this picture. The electrons or positrons are accelerated clockwise, the protons counterclockwise.

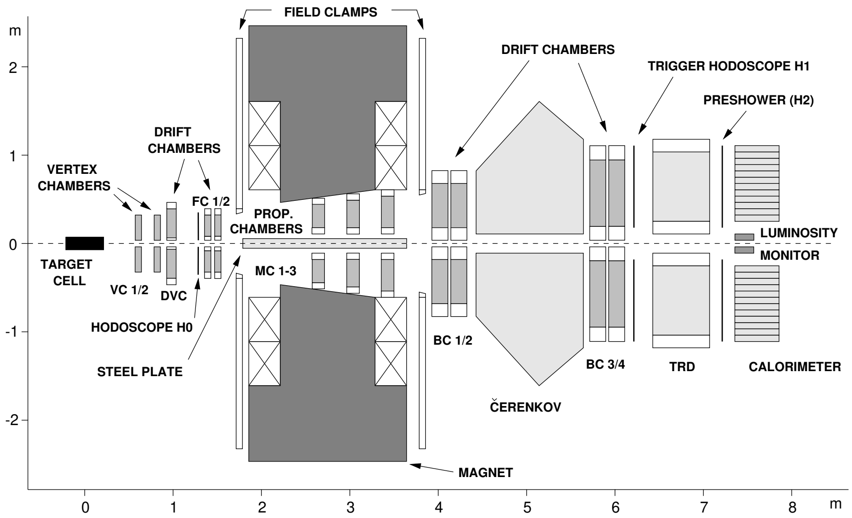

Figure 1.2: Schematic side view of the HERMES experiment. The target section is on the left. The HERA electron/positron beam passes HERMES from the left to the right.

products in coincidence with the scattered lepton (*semi-inclusive* physics). Using both polarized and unpolarized targets, the semi-inclusive physics measurements are the central item of the HERMES physics program.

The detector used at HERMES as shown in figure 1.2 is an open-geometry forward spectrometer. The momentum of a particle can be obtained by a tracking system consisting of drift chambers in front and behind the spectrometer magnet. The identification of the particles is provided by a lead-glass calorimeter, a pre-shower detector, a transition radiation detector (TRD) and a ring imaging cherenkov detector (RICH) that can distuinguish between protons, pions and kaons.

The electrons/positrons of the HERA storage ring are transversally polarized by the Sokolov-Ternov effect [Sok 64]. To provide the needed longitudinally polarized beam a set of spin rotators have been installed before and after the HERMES section of HERA. A longitudinal polarimeter (LPOL) near the HERMES experiment as well as a transversal polarimeter (TPOL) in the west section of HERA are used to measure the beam polarization [Bar 93, Bar 94, Lor 97].

1.3 The Polarized HERMES Gas Target

The HERMES polarized hydrogen and deuterium target as shown in figure 1.3 consists of an atomic beam source (ABS), which injects a spin polarized beam of hydrogen or deuterium atoms into a thin walled storage cell, a Breit-Rabi polarimeter (BRP) to measure the atomic polarization and a target gas analyzer (TGA) to determine the atomic fraction. Due to the storage cell, the atoms remain in the interaction area for two orders of magnitude longer than compared to a free jet target. The nucleon density is increased by the same factor. A drawback of using a storage cell is that the atoms now interact with the storage cell wall and may collide with other atoms in the gas phase. During such an interaction the atom may depolarize or recombine to a gas molecule. The temperature of the storage cell and the magnetic holding field are chosen

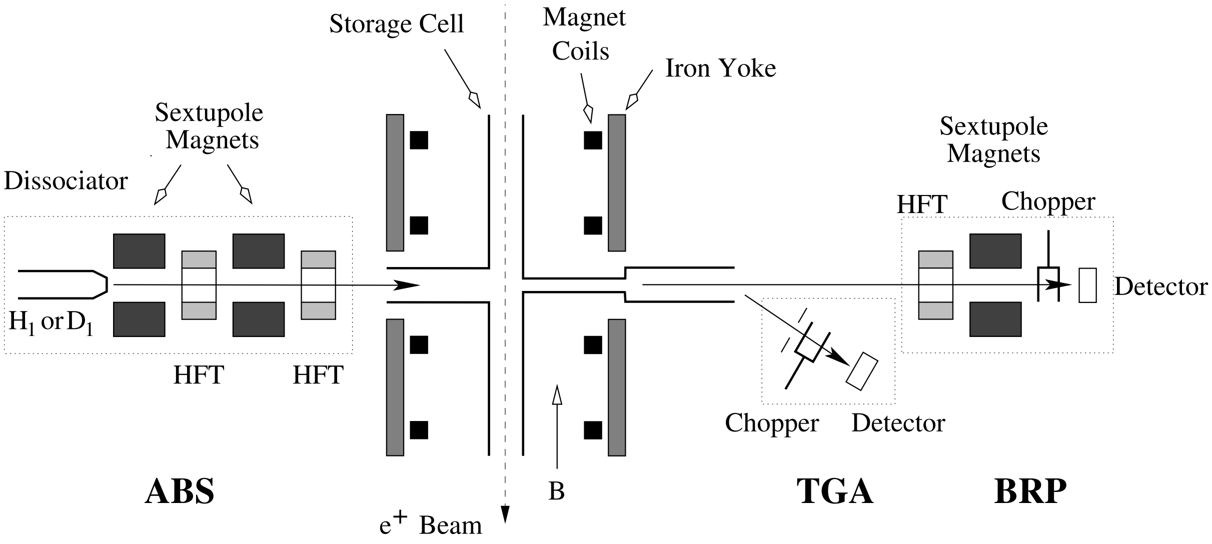

Figure 1.3: Schematic top view of the HERMES target. Hydrogen or deuterium gas is dissociated and polarized in the atomic beam source (ABS) before being injected into the storage cell which is surrounded by a magnet. The target gas is sampled and analyzed by means of a target gas analyzer (TGA) and a Breit-Rabi polarimeter (BRP).

such as to minimize the recombination and depolarization effects. The magnetic holding field of up to 350 mT also defines the quantization axis for the spins and is required to achieve high polarization of the mixed hyperfine states. Until the end of 2000 a longitudinal holding field provided by a superconducting magnet was used whereas since 2001 a conventional magnet providing a transversal magnetic holding field has been installed.

The target storage cell is an open-ended 400 mm long tube with an elliptical cross section of 21×8.9 mm^2 and is made of 75 μm thin aluminum foil coated with Drifilm [Tho 87, Swe 88]. Two side tubes are mounted to the center of the storage cell, one for the injection of atoms by the ABS and the other to extract a sample of the target gas to be analyzed by the BRP and the TGA. The cell is supported by aluminum rails which can be cooled by gaseous helium.

In the ABS the gaseous hydrogen and deuterium molecules are dissociated using a radio frequency dissociator[1]. The atoms are then electron polarized by means of Stern-Gerlach spin separation where atoms with $m_s = +\frac{1}{2}$ are focussed into the opening of the injection tube by a system of sextupole magnets, and atoms with $m_s = -\frac{1}{2}$ are defocussed and pumped away. Several adiabatic high frequency transition (HFT) units [Abr 58] are used to transfer the polarization of the electron spin to the nuclear spin by a selected exchange of the populations of two hyperfine states.

[1]In December 1999 the rf-dissociator has been replaced by a recently developed surfatron based microwave dissociator[Koc 99].

The TGA consists of a chopper, a cross beam ionizer and a quadrupole mass spectrometer (QMS) with a channeltron for single ion detection. The measurement of the relative amount of atoms and molecules in the sample beam is used to determine the atomic fraction inside the storage cell needed for the calculation of the target polarization.
The BRP is used to determine the hyperfine state population of the sample beam which is then related to the atomic polarization inside the storage cell. The detector of the BRP is similar to that of the TGA. Before the sample beam enters the BRP detector it passes two adiabatic HFT units and a sextupole magnet system. Switching the HFT units allows to select atoms in different combinations of hyperfine states to pass the sextupole spin selector. A set of at least four (six) measurements with different HFT settings is required to determine the hyperfine state population of the hydrogen (deuterium) atoms in the sample beam.

1.4 Target Polarization

The average polarization P^T of nucleons in the target can be calculated using the results of the measurements of the TGA and the BRP. P^T has contributions from polarized atoms (P_a) and polarized molecules (P_m) if two polarized atoms recombine to a molecule. Nucleons that enter the storage cell as molecules are unpolarized. If n_a is the number of atoms inside the storage cell and n_m the number of molecules, the fraction of nucleons in the atomic state (also called the degree of dissociation) α is defined by

$$\alpha = \frac{n_a}{n_a + 2n_m} = \frac{\rho_a}{\rho_a + \sqrt{2}\rho_m} \ , \tag{1.5}$$

where $\rho_{a,m}$ denote the normalized atomic and molecular densities. With α_0 representing the initial fraction of nucleons in atoms as injected by the ABS and α_r denoting the fraction of nucleons in atoms surviving recombination during their way through the storage cell, P^T can be calculated by

$$P^T = \alpha_0 \cdot (\alpha_r + (1 - \alpha_r) \cdot \beta) \cdot P_a \ , \tag{1.6}$$

where β stands for the ratio of the polarization of the molecules produced by recombination P_m relative to the polarization of the atoms P_a. The knowledge of β for the experimental conditions at the HERMES experiment will be discussed in chapter 6.2.
The values for α_0, α_r and P_a are calculated using the measurements of the TGA and the BRP. As both detectors measure properties of a sample of the target gas it is necessary to relate the results to a corresponding value averaged along the storage cell. This is achieved by the sampling corrections c_α

$$\alpha_r = c_\alpha \cdot \alpha_r^{TGA} \ , \tag{1.7}$$

and c_p

$$P_a = c_p \cdot P_a^{BRP} \ . \tag{1.8}$$

These sampling corrections and their systematic uncertainties are a function of the measured values of α_r^{TGA} and P_a^{BRP} themself. The functions depend on the geometry of the storage cell, its surface properties and the geometry of the detectors. They are calculated with the help of simulations of the path of the particles through the storage cell, where the history of these particles is stored and analyzed. Another possiblity to calculate sampling corrections analytically is to describe the diffusion process of the target gas inside the storage cell with the help of the one-dimensional diffusion equation. Both methods will be discussed in chapter 5.

Chapter 2

Hyperfine Splitting and Applications in the HERMES Target

2.1 Hyperfine Structure of Hydrogen/Deuterium

The total angular momentum $\vec{F}$ of an atom is the sum of the electron spin $\vec{S}$, the nuclear spin $\vec{I}$ and the orbital angular momentum of the electron. For hydrogen and deuterium atoms in the ground state (1s) the orbital angular momentum is zero as the spin of the nucleus couples directly with the magnetic moment of the electron. The differences in energy of the two states of hydrogen and deuterium atoms with a different $\vec{F}$ are called the hyperfine splitting energy $E_{HFS}^{(H)}$ and $E_{HFS}^{(D)}$. The corresponding transition frequency has been measured very precisely using a maser [Hel 70, Dym 92, Aud 71] to be

$$\nu_{HFS}^{(H)} = 1\,420\,405\,751.768(1) \text{ Hz and} \tag{2.1}$$

$$\nu_{HFS}^{(D)} = 327\,384\,352.51(1) \text{ Hz} . \tag{2.2}$$

An external magnetic field $B = |\vec{B}| = B_z$ cancels the degeneration of the states with $F \neq 0$ (with F being the quantum number of $\vec{F}$ with respect to the quantization axis) as the spins of electron and nucleus are interacting with the external field also. After introducing the Larmor frequency of the electron as

$$\omega_S = \frac{g_S \mu_B}{\hbar} B \tag{2.3}$$

with g_S being the gyromagnetic factor of the electron and the Bohr magneton μ_B, the critical magnetic field B_c is defined by

$$\hbar\omega_S = E_{HFS} = 2\pi\hbar \cdot \nu_{HFS} \tag{2.4}$$

which leads in combination with (2.3) to

$$B_c = \frac{E_{HFS}}{g_S \mu_B} . \tag{2.5}$$

The critical field for hydrogen is $B_c^H \approx 50.7$ mT and for deuterium $B_c^D \approx 11.7$ mT. The ratio of the external field and the critical field defines x:

$$x = \frac{B}{B_c} \ . \tag{2.6}$$

The interaction of the magnetic moments with an external magnetic field and the coupling of the spins of electron and nucleus can be described by the Hamilton operator

$$\mathcal{H} = \mathcal{A}_{H,D}\vec{I}\cdot\vec{S} + \frac{g_S\mu_B}{\hbar}S_zB_z - \frac{g_I\mu_N}{\hbar}I_zB_z \ . \tag{2.7}$$

The first term with the constant $\mathcal{A}_{H,D}$[Coh 77] describes the coupling between $\vec{S}$ and $\vec{I}$ for hydrogen and deuterium respectively, the second term deals with the interaction of the electron spin with the external magnetic field whereas the third part, in which g_I is the gyromagnetic factor of the nucleus and μ_N is the nuclear magneton, describes the interaction of the nuclear spin with the external magnetic field.
Disregarding the effect of the nuclear spin coupling to the external magnetic field by neglecting the third term in equation (2.7) due to the small size of the nuclear magneton μ_N for magnetic holding fields up to $B \approx 30$ T the Hamilton operator simplifies to

$$\mathcal{H} = \mathcal{A}_{H,D}\vec{I}\cdot\vec{S} + \omega_S S_z \ . \tag{2.8}$$

One can find a basis for the Hamilton operator using the product wave functions $|\uparrow +\rangle$, $|\uparrow -\rangle$, $|\downarrow +\rangle$, $|\downarrow -\rangle$ for hydrogen and $|\uparrow +\rangle$, $|\uparrow 0\rangle$, $|\uparrow -\rangle$, $|\downarrow +\rangle$, $|\downarrow 0\rangle$, $|\downarrow -\rangle$ for deuterium, where the arrows refer to the magnetic quantum number of the electron spin m_S and the nuclear spin is represented by the sign of its magnetic quantum number m_I. Making use of the identity

$$\vec{I}\cdot\vec{S} = I_zS_z + \frac{1}{2}(I_+S_- + I_-S_+) \ , \tag{2.9}$$

where $I_\pm = I_x \pm iI_y$ and $S_\pm = S_x \pm iS_y$, one can then find eigenvectors end eigenvalues of $\mathcal{H}$ by an orthogonal transformation represented by the matrix U_0

$$U_0^H = \begin{pmatrix} 1 & 0 & 0 & 0 \\ 0 & \cos\theta & 0 & -\sin\theta \\ 0 & 0 & 1 & 0 \\ 0 & \sin\theta & 0 & \cos\theta \end{pmatrix}, \ U_0^D = \begin{pmatrix} 1 & 0 & 0 & 0 & 0 & 0 \\ 0 & \cos\theta_+ & 0 & 0 & 0 & -\sin\theta_+ \\ 0 & 0 & \cos\theta_- & 0 & -\sin\theta_- & 0 \\ 0 & 0 & 0 & 1 & 0 & 0 \\ 0 & 0 & \sin\theta_- & 0 & \cos\theta_- & 0 \\ 0 & \sin\theta_+ & 0 & 0 & 0 & \cos\theta_+ \end{pmatrix} \tag{2.10}$$

with the mixing angles θ and $\theta_\pm$ defined by

$$\tan 2\theta = \frac{1}{x} \qquad \text{and} \qquad \tan 2\theta_\pm = \frac{\sqrt{8}}{3x \pm 1} \ . \tag{2.11}$$

The new basis of the Hamilton operator is called the Breit-Rabi basis and consists of the eigenvectors of $\mathcal{H}$. For hydrogen they are given by

$$\begin{aligned}
|\,1\,\rangle^H &= |\uparrow +\rangle \\
|\,2\,\rangle^H &= \cos\theta\,|\uparrow -\rangle + \sin\theta\,|\downarrow +\rangle \\
|\,3\,\rangle^H &= |\downarrow -\rangle \\
|\,4\,\rangle^H &= -\sin\theta\,|\uparrow -\rangle + \cos\theta\,|\downarrow +\rangle
\end{aligned} \tag{2.12}$$

and for deuterium they are

$$\begin{aligned}
|\,1\,\rangle^D &= |\uparrow +\rangle \\
|\,2\,\rangle^D &= \cos\theta_+\,|\uparrow 0\,\rangle + \sin\theta_+\,|\downarrow +\rangle \\
|\,3\,\rangle^D &= \cos\theta_-\,|\uparrow -\rangle + \sin\theta_-\,|\downarrow 0\,\rangle \\
|\,4\,\rangle^D &= |\downarrow -\rangle \\
|\,5\,\rangle^D &= -\sin\theta_-\,|\uparrow -\rangle + \cos\theta_-\,|\downarrow 0\,\rangle \\
|\,6\,\rangle^D &= -\sin\theta_+\,|\uparrow 0\,\rangle + \cos\theta_+\,|\downarrow +\rangle \ .
\end{aligned} \tag{2.13}$$

The behaviour of the corresponding eigenvalues depending on an external magnetic field is shown in 2.1. For hydrogen these eigenvalues are given by

$$\begin{aligned}
E_1^H &= E_{HFS}^H \cdot \left(\tfrac{1}{4} + \tfrac{1}{2}x\right) \\
E_2^H &= E_{HFS}^H \cdot \left(-\tfrac{1}{4} + \tfrac{1}{2}\sqrt{x^2+1}\right) \\
E_3^H &= E_{HFS}^H \cdot \left(\tfrac{1}{4} - \tfrac{1}{2}x\right) \\
E_4^H &= E_{HFS}^H \cdot \left(-\tfrac{1}{4} - \tfrac{1}{2}\sqrt{x^2+1}\right)
\end{aligned} \tag{2.14}$$

and for deuterium one finds

$$\begin{aligned}
E_1^D &= E_{HFS}^D \cdot \left(\tfrac{1}{3} + \tfrac{1}{2}x\right) \\
E_2^D &= E_{HFS}^D \cdot \left(-\tfrac{1}{6} + \tfrac{1}{2}\sqrt{x^2+\tfrac{2}{3}x+1}\right) \\
E_3^D &= E_{HFS}^D \cdot \left(-\tfrac{1}{6} + \tfrac{1}{2}\sqrt{x^2-\tfrac{2}{3}x+1}\right) \\
E_4^D &= E_{HFS}^D \cdot \left(\tfrac{1}{3} - \tfrac{1}{2}x\right) \\
E_5^D &= E_{HFS}^D \cdot \left(-\tfrac{1}{6} - \tfrac{1}{2}\sqrt{x^2-\tfrac{2}{3}x+1}\right) \\
E_6^D &= E_{HFS}^D \cdot \left(-\tfrac{1}{6} - \tfrac{1}{2}\sqrt{x^2+\tfrac{2}{3}x+1}\right) \ .
\end{aligned} \tag{2.15}$$

A more general solution of the Hamilton operator (2.7) without neglecting the interaction of the nuclear spin and the external magnetic field can be found in [Bau 00].

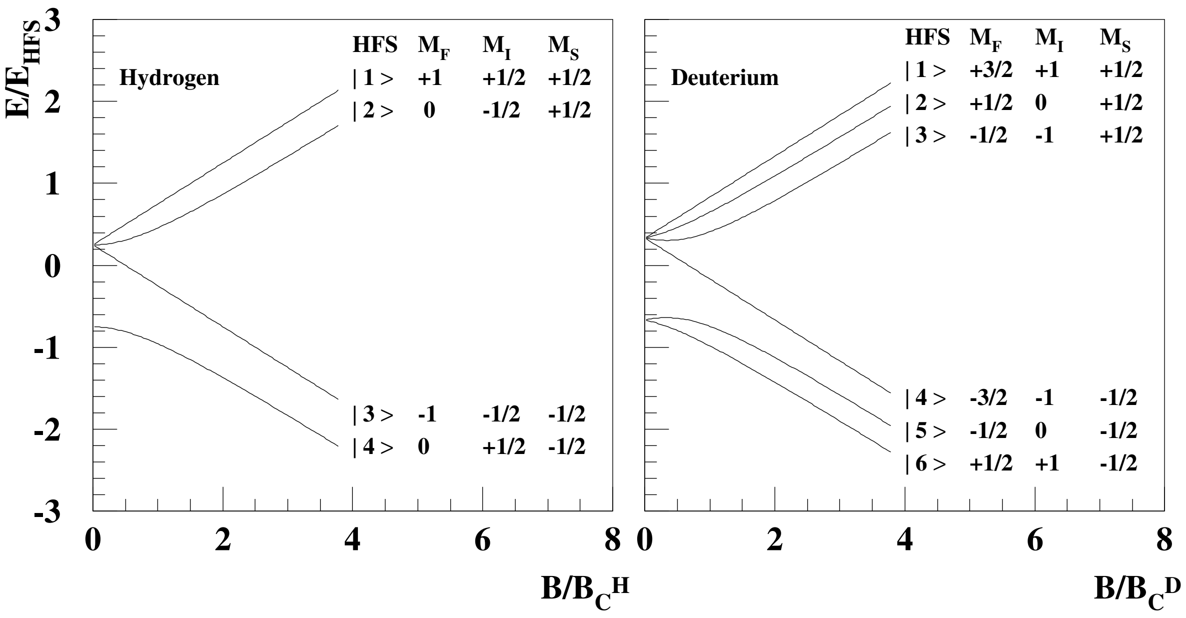

Figure 2.1: The hyperfine energy levels of hydrogen (left) and deuterium (right) atoms as a function of the magnetic holding field (Breit-Rabi diagram). The field values are scaled with the corresponding critical field B_c and the energy values with the corresponding hyperfine energy E_{HFS}.

The polarization of the electrons P_e and nucleons P_z of any of the states in equations (2.12) and (2.13) is given by the normalized expectation values of the operators S_z and I_z respectively. In a gas sample with known hyperfine population numbers N_i, which represent the probablities of an atom to be in state $|\, i\, \rangle$, the polarization values for hydrogen can be calculated by

$$\begin{aligned} P_e &= N_1 - N_3 + (N_2 - N_4)\cos 2\theta \\ P_z &= N_1 - N_3 - (N_2 - N_4)\cos 2\theta \ . \end{aligned} \tag{2.16}$$

In case of deuterium another value is needed to completely characterize the atom's polarization. An often used possibility is the tensor polarization P_{zz}, which is defined as the zz component of the tensor operator $I_{ij} = \frac{3}{2}(I_i I_j + I_j I_i) - 2\delta_{ij}$ [God 58]:

$$P_{zz} = \langle\, I_{zz}\, \rangle = \left\langle\, 3I_z^2 - 2\, \right\rangle \ . \tag{2.17}$$

Hence the calculation of the polarizations for deuterium yields analogous to (2.16)

$$\begin{aligned}
P_e &= N_1 - N_4 + (N_2 - N_6)\cos 2\theta_+ + (N_3 - N_5)\cos 2\theta_- \\
P_z &= N_1 + N_6 - N_3 - N_4 + (N_2 - N_6)\sin^2\theta_+ + (N_3 - N_5)\sin^2\theta_- \\
P_{zz} &= N_1 + N_4 - N_2 \cdot \tfrac{1}{2}(3\cos 2\theta_+ + 1) + N_3 \cdot \tfrac{1}{2}(3\cos 2\theta_- - 1) \\
&\quad - N_5 \cdot \tfrac{1}{2}(3\cos 2\theta_- + 1) + N_6 \cdot \tfrac{1}{2}(3\cos 2\theta_+ - 1)\ .
\end{aligned} \tag{2.18}$$

Quantifying the relative orientation of the spins of the electron and nucleon can be done by defining the asymmetry A_{IS} in case of hydrogen by

$$A_{IS}^H = \frac{4}{\hbar^2}\left\langle \vec{I}\vec{S} \right\rangle = N_1 + N_3 - N_2 - N_4 + (N_2 - N_4)2\sin 2\theta\ , \tag{2.19}$$

and in case of deuterium by

$$\begin{aligned}
A_{IS}^D = \tfrac{2}{\hbar^2}\left\langle \vec{I}\vec{S} \right\rangle = &\ N_1 + N_4 - N_3 - N_6 - (N_2 - N_6)(\sin^2\theta_+ - \sqrt{2}\sin 2\theta_+) \\
&+ (N_3 - N_5)(\sin^2\theta_- + \sqrt{2}\sin 2\theta_-)\ .
\end{aligned} \tag{2.20}$$

2.2 Hyperfine Transitions

Transitions between certain hyperfine states are playing a central role in polarized target physics as a change in the hyperfine population will also change the polarization of the target gas as seen in equations (2.16) and (2.18) respectively. They are both important to either polarize the target gas by using adiabatic high frequency transition (HFT) units [Abr 58, Hae 67, Phi 87, Oh 70] in the ABS[1] or to cause depolarization during wall collisions [Bou 65] and by resonant depolarization induced by the bunch field of the HERA electron beam [HER 98b].

A hyperfine transition ($a \leftrightarrow b$) exchanges the hyperfine population of the state $|\,a\,\rangle$ with the energy E_a and the state $|\,b\,\rangle$ with the energy E_b. Its frequency ν_{ab} is defined by the energy difference:

$$\nu_{ab} = \frac{|E_a - E_b|}{h}\ . \tag{2.21}$$

The same magnetic field dependence of the energy of the hyperfine states applies then also for the frequencies of hyperfine transitions which requires a very careful tuning of the applied frequency and the magnetic field settings of a high frequency transition (HFT) to achieve optimal transition efficiency (compare figure 2.1).

The principle of a high frequency transition in a semi-classical picture is illustrated in figure 2.2. A magnetic moment $\vec{M}$ is precessing around the quantization axis of an external magnetic field B_z with its Larmor frequency (figure 2.2a). Changing the coordinate system now to a rotating system with that Larmor frequency simplifies the description of the interaction with the high

[1]HFT units are also used to determine the polarization of a gas sample in the BRP.

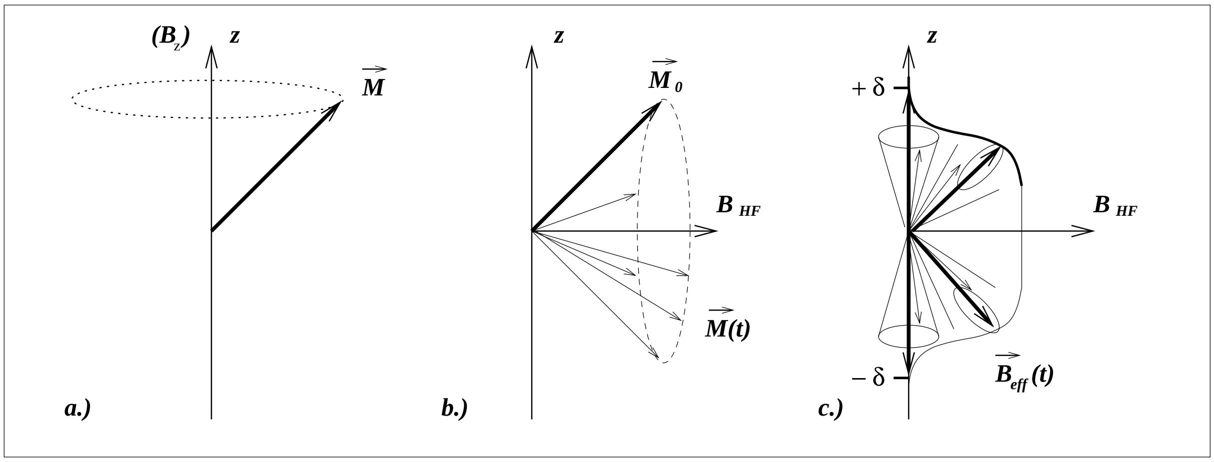

Figure 2.2: Principle of an adiabatic high frequency transition (HFT) unit: a) Precession of a magnetic moment $\vec{M}$ around a magnetic field B_z. b) Precession around the resonant high frequency field B_{HF} in a rotating system with the Larmor frequency ω_s. c) Precession in an adiabatic transition in the rotating system with a magnetic gradient field superimposed on B_z.

frequency field [Fik 71]. The magnetic moment $\vec{M}$ in this coordinate system is now precessing around the high frequency field perpendicular to the static field B_z as seen in figure 2.2b. The interaction time of the atoms with the high frequency field defines the relative position of $\vec{M}$ after the transition. As the length of the interaction area in a high frequency transition is fixed the final spin orientation depends only on the velocity of the atoms that defines the interaction time. As the velocity of beam atoms can be described by a modified Maxwell distribution the magnetic moments can never be all rotated by 180°. The overall efficiency of such a transition is theoretically limited to about 0.76 [Kus 59]. This method of *exact resonance* is mostly used if a very precise setting of the resonance frequency is needed such as in I.I. Rabi's experiments [Rab 39].

For the use of hyperfine transitions to polarize an atomic beam the highest possible transition efficiencies are wanted[2]. To reach efficiencies very close to 100 % the static magnetic field B_z might be superimposed by a gradient field along the axis of the atomic beam as first suggested by A. Abragam and J.M. Winter [Abr 58]. The effective field $\vec{B}_{eff}$, around which $\vec{M}$ describes a tight precession, is now slowly or *adiabatically* rotated along the solid curve in figure 2.2c. In this way the transition becomes mostly independent of the velocity distribution of the beam and the transition efficiency can reach values close to 100%. Practically, efficiencies of more than 98% can be reached with resonant regions of a few cm length[3] for atoms of thermal velocity.

[2] In the BRP high efficiencies are necessary to guarantee a high analyzing power

[3] The length of the resonance region depends on the strength of the gradient field and on the geometry of the coil or cavity.

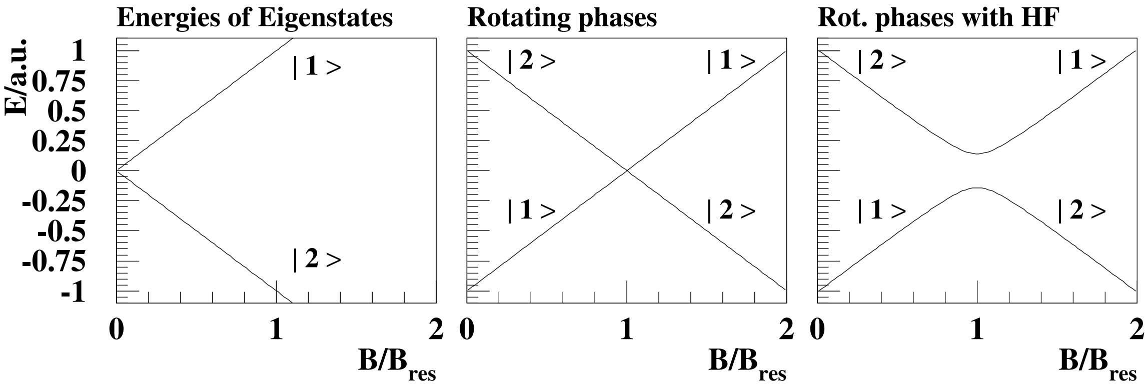

Figure 2.3: Quantum mechanical picture of an adiabatic HFT unit. **Left**: Eigenenergies of two hyperfine states in linear approximation vs. the magnetic field. B_{res} is the field value of the resonance. The horizontal axis is presenting both positions in space and time. **Center**: The high frequency terms within the Hamilton operator are equivalent to a phase rotation of both states in combination with a shift of the eigenenergies. **Right**: The strength of the high frequency field causes a separation of the eigenenergies at the cross point B_{res}.

A quantum mechanical treatment of adiabatic hyperfine transitions describing very clearly the adiabaticity can be found in [Phi 87]. Following Philpotts description, in the presence of the high frequency field the hyperfine states can be described by a mixture of the original eigenstates where these so-called adiabatic eigenstates do not overlap (compare figure 2.3), because at each cross point of the shifted energy values a transition takes place (if the amplitude of the high frequency is high enough [Bau 00]).

One can distinguish different hyperfine transitions by the change of either their total angular momentum F ($\Delta F = 0$ or $\Delta F = 1$) or the corresponding quantum number m_F ($\Delta m_F = 0$ or $\Delta m_F = 1$). High frequency transitions that change the total angular momentum F are called *strong field transitions* (SFT) for historical reasons as they have been operated first in strong static magnetic fields. They induce transitions between two different Zeeman multipletts. One or several subsequent single-photon transitions within the same Zeeman multiplett ($\Delta F = 0$) are called *medium field transitions* (MFT), whereas a multi-photon transition with $\Delta F = 0$ and $m_F \leftrightarrow -m_F$ is a *weak field transition* (WFT)[4].

The transition frequency of a SFT is typically higher than $\nu_{HFS} = E_{HFS}/h$ while for the WFT/MFT it is proportional to the field in the limiting case of $B_z \to 0$. SFTs are therefore realized by strip line resonators and WFTs/MFTs by high frequency coils. The SFTs are kept in

[4] Other authors have chosen a different notation for the transition types [Phi 87].

resonance with the help of feedback loops while the impedance matching of the coils is realized by Collins filters [Bra 95]. Since every HFT unit is tuned to a fixed frequency they have to be replaced for a change of the target gas type (hydrogen or deuterium).
If a transition induces an exchange of two hyperfine states with $\Delta m_F = 0$ the high frequency field B_{HF} is parallel to the static field B_z. In contrast to the conventions in optical spectroscopy these transitions are called σ-transitions. Respectively π-transitions are transitions with $\Delta m_F = 1$ where B_{HF} is perpendicular to B_z.
The efficiency of each single-photon transition $|\,a\,\rangle \leftrightarrow |\,b\,\rangle$ is named ε_{ab}. Hence the effect of the HFT on the hyperfine populations $\vec{N} = (N_1, N_2, \ldots)$ can be described by a matrix T^{ab}:

$$N_i^{new} = \sum_j T_{ij}^{ab} \cdot N_j^{old} \ , \tag{2.22}$$

where *new* and *old* describe the status after and before the transition. The matrix T^{ab} includes the necessary efficiencies and can - as an example for a SFT 1-4 transition of hydrogen - be written as:

$$T^{14} = \begin{pmatrix} 1-\varepsilon_{14} & 0 & 0 & \varepsilon_{14} \\ 0 & 1 & 0 & 0 \\ 0 & 0 & 1 & 0 \\ \varepsilon_{14} & 0 & 0 & 1-\varepsilon_{14} \end{pmatrix} \ . \tag{2.23}$$

In case of a multi-step transition there are T-matrices for every single step and they have to be multiplied subsequently corresponding to the order in which they take place. As an example a MFT 1-2 followed by a MFT 2-3 for hydrogen (which causes an effective cycling of the three hyperfine populations involved[5]) can be described following equation (2.22) by

$$\vec{N}^{new} = T^{23} T^{12} \vec{N}^{old} \ . \tag{2.24}$$

2.3 Spin Separation in Permanent Sextupole Magnets

W. Gerlach and O. Stern showed in [Ger 21] that a beam of silver atoms is separated into two parts by an inhomogeneous magnetic field. Such a field separates atoms with an electron spin parallel to the magnetic field from those with antiparallel electron spin because the direction of the force depends on the sign of the magnetic moment and therefore on the sign of $\langle\, m_S\,\rangle$. The field strength of a sextupole magnet as shown in figure 2.4 can be calculated by [Hae 67]

$$B(r) = B_{pt} \cdot (\frac{r}{r_{pt}})^2 \tag{2.25}$$

with the radius r, the pole tip field B_{pt} and the radius of the pole tip r_{pt}. The pole tip field

[5]In a technical context such a combination is called a MFT 1-3 because what used to be in state $|\,1\,\rangle$ before the passage will be in state $|\,3\,\rangle$ afterwards.

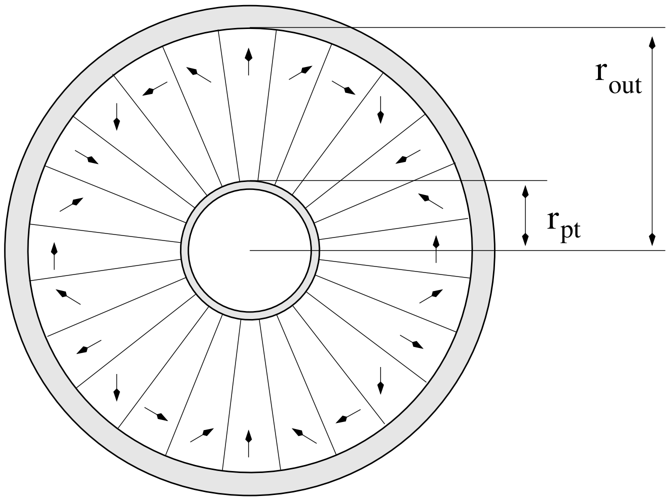

Figure 2.4: Schematic view of a sextupole magnet with 24 segments of varying magnetization directions. r_{pt} is the inner radius (at the pole tip) and r_{out} the outer radius. The magnet is encapsulated in a stainless steel can for protection purposes which is only 200 μm thick on the inside of the magnet.

value of a permanent[6] sextupole magnet is given by

$$B_{pt} = \frac{3}{2} \frac{J \cdot sin(4\pi\varepsilon/M)}{4\pi\varepsilon/M} \left(1 - \frac{r_{pt}^2}{r_{out}^2}\right) , \tag{2.26}$$

with the magnetization of the sextupole material J, the number of segments M, the outer radius of the magnet r_{out} and the so-called filling factor ε, describing the relative amount of magnetized material in the magnet ($0 < \varepsilon < 1$). The field dependance of any sextupole magnet, as given in equation 2.25, causes the axial distance of atoms with antiparallel electron spin to increase

[6]In the following context the term 'sextupole magnets' always refers to a permanent magnet.

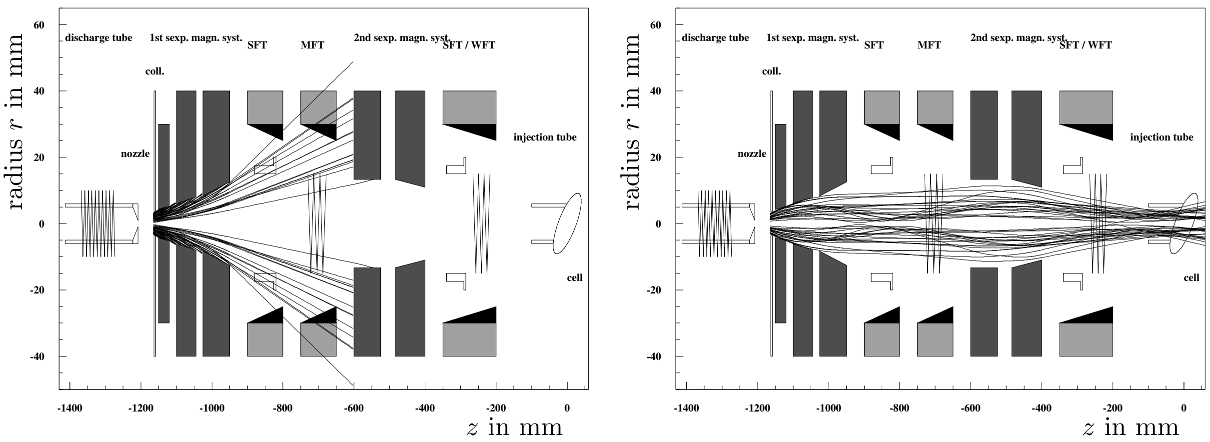

Figure 2.5: Some calculated trajectories of hydrogen/deuterium atoms through the sextupole magnet system of the HERMES ABS. The radial distance r to the beam axis vs. the negative distance z to the cell center is displayed, where the scale of r is enhanced by a factor of 10 compared to z. In the left picture one sees the deflected pure hyperfine state $|\,3\,\rangle$ in case of hydrogen ($|\,4\,\rangle$ in case of deuterium) with $m_S = -\frac{1}{2}$, whereas the right picture shows the focussed pure hyperfine state $|\,1\,\rangle$ of both target gas types with $m_S = +\frac{1}{2}$.

within the sextupole magnet - they are defocussed. These atoms are pumped away so that only atoms with parallel electron spin ($m_S = +\frac{1}{2}$) of a matching velocity are able to be transmitted through the sextupole system focussed to the beam axis. In a high holding field the atomic beam that leaves the sextupole system is nearly completely electron polarized ($P_e \approx +1$). Possible trajectories of atoms through the sextupole system at the HERMES atomic beam source have been calculated using a tracking program [Bra 95]. The results of these calculations are shown in figure 2.5 for both type of electron orientations ($m_S = \pm\frac{1}{2}$). A calculation and an optimization of the sextupole system of the Breit-Rabi polarimeter with respect to its focussing properties at the HERMES operating conditions can be found in [Bru 01].

Chapter 3

Experimental Setup of the HERMES Polarized Target

3.1 Target Chambers and Target Magnets

Until september 2000 the HERMES target was operated with a magnetic holding field of up to 350 mT longitudinally to the HERA lepton beam. The magnet used to provide such a field is a superconducting magnet cooled by gaseous helium from a dewar below the target platform. After the cold helium has circulated through the superconducting magnet it flows through the aluminum rails on which the storage cell is mounted. A schematic of the target vacuum chamber surrounded by the coils and the iron yoke of the magnet as well as a schematic of the pump system to evacuate that chamber consisting of two molecular turbo pumps with a total pumping speed of 4400 ls^{-1} is shown in figure 3.1. A thin walled exit window downstream[1] of the target chamber allows the scattered electrons or positrons and hadronic fragments to leave the target region and to be detected by the HERMES spectrometer. A fixed collimator C2 protects the storage cell from direct synchrotron light of the HERA electron/positron beam and from electrons resp. positrons hitting the cell wall. Further upstream of C2 an adjustable collimator C1 with a more narrow opening is located which is widened during positron injection into the HERA storage ring.

The superconducting magnet consists of four coils around the target chamber as indicated by the black squares in the right part of the figure. It provides the longitudinal holding field over the storage cell of up to 350 mT defining the quantization axis for the spins of the polarized atoms in the storage cell and decoupling the spins of nucleons and electrons. Since the passing HERA beam is bunched to provide high luminosity for the collider experiments H1 and ZEUS it may induce resonant nuclear depolarization of the target gas. These resonances can be avoided

[1] Up- and downstream are used with respect to the HERA lepton beam direction.

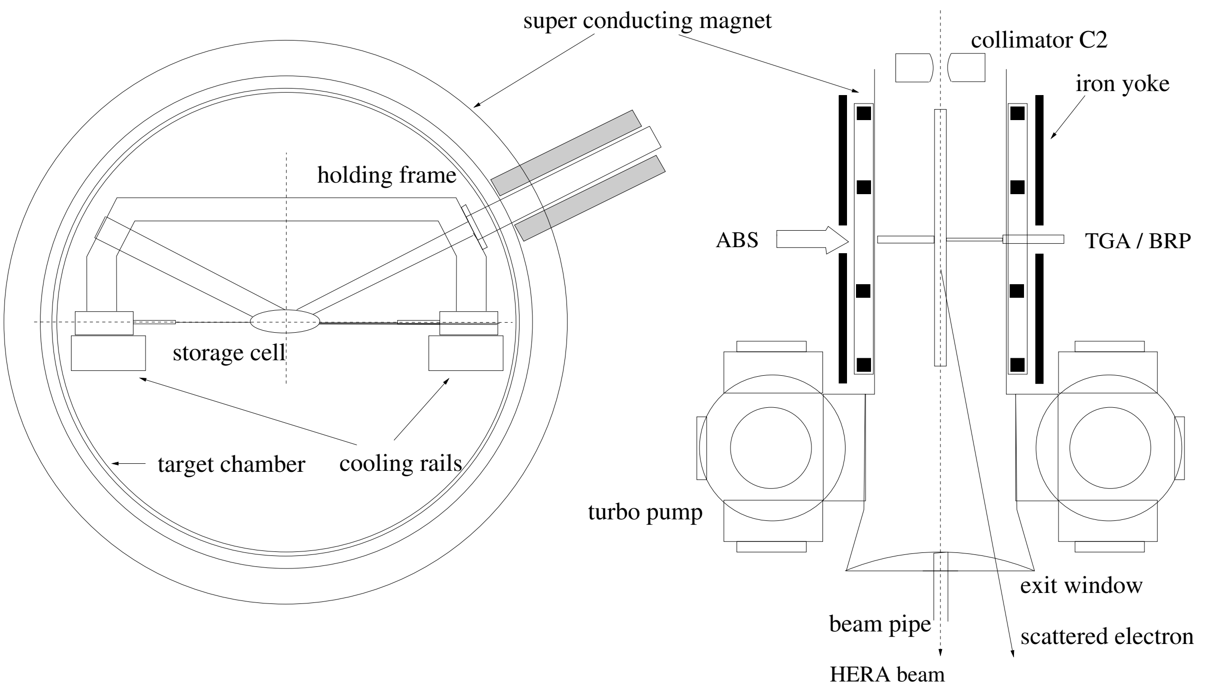

Figure 3.1: Schematic view of the target section with the target chamber incl. storage cell viewed upstream (left picture) and the top view of the target chamber (right picture) showing also the pump system and the exit window.

by a proper setting of the holding field as long as its homogeneity is sufficient [Kol 98]. In case of hydrogen as target gas the necessary maximum fluctuation of the magnetic field along the storage cell is 1.5%, i.e. 5 mT at a field value of 335 mT. For the running period with deuterium gas this issue was found to be less critical [Bau 00].

After the end of the running period with a longitudinal magnetic holding field and a deuterium gas target in September 2000, the HERMES target was modified for the measurements with a hydrogen gas target in a transversally orientated magnetic holding field. Thus a new target magnet had to be built and as the magnitude of the transversal magnetic field is limited by the amount of synchrotron radiation[2] produced by the deflection of the beam by the target magnet, it was decided to build this transverse magnet using conventional materials instead of the superconducting coils in the longitudinal magnet. One advantage of conventional magnets is that they don't have to be cooled using cold gaseous helium.

Additionally the use of a transverse magnet requires a more careful field setting to avoid bunch field induced resonant depolarization by the HERA beam. The orientation of the bunch field induced magnetic field and the target field transversal to the HERA beam direction allows both

[2]This synchrotron radiation causes a signal background in the HERMES detectors and thus the opening angle of the radiation fan has to be kept within certain limits.

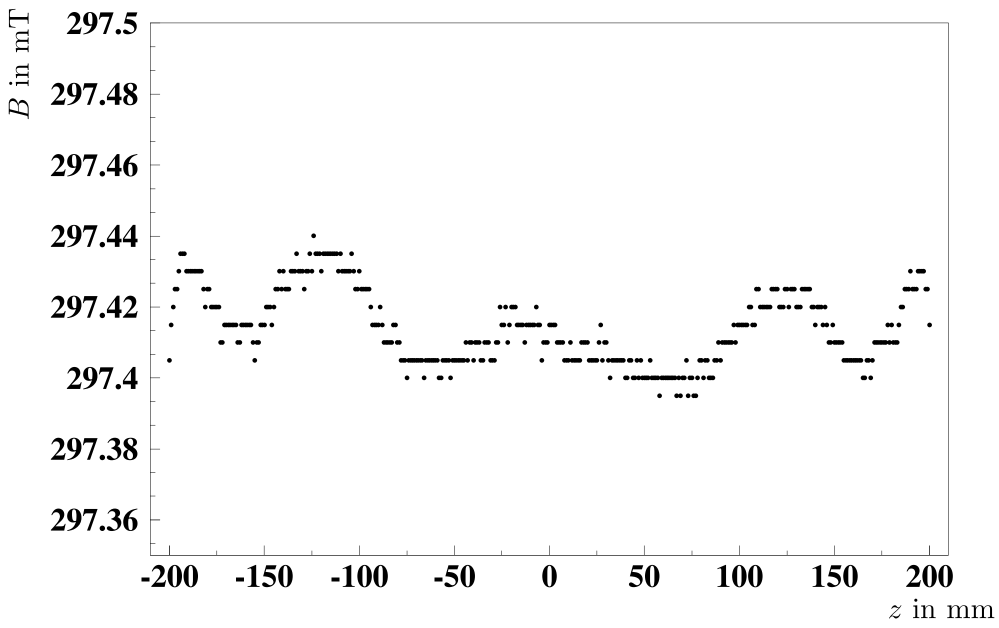

Figure 3.2: Measured magnetic field of the transverse target magnet as function of the position z in mm along the HERA beam axis where the center of the storage cell with the connected injection and sample tube is at $z = 0$. Each dot represents one measurement. The required homogeneity to avoid bunch field induced resonant depolarization by the HERA beam is a maximum fluctuation of $\Delta B \leq 0.15$ mT, which is reached in case of the HERMES target magnet with a fluctuation of less than 0.05 mT along z.

σ- and π-transitions because these fields have both perpendicular and parallel components. Hence the spacing between the beam induced resonances is narrower than in the longitudinal case, where only perpendicular components allowing π-transitions exist. Therefore a higher homogeneity of the transverse target magnet of $\Delta B \leq 0.15$ mT at a field value of 297 mT is required. This homogeneity was achieved after an additional shimming of the pole tips of the transverse magnet with 1 mm thin plates made of *Vacoflux 50* [3]. The magnetic field map along the HERA beam (represented by the coordinate z) is shown in figure 3.2 giving a homogeneity of $\Delta B \leq 0.05$ mT which is two orders of magnitude better than for the longitudinal magnet.

3.2 Storage Cell

The HERMES target storage cell [Stw 95] is made of two 75 μm thin pure aluminum sheets which are tightly spot-welded to prevent atoms from entering the gap between them. It is 400 mm long and has an elliptical shape of 21×8.9 mm^2 cross section. All aluminum parts of the cell

[3] Vacoflux is a registered trademark of Vacuumschmelze GmbH, Hanau, Germany.

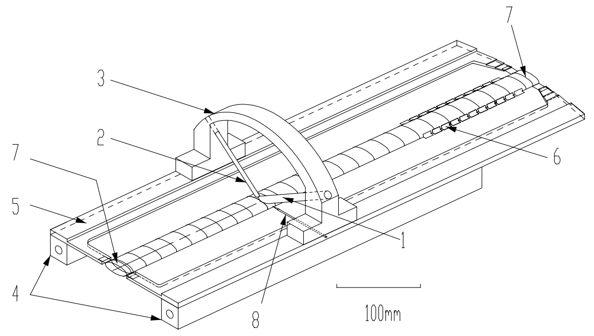

Figure 3.3: The HERMES storage cell with the HERA beam passing from left to right: 1) Injection tube; 2) Sample tube (Extension tube not shown); 3) Tube support arch; 4) Cryogenic colling and support rails; 5) Support plates; 6) Cell extension with pumping apertures; 7) Cell end support collar; 8) Unpolarized gas feed capillary.

are coated with Drifilm [Wit 56, Cam 87, Tho 87, Stn 95, Bra 95, Fed 97] to minimize depolarization and recombination caused by wall collisions [Swe 88, Cam 87, Lev 88]. A potentially better coating material would be Teflon but it may not be used within the HERA environment because it is less radiation hard. Physically the cell is 147 mm longer in the downstream direction as shown in figure 3.3 to ensure that all scattered particles inside the spectrometer detector acceptance pass through the same thickness of material.

Three different sizes of cells have been used so far. The mentioned size of 21×8.9 mm^2 is the actual size since December 1999 and is called the medium-sized cell. The 'large' one which was used until December 1999 had a cross section of 29×9.8 mm^2 and a 'small' one (19×8.0 mm^2) was tested in January 1999 and found to be too small in cross section.

Wake field suppressors made of 100 μm thick titanium have been designed to guide the electromagnetic high frequency field of the bunched HERA beam[4] and form an electrical connection between the storage cell and the HERA beam pipe.

The storage cell is mounted on cooling rails which are temperature regulated by gaseous helium after having cooled the superconducting magnet. The optimal operating temperature for hydrogen was found to be about 100 K where recombination and depolarization effects are low. Additionally the lower conductance at this temperature leads to a higher target thickness by a factor of $\sqrt{3}$ compared to room temperature. For deuterium the target temperature could still be decreased to about 65 K which increased the target thickness by about 23 percent compared to 100 K.

The temperature of the cooling rails is monitored at three different positions by platinum resistors. Since 1999 an additional thermocouple wire is attached to the aluminum foil close to the cell ellipse to monitor the cell temperature directly during the injection of the HERA beam. The cooling rails of the storage cell are connected to the target chamber flange on the upstream

[4]If not mentioned otherwise HERA beam refers to the electron/positron beam of the HERA storage ring as the proton ring is not used by the HERMES experiment.

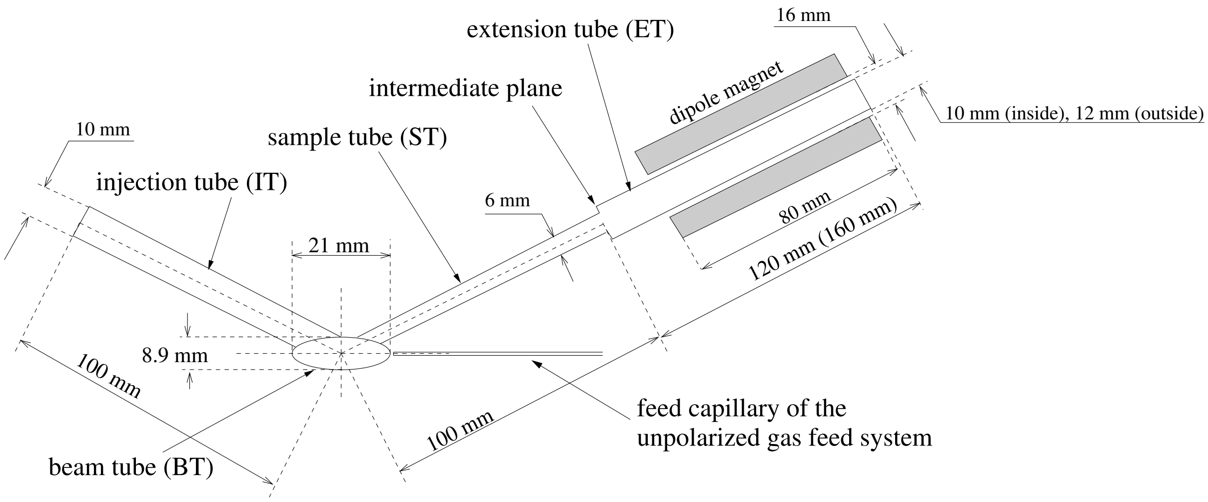

Figure 3.4: Onscale schematic of the medium size storage cell showing the dimensions of the elliptical cross section and the side tubes. Until 1999 cells with a smaller sample tube of 5 mm diameter have been used. The size of the sample tube has been increased to sample more particles which results in a better statistical precision of the measured quantities by the target gas analyzer and the Breit-Rabi polarimeter. For the setup with the transversal magnet the extension tube had to be prolonged to 160 mm length as the whole setup of analyzers had to be moved back by 40 mm.

end. Due to the thermal contraction of the cell when being cooled, the position of the cell center changes relative to the atomic beam source and the Breit-Rabi polarimeter. From room temperature down to 100 K the cell center moves by 0.9 mm. The alignment of atomic beam source and Breit-Rabi polarimeter relative to the cell center includes an offset to compensate for the effect at the target working point.

Figure 3.4 shows the storage cell view from the HERMES spectrometer position, i.e. upstream. Two side tubes are connected to the beam tube, one to inject the polarized atoms through the injection tube and another one to sample the target gas and analyze it in the target gas analyzer and the Breit-Rabi polarimeter. The sample tube is tilted in respect to the axis of the injection tube to ensure that the sampled atoms have thermalized with the storage cell wall. The dipole magnet around the extension tube mounted outside the target chamber extends the magnetic holding field of the superconducting magnet to prevent depolarization inside the extension tube. Below the sample tube the small feed capillary of the unpolarized gas feed system is connected to the cell center.

3.3 Unpolarized Gas Feed System (UGFS)

The unpolarized gas feed system (UGFS) is required for the unpolarized physics program of the HERMES experiment and can be used to inject gas into the storage cell or the target chamber directly. The density of the unpolarized gas in both storage cell and target chamber can be controlled by the gas flow rate of UGFS, which is adjusted by either a flow regulator in case of a high required density of the unpolarized gas and thus high fluxes or a system of two valves, one regulation valve and one dosing valve.

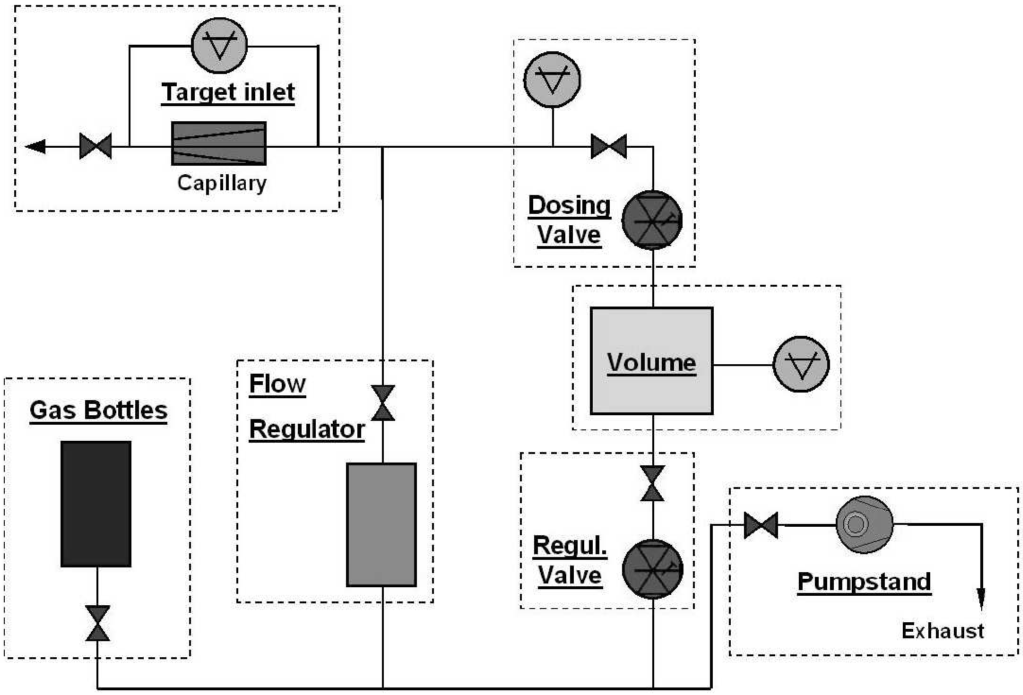

Figure 3.5: Schematic view of the unpolarized gas feed system. Unpolarized molecules of different gas types may be injected into the storage cell or into the target chamber directly via a capillary of 0.5 mm diameter and either 10 mm or 60 mm length. The flow into the target cell can be controlled by either a flow regulator (for high fluxes) or a system of regulation and dosing valve (for low fluxes).

3.4 Atomic Beam Source (ABS)

The atomic beam source [Sto 94, Kor 90, Nas 02] consists of a dissociator, a skimmer and a collimator for beam formation, a sextupole magnet system consisting of five magnets to focus atoms

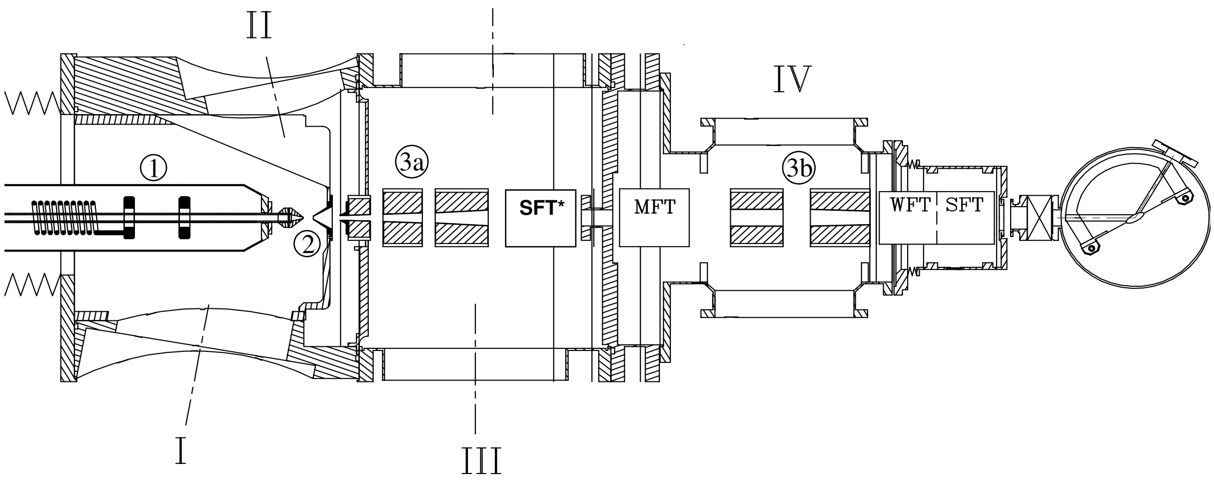

Figure 3.6: Schematic of the ABS setup. Hydrogen or deuterium molecules are dissociated in the discharge tube of the dissociator ①. Adiabatic gas expansion after the nozzle creates a peaked atomic beam. Skimmer ② and collimator are limiting its spread to the acceptance of the entrance of the sextupole magnet system ③. Several high frequency transitions can be used to manipulate the hyperfine population of the atomic beam. The roman numbers denote the four stages of the differential pumping system.

with $m_s = +\frac{1}{2}$ into the storage cell by means of Stern-Gerlach spin separation and adiabatic high frequency transitions to manipulate the hyperfine population of the atomic beam. With the setup used within the HERMES experiment, injected fluxes (i.e. the number of injected atoms per second) of $\Phi^{\mathrm{ABS}} \simeq 6.6 \cdot 10^{16}$ s^{-1} in case of hydrogen and $\Phi^{\mathrm{ABS}} \simeq 4.5 \cdot 10^{16}$ s^{-1} in case of deuterium[5] have been observed. These values have been calculated from the density-dependent spin exchange relaxation in [Bau 00] and agree with previous compression tube measurements [Stw 97]. The injected nuclear polarization P_z^{inj} was stably above 0.97 for hydrogen and above 0.91 for deuterium. A schematic picture of the setup of the atomic beam source can be seen in figure 3.6.

Pure molecular hydrogen/deuterium gas provided by a hydrogen generator[6] enters the dissociator from the left. The molecules are dissociated by a radio frequency discharge with a frequency of 13.56 MHz in a pyrex tube of the dissociator with a degree of dissociation of up to 80% at a throughput of about 1 $\frac{\mathrm{mbar \cdot l}}{\mathrm{s}}$ and radio frequency powers of about 300 W [Nas 02]. To maximize the stability and the degree of dissociation an amount of oxygen between 0.1 and 0.3

[5]The injected fluxes are given for the case of disabled high frequency transitions, i.e. injecting two hyperfine states in case of hydrogen and three states in case of deuterium

[6]The generator has been installed in September 2000. Gas bottles have been used before.

volume percent is added to the molecular gas. The water produced by the discharge covers the glass tube where together with hydrogen atoms OH^- radicals are produced which additionally dissociate hydrogen molecules [Wis 64, Kor 90].

A high degree of dissociation at higher throughputs can be achieved using a recently developed mircowave dissociator based on a modified waveguide surfatron field applicator [Koc 99, Nas 02]. The microwave dissociator operates at a frequency of 2.45 GHz. With typical throughputs between 1 and 2 $\frac{\mathrm{mbar \cdot l}}{\mathrm{s}}$ and microwave powers of about 600 W a degree of dissociation higher than 80% is achieved.

The atomic gas flows through a conical nozzle with an opening diameter of 2 mm which is cooled to about 100 K. The water produced by the discharge then freezes on the nozzle surface and reduces recombination processes. When the ice layer gets too thick it has to be removed[7] as it reduces the conductance and the pressure in the discharge tube increases causing more volume recombination and thus reducing the degree of dissociation.

After passing the cold nozzle the gas expands into the vacuum of the dissociator chamber. The divergence of the atomic beam is controlled by a skimmer and collimator system to match the aperture of the sextupole magnet system. A powerful differential pumping system with a total nominal pumping speed of more than 15000 ls^{-1} ensures a low attenuation of the beam caused by residual gas. A roots blower forepump with a nominal pumping speed of 1000 ls^{-1} is used to provide low fore-vacuum pressure of the turbopumps on the first three of a total of four vacuum chambers (dissociator -, skimmer - plus first and second sextupole chamber) so that the turbopumps do not run into their compression limit even with high dissociator throughputs of up to 5 $\frac{\mathrm{mbar \cdot l}}{\mathrm{s}}$.

With the microwave dissociator a high degree of dissociation was observed of up to 4 $\frac{\mathrm{mbar \cdot l}}{\mathrm{s}}$. These throughputs contain future development potential as they could lead to a higher atomic beam intensity provided by the atomic beam source. For this purpose the sextupole magnet system needs to be redesigned to match the correspondingly higher velocities of the atoms. This redesign however requires a very precise understanding of the beam formation and attenuation by residual gas included into a simulation program able to calculate the trajectories of the atoms based on realistic starting conditions after the collimator [Nas 02, Loz 93].

The magnet system of the HERMES atomic beam source consists of a total of five segmented permanent sextupole magnets with high pole tip fields of about 1.45 T. According to Stern-Gerlach spin separation each magnet focuses atoms with $m_s = +\frac{1}{2}$ to the entrance to the injection tube into the storage cell and defocuses atoms with $m_s = -\frac{1}{2}$ as explained in more detail in

[7] The removal of the ice layer by warming up the nozzle and pumping away the water is called nozzle regeneration.

chapter 2.3. These magnets consist of 24 segments of *Vacodym*[8]. To protect the magnets from being chemically destroyed by atomic hydrogen they are protected by a stainless steel cylinder [Sch 91].

Together with high frequency transition units between the sextupole magnets and after the last magnet almost any hyperfine population can be injected into the cell. Between the sextupoles a strong field transition (SFT) and a medium field transition (MFT)[9] can be used simultaneously whereas the weak field transition (WFT) and the SFT after the sextupole magnets can only be used separately because they share the coils for the static and gradient magnetic field. A detailed description of the principle of high frequency transition units can be found in chapter 2.2.

Both SFT units in the atomic beam source produce a high frequency field that has no perpendicular component relative to the static field. Thus they can only be operated to induce σ-transitions (SFT 2$\leftrightarrow$4 for hydrogen or SFT 2$\leftrightarrow$6 and 3$\leftrightarrow$5 for deuterium).

As two subsystems of sextupole magnets are used the transmission probabilities of atoms in the hyperfine state $|\,a\,\rangle$ through the whole sextupole system is described by a matrix σ_{ab}, if an atom enters the first subsystem in state $|\,a\,\rangle$ and the second part in state $|\,b\,\rangle$. With the description of the effect of an adiabatic hyperfine transition by a matrix T^{ab} in equation (2.22) one can combine all transitions between the sextupole magnets to an effective transition matrix B^{ab} by multiplying the corresponding T-matrices. The same can be done for all transitions in the appendix of the atomic beam source (i.e. after the second sextupole subsystem) resulting in a matrix A^{ab}.

Using this nomenclature, the number of atoms injected into the storage cell in a certain hyperfine state $|\,a\,\rangle$ per unit time, the beam intensity I_a, can be described by[10]

$$I_a = \sum_j A^{aj} \sum_i \sigma_{ij} B^{ij} \ , \tag{3.1}$$

which simplifies significantly with a decreasing amount of hyperfine transitions. If for example no transitions are used to inject a positively electron polarized atomic beam into the storage cell, the beam intensity is given by

$$I_a = \sigma_{aa} \ . \tag{3.2}$$

[8] Vacodym is a registered trademark of Vacuumschmelze GmbH, Hanau, Germany.

[9] Any transition with a high frequency coil (WFT or MFT) can in principle be used for both purposes so that a MFT unit can be retuned and operated as a WFT unit and vice versa.

[10] Before the atomic beam reaches the first sextupole magnet all hyperfine states have equal population.

For the injection of P_z^+ in case of deuterium (using the SFT 3↔5 between the sextupoles and the SFT 2↔6 in the appendix) the transmission through the atomic beam source can be described in the following way:

$$\begin{pmatrix} 1 \\ 1 \\ 1 \\ 1 \\ 1 \\ 1 \end{pmatrix} \overset{\text{sixpole}}{\Longrightarrow} \begin{pmatrix} \sigma_1 \\ \sigma_2 \\ \sigma_3 \\ \sigma_4 \\ \sigma_5 \\ \sigma_6 \end{pmatrix} \overset{\text{SFT 3-5}}{\Longrightarrow} \begin{pmatrix} \sigma_1 \\ \sigma_2 \\ \sigma_3(1-\varepsilon_{35})+\sigma_5\varepsilon_{35} \\ \sigma_4 \\ \sigma_5(1-\varepsilon_{35})+\sigma_3\varepsilon_{35} \\ \sigma_6 \end{pmatrix}$$
$$\overset{\text{sixpole}}{\Longrightarrow} \begin{pmatrix} \sigma_{11} \\ \sigma_{22} \\ \sigma_{33}(1-\varepsilon_{35})+\sigma_{53}\varepsilon_{35} \\ \sigma_{44} \\ \sigma_{55}(1-\varepsilon_{35})+\sigma_{35}\varepsilon_{35} \\ \sigma_{66} \end{pmatrix} \overset{\text{SFT 2-6}}{\Longrightarrow} \begin{pmatrix} \sigma_{11} \\ \sigma_{22}(1-\varepsilon_{26})+\sigma_{66}\varepsilon_{26} \\ \sigma_{33}(1-\varepsilon_{35})+\sigma_{53}\varepsilon_{35} \\ \sigma_{44} \\ \sigma_{55}(1-\varepsilon_{35})+\sigma_{35}\varepsilon_{35} \\ \sigma_{66}(1-\varepsilon_{26})+\sigma_{22}\varepsilon_{26} \end{pmatrix} . \tag{3.3}$$

The result on the right side of equation (3.3) is similar to the one which can be derived using equation (3.1). In the ideal case of full transition efficiencies and optimal sextupole transmissions only states $|\,1\,\rangle$ and $|\,6\,\rangle$ should remain in the atomic beam. A summary of the default injection modes for hydrogen and deuterium can be seen in table 3.1 and 3.2 respectively.

To derive the transmission probability matrix both for hydrogen and deuterium gas one can use a computer simulation calculating the trajectories of atoms through the magnetic field of the sextupole system as seen in figure 2.5 and then compare the normalized hyperfine populations before the first magnet and entering the injection tube to the storage cell. Braun and Baum-

Hydrogen		high frequency transitions	
Pol.	Inj. States	appendix	between sextupoles
P_e	$\|1\rangle$,$\|2\rangle$	off	off
P_z^+	$\|1\rangle$,$\|4\rangle$	SFT 2-4	off
P_z^-	$\|2\rangle$,$\|3\rangle$	WFT 1-3	off
P_e^+, P_z^+	$\|1\rangle$	off	SFT 2-4 / MFT 2-3
P_e^+, P_z^-	$\|2\rangle$	off	WFT 1-3 / MFT 1-3
P_e^-, P_z^-	$\|3\rangle$	WFT 1-3	SFT 2-4 / MFT 2-3
P_e^-, P_z^+	$\|4\rangle$	SFT 2-4	WFT 1-3 / MFT 1-3
P_{no}	empty	off	SFT 2-4, WFT 1-3

Table 3.1: Injection modes of the atomic beam source for hydrogen running. The last mode of empty hyperfine population with running atomic beam source is used to determine the amount of molecules injected into the storage cell by the ABS. The single states have been used for Bhabha measurements [Wei 98].

Deuterium		high frequency transitions	
Pol.	Inj. States	appendix	between sextupoles
P_e	$\|1\rangle$,$\|2\rangle$,$\|3\rangle$	off	off
P_z^+	$\|1\rangle$,$\|6\rangle$	SFT 2-6	SFT 3-5
P_z^-	$\|3\rangle$,$\|4\rangle$	WFT 1-4/2-3	SFT 3-5
P_{zz}^+	$\|3\rangle$,$\|6\rangle$	SFT 2-6	MFT 1-4
P_{zz}^-	$\|2\rangle$,$\|5\rangle$	SFT 3-5	MFT 1-4
P_e^+, P_z^+	$\|1\rangle$	off	MFT 3-4, SFT 2-6
P_e^+, P_{zz}^-	$\|2\rangle$	off	WFT 1-4/2-3, SFT 2-6
P_e^+, P_z^-	$\|3\rangle$	off	WFT 1-4/2-3, SFT 3-5
P_e^-, P_z^-	$\|4\rangle$	WFT 1-4/2-3	MFT 3-4, SFT 2-6
P_e^-, P_{zz}^-	$\|5\rangle$	SFT 3-5	WFT 1-4/2-3, SFT 3-5
P_e^-, P_z^+	$\|6\rangle$	SFT 2-6	WFT 1-4/2-3, SFT 2-6

Table 3.2: Injection modes of the atomic beam source for deuterium running. More injection modes are possible but were not used by default. The single states have been used for the BRP calibration (see chapter 3.6.1).

garten gave estimates for the transmission probablities with parametrized starting conditions[11] of the atoms from the collimator plane in the atomic beam source [Bra 95, Bau 00] because the precise circumstances of the beam formation at the nozzle have been basically unknown. Later, Nass computed realistic starting conditions using a Monte-Carlo simulation by Bird [Bir 94] for the HERMES atomic beam source [Nas 02]. No trajectory calculations with these starting conditions have been carried out yet.

3.5 Target Gas Analyzer (TGA)

The target gas analyzer [Bau 96] is located between the target chamber and the Breit-Rabi polarimeter with whom it shares the vacuum system (see figure A.1). Details about the vacuum system are described in appendix A. The purpose of the target gas analyzer is to measure the atomic and the molecular contents of the gas sample to derive the amount of nucleons in atoms relative to the total amount of nucleons as seen by the HERA positron/electron beam.

The setup shown in figure 3.7 consists of two baffles, a chopper and a 90° off-axis quadrupole mass spectrometer (QMS) with a cross beam ionizer. A channel electron multiplier (CEM) is used for the detection of the ionized atoms and molecules. The system of baffles ensures that atoms entering the ionizer volume of the quadrupole mass spectrometer can not hit the inner ionizer walls and recombine there causing a virtual molecular beam signal. For this purpose one baffle is mounted at a short distance to the extension tube and the other baffle directly in front of the cross beam ionizer. The axis of the cross beam ionizer is tilted by 7° with respect

[11] A so-called molecularity parameter μ with $0 \leq \mu \leq 1$ has been used to describe the laminarity of the formed atomic beam which had to maximal ($\mu = 1$) to agree with the measurements.

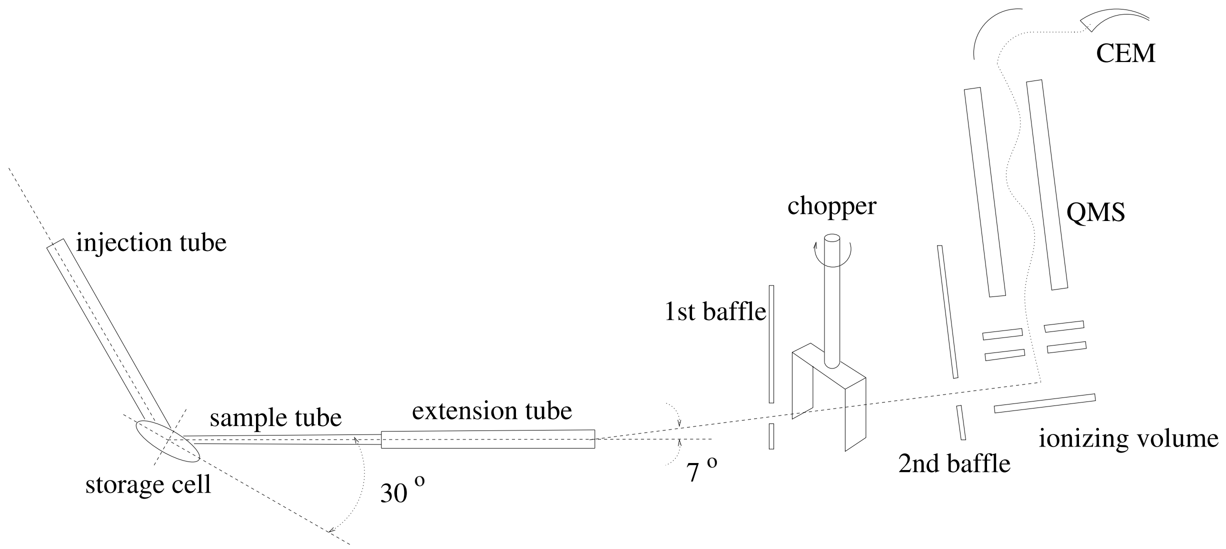

Figure 3.7: Schematic of the target gas analyzer. The beam leaving the extension tube is chopped and filtered in a quadrupole mass spectrometer (QMS) before being detected by a channel electron multiplier (CEM). The first baffle rejects any gas flow from sources other than the sample beam while the second baffle collimates the beam so that no atom from the beam may recombine on the wall of the ionizing volume.

to the beam axis of the sample and extension tube not to block the beam into the Breit-Rabi polarimeter. Particles entering the ionizing volume are ionized by 70 eV electrons emitted from a filament with the ionization cross section $\sigma_{\mathrm{mass}}^{\mathrm{ion}}$ [12] and extracted. After being mass filtered by the quadrupole rods of the QMS the remaining ions are detected by a channel electron multiplier[13] with a certain detection probability of $\varepsilon_{\mathrm{mass}}$ and converted into an electronically measureable pulse and counted by a multichannel time resolving counter on a digital signal processor (DSP) board. The detection probability $\varepsilon_{\mathrm{mass}}$ depends also on the mass of the detected particle and includes the transmission probability of the ions through the QMS.
A trigger signal from the chopper electronics is used to synchronize the chopper status and the correlated counting rate. The chopper rotating at 5.5 Hz is required in order to distinguish particles from the sample beam and those from residual gas. The beam rates are calculated by the difference of the counts per time in the periods with open and closed[14] chopper. Analyzing the time spectrum as seen in figure 3.8 gives an estimation of the statistical error of the beam intensity measurement. Frequency drifts of the chopper motor are compensated by an adjust-

[12]The ionization cross section varies for different masses of the particles and has been measured by [Rap 65, Sha 87].
[13]The CEM is installed at 90° with respect to the quadrupole rods of the QMS in order to reject neutral particles.
[14]Open and closed refers to the blocking of the sample beam before entering the ionizer volume.

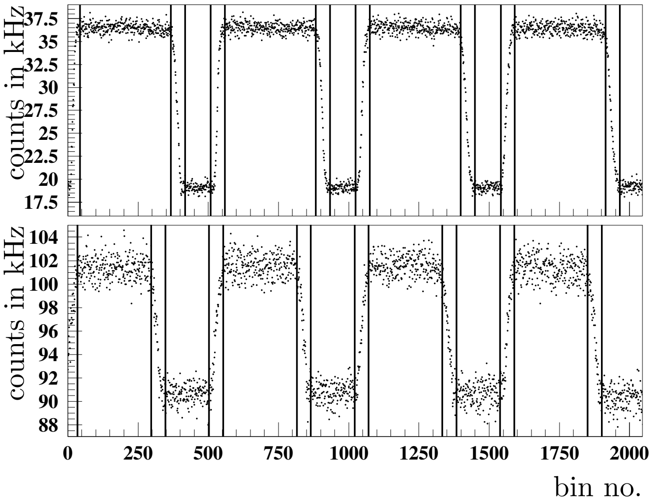

Figure 3.8: Time spectrum of atomic countrates of both detectors (upper figure: BRP, lower figure: TGA). The vertical lines indicate the bin numbers corresponding to the limits between the chopper positions open, undefined and closed. To calculate the signal from the sample beam the count rates with chopper closed (chamber background) are subtracted from the count rates with chopper open (beam plus background).

ment of the bin length by the DSP software so that two chopper turns fit exactly the 2048 bins of the time resolving counter. The typical bin length is about 175 μs at a chopper frequency of 5.5 Hz. Details about the control system of the HERMES target hardware can be found in appendix C.

The measured atomic (molecular) beam rates S_a (S_m) of the TGA are proportional to the corresponding particle flux Φ_a (Φ_m)[15] into the TGA times the ionization cross section σ_a^{ion} (σ_m^{ion}) and the detection probability ε_a (ε_m). The probability for ionization is proportional to the time that the particles need to pass the ionizing volume. Hence the signal is additionally proportional to the mean inverse velocity of the particles $\left\langle \frac{1}{v_a} \right\rangle$ $\left(\left\langle \frac{1}{v_m} \right\rangle\right)$ because thermalized particles travel with a mass dependent velocity.

Additionally the magnetic fringe fields of the target and the spectrometer magnet influence the trajectories of the ions inside the cross beam ionizer and the mass spectrometer. Thus the magnetic field values are kept constant during all measurements. Taking all the mentioned parameters into account one finds

$$S_{a,m} \propto f(B, I_{\text{emis}}) \cdot \sigma_{a,m}^{\text{ion}} \cdot \varepsilon_{a,m} \cdot \left\langle \frac{1}{v_{a,m}} \right\rangle \cdot \Phi_{a,m} \ . \tag{3.4}$$

The dependence on the emission current I_{emis} of the electron gun of the cross beam ionizer has been measured and is shown in figure 3.9 leaving all other parameters of equation (3.4) unchanged. The dependence on I_{emis} is not necessarily linear as space charge effects in the electron gun can lead to a change in the trajectories of the ionizing electrons and thus to a change of the ionizing efficiency. The total flux of nucleons into the TGA $\tilde{\Phi}^{\text{TGA}}$, normalized to the number of nucleons per atom, is given by the sum of atomic flux and twice the molecular

[15]It should be noted that a particle flux Φ_m refers to the number of molecules per second, where ϕ_m refers to the number of atoms, that are bond in molecules, per second.

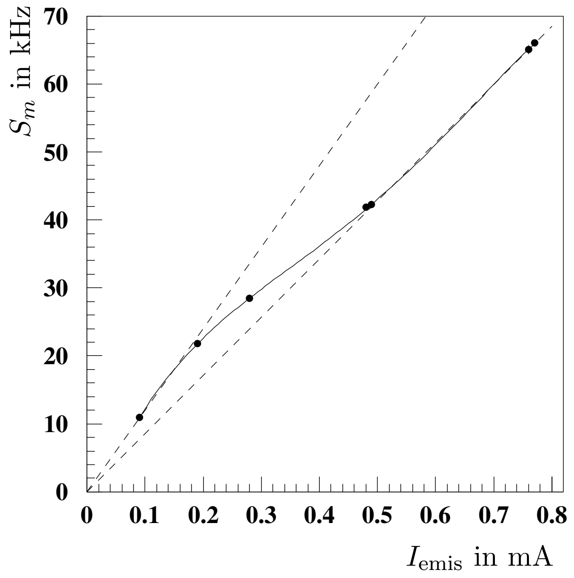

Figure 3.9: Beam signal of the TGA as function of the emission current I_{emis}. The line connecting the measurement points is a fit with a 4th degree polynomial. Two dashed lines are indicating two different regions of proportionality. All other parameters of equation (3.4) have been constant during the measurement which was performed using a constant gas flow from the unpolarized gas feed system into the storage cell and measuring the beam signal for molecules $_m$.

flux. This total flux into the TGA is proportional to the injected atomic flux of the atomic beam source:

$$\tilde{\Phi}^{\text{TGA}} = \Phi_a + 2\Phi_m \propto \Phi^{\text{ABS}} \ . \tag{3.5}$$

With the temperature T of the storage cell and thus of the thermalized particle and the mass $M_{a,m}$ of that particle

$$\left\langle \frac{1}{v_m} \right\rangle = \left\langle \sqrt{\frac{M_m}{T}} \right\rangle = \left\langle \sqrt{\frac{2 \cdot M_a}{T}} \right\rangle = \sqrt{2} \left\langle \frac{1}{v_a} \right\rangle \tag{3.6}$$

is fulfilled due to the double mass of a molecule compared to an atom. Using equations (3.4), (3.5) and (3.6) the partial beam rates $S_{a,m}$ can be interpreted in a similar way as parts of the total rate $S_{\text{tot}} \propto \tilde{\Phi}^{\text{TGA}}$

$$S_{\text{tot}} = S_a + \sqrt{2} \cdot \kappa \cdot S_m \ , \tag{3.7}$$

where κ is the calibration constant of the target gas analyzer giving the relative sensitivity of the TGA for atomic and molecular beam:

$$\kappa = \frac{\sigma_a^{\text{ion}} \cdot \varepsilon_a}{\sigma_m^{\text{ion}} \cdot \varepsilon_m} \ . \tag{3.8}$$

The velocity of a particle depends on the temperature of the surface it thermalized with. Hence the flowrate into the TGA depends also on the temperature of the extension tube because those particles entering the TGA have thermalized with the extension tube wall[16]. This differs from the situation in the Breit-Rabi polarimeter because the TGA acceptance is tilted by 7° with respect to the extension tube axis and thus only detects particles that had at least their last

[16]Measurements showed that the extension tube has typically a higher temperature than the rest of the cell as it is only connected by a thread to the storage cell frame.

wall collision in the extension tube. Simulations of the molecular flow showed, that any particle experiences an average of about 112 collisions [Hen 98, Bau 00] on the extension tube wall before they are detected by the TGA.

Normalized flowrates $\phi_{a,m}$ can be defined making them comparable and independent of temperature and emission current using an empirical temperature dependence $g(T)$ [Bau 00, Kol 98] and the measured function $f(B, I_{\text{emis}})$ from figure 3.9:

$$\phi_a = \frac{S_a}{g(T) \cdot f(B, I_{\text{emis}})} \tag{3.9}$$

$$\phi_m = \frac{\sqrt{2} \cdot \kappa \cdot S_m}{g(T) \cdot f(B, I_{\text{emis}})} \tag{3.10}$$

The fraction of nucleons in atoms relative to all nucleons of the particles entering the target gas analyzer can then be defined similar to equation (1.5) by

$$\alpha^{\text{TGA}} = \frac{\phi_a}{\phi_a + \phi_m} = \frac{S_a}{S_a + \sqrt{2} \cdot \kappa \cdot S_m} \ . \tag{3.11}$$

3.5.1 Calibration of the TGA

The purpose of the target gas analyzer is to measure the atomic fraction α^{TGA} as given by equation (3.11). Besides the measured partial beam rates $S_{a,m}$ this equation contains the unknown relative sensitivity κ which is determined by a calibration of the TGA. This calibration can be done making use of the stability of the intensity of the atomic beam source Φ^{ABS} in equation (3.5) during normal operation. The detected total rate S_{tot} is then also constant and rewriting equation (3.7) leads to

$$S_a + \sqrt{2} \cdot \kappa \cdot S_m = \text{constant} \tag{3.12}$$

or

$$\phi_a + \phi_m = \phi_{\text{tot}} = \text{constant} \tag{3.13}$$

if one uses the normalized flowrates from equations (3.9) and (3.10). κ can now be determined by a linear fit of ϕ_m versus ϕ_a as

$$\frac{\partial \phi_m}{\partial \phi_a} = -1 \ , \tag{3.14}$$

and thus using equations (3.9) and (3.10)

$$\frac{\partial \left(\frac{S_m}{g(T) \cdot f(B, I_{\text{emis}})} \right)}{\partial \left(\frac{S_a}{g(T) \cdot f(B, I_{\text{emis}})} \right)} = -\frac{1}{\sqrt{2} \cdot \kappa} \ . \tag{3.15}$$

To obtain a low systematical uncertainty of the derived κ-value it is necessary to vary the atomic fraction α^{TGA} over a preferably large range. Displaying the corrected partial molecular beam rates versus the corrected partial atomic beam rates for the varying α^{TGA} and making a linear

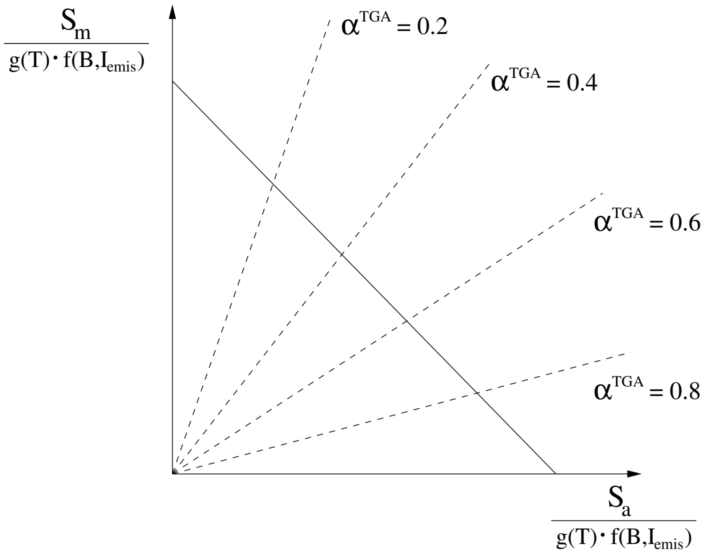

Figure 3.10: The corrected partial molecular beam rate as a function of the corrected partial atomic beam rate of the TGA at a constant intensity of the atomic beam source Φ^{ABS}. The slope of the solid line equals the right side of equation (3.15). The dashed lines correspond to constant α^{TGA} at different Φ^{ABS}.

fit to these data points results in a straight line with a slope of $-\frac{1}{\sqrt{2}\cdot\kappa}$ as shown in figure 3.10. As recombination is a temperature dependent process (compare chapter 4.1) the α^{TGA}-value varies with the temperature of the storage cell. Thus performing a so-called temperature scan is one possibility to calibrate the TGA but requires the knowledge of the temperature correction function $g(T)$.

An additional but unintended way to calibrate the TGA is to employ the strong variation of α^{TGA} at T_{cell} = const after an accidental beam loss of the HERA electron/positron beam near the HERMES target region[17]. This beam loss calibration does not require any knowledge about the temperature correction function $g(T)$.

Method 1: Temperature Scans

To vary the temperature of the storage cell the helium flow through its cooling rails is changed. After the temperature becomes stable the partial beam rates are measured for about an hour at constant temperature of the cell and constant beam intensity of the atomic beam source. This is then done for various temperatures.

The partial beam rates need to be corrected by the function $g(T)$. This function can be derived from an unpolarized temperature scan where hydrogen or deuterium gas is injected by the unpolarized gas feed system (UGFS) instead of the atomic beam source. The UGFS injects only molecular gas with a constant intensity into the storage cell so that a variation of the molecular beam rate in the TGA refers to a temperature effect. The function $g(T)$ describing the temperature dependence can be determined by a fit to the measured total beam rate versus the cell temperature as shown in figure 3.11. On the left side the total beam rate – which is,

[17]These beam losses have a comparatively high probability to happen close to the HERMES target region as the collimator C2 (see chapter 3.1) is the most narrow part of the electron storage ring.

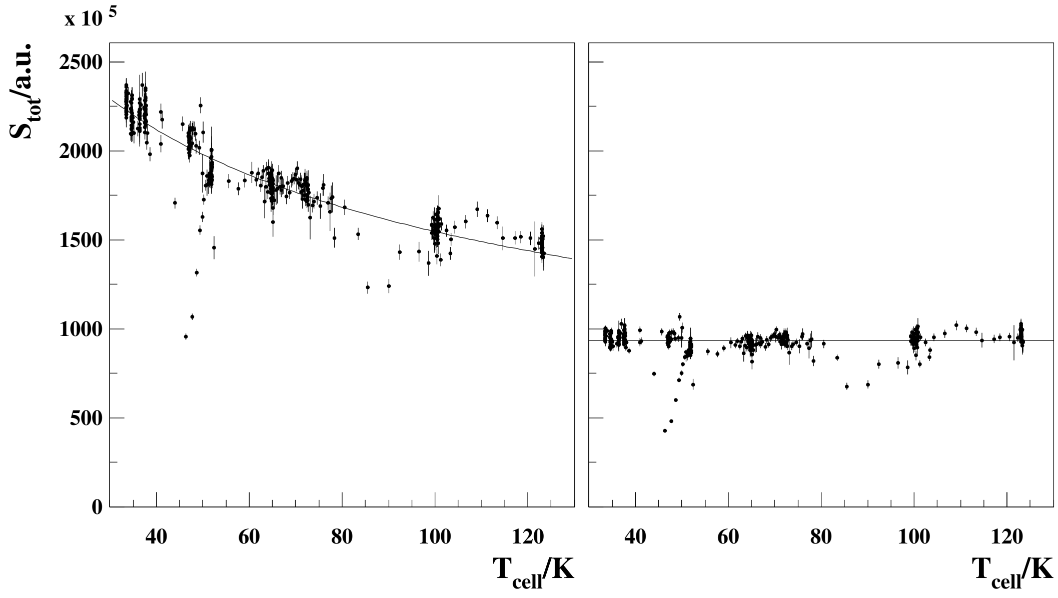

Figure 3.11: Plot of the total beam rate S_{tot} (corrected for emission current I_{emis} and beam intensity from the UGFS) for a temperature scan with unpolarized molecular deuterium. Left: The solid line indicates the fitted temperature correction function $g(T)$. Right: The same data after applying the temperature correction as found in the left figure.

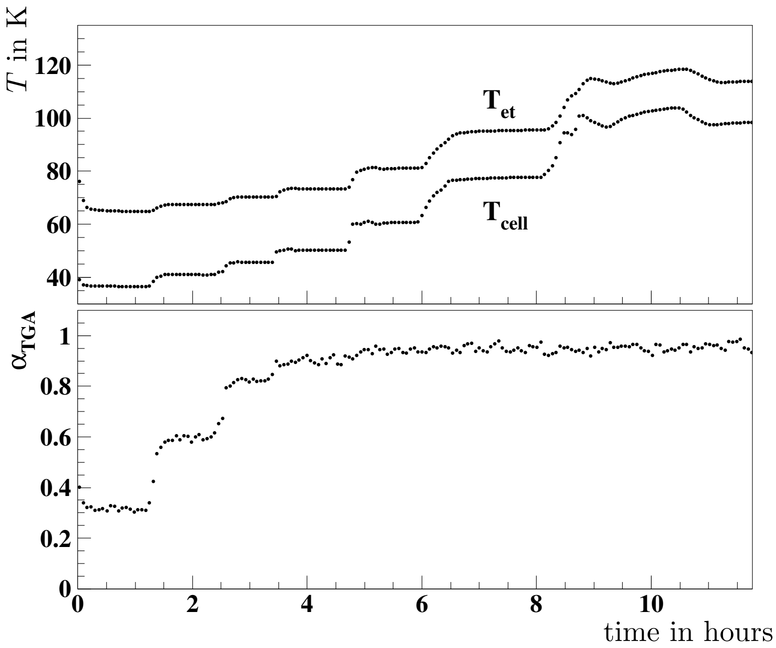

Figure 3.12: Data from a polarized temperature scan from August 1999 with deuterium. The temperature steps shown in the upper plot result in steps in the measured atomic fraction α^{TGA} in the lower plot.

in the case of a purely molecular target, similar to the molecular beam rate – corrected for emission current I_{emis} and beam intensity from the UGFS is plotted versus the cell temperature. The data on the right side is corrected by the fitted temperature dependence. The fitted correction function $g(T)$ is a function of the temperature of the extension tube, as all particles

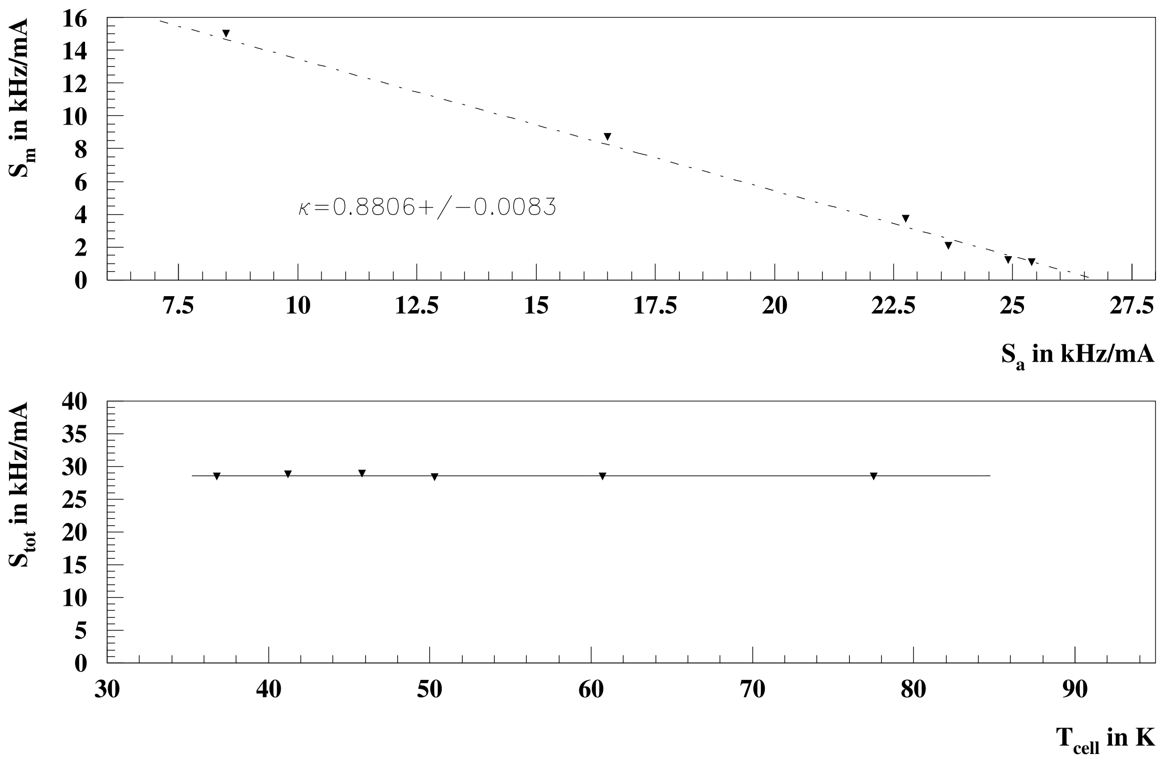

Figure 3.13: Analysis of the data from a temperature scan seen in figure 3.12. The upper plot shows the derivation of κ as seen in figure 3.10. The data points are averaged for constant temperatures and the measured beam rates are corrected for temperature and emission current. The lower plot shows $S_{\rm tot}$ (equation (3.7)) versus the cell temperature proving the validity of the calibration.

entering the ionizing volume of the TGA are thermalized by the extension tube as mentioned above. The temperature of the extension tube $T_{\rm ext}$ – measured by a thermocouple attached to the extension tube at the farest distance to the center of the storage cell – is higher than the cell temperature as the thermal contact to the cooling rails is unknown and the dipole magnet around the extension tube is at 300 K and causes a heating of the extension tube by radiation. The temperature correction function found from figure 3.11 is remarkably simple:

$$g(T_{\rm ext}) = \sqrt{\frac{T_{\rm ext}}{T_{\rm fit}}}\ , \tag{3.16}$$

with the fitted temperature $T_{\rm fit} \simeq 300$ K. These measurements have to be repeated after significant changes to the storage cell because the thermal contact between extension tube and cooling rails may change.

With the two correction functions $g(T)$ from equation (3.16) and $f(B, I_{\rm emis})$ from figure 3.9 it is now possible to display the data of a polarized temperature scan as shown in figure 3.10. One

dataset from a polarized temperature scan with deuterium gas from August 1999 is shown in figure 3.12. The upper plot shows the different temperature steps where the temperature of the extension tube is always above the cell temperature as explained above, whereas the lower plot shows the corresponding change in α^{TGA}. Figure 3.13 shows the determination of κ after the data points for each temperature step have been averaged. A cross check of the calibration is the plot of equation (3.13) versus the cell temperature to show the constance of ϕ_{tot} and thus the validity of the calibration.
Seven reliable temperature scan calibrations of the target gas analyzer have been made in the deuterium running period between August 1998 and September 2000 resulting in an averaged κ of

$$\kappa = 0.861 \pm 0.024 \ . \tag{3.17}$$

Method 2: HERA Beam Losses

As the cell temperature and the emission current of the filament in the ionizing volume of the quadrupole mass spectrometer are not influenced by an accidental loss of the HERA electron/positron beam near the HERMES target region, one can apply the observed partial beam rates $S_{a,m}$ without corrections to a plot of equation (3.12). The inverse negative slope of the fitted line in figure 3.14 is identical to $\sqrt{2}\kappa$. A beam loss causes a sudden and sharp drop of α^{TGA}. After the beam loss α^{TGA} increases slowly with the running of the atomic beam source due to the recovery of the water layer on the cell surface. Due to the uncertainties in the knowledge of the temperature of the extension tube and the model describing it, the calibration with the beam loss data can assumed to be more reliable. For the deuterium running period from August 1998 to September 2000 in total three reliable beam loss calibrations could be made all being consistent and giving an averaged κ of

$$\kappa = 0.859 \pm 0.007 \tag{3.18}$$

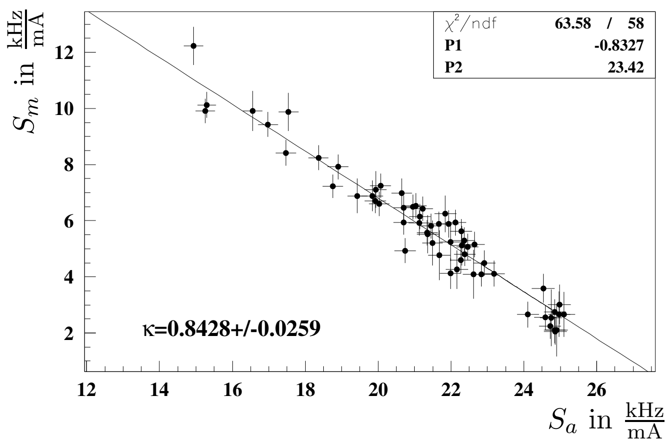

Figure 3.14: Molecular rate S_m of the TGA versus atomic rate S_a after a beam loss of the HERA beam in August 1999. The inverse negative slope of the linear fit is equal to $\sqrt{2}\kappa$. The atomic fraction α^{TGA} dropped to 0.3 after the beam loss and recovered to about 0.9 within about 3 hours. The temperature of the storage cell was constant all the time.

which in perfect agreement with the result for κ from the performed temperature scans in that period as given in equation (3.17). Details about the TGA calibrations during the deuterium running period can be found in [Bru 01].

3.5.2 The Initial Atomic Fraction α_0^{TGA}

In order to calculate the target polarization following equation (1.6) it is necessary to separate the fraction of nucleons being injected into the storage cell as atoms (α_0) and the fraction of nucleons in atoms surviving recombination (α_r). α^{TGA} then also consists of two contributions and with equation (3.11) can be written as

$$\alpha^{\mathrm{TGA}} = \frac{\phi_a}{\phi_a + \phi_m} = \alpha_0^{\mathrm{TGA}} \cdot \alpha_r^{\mathrm{TGA}} \ . \tag{3.19}$$

As long as dissociative ionization can be neglected the only source of the atomic flux ϕ_a into the target gas analyzer is the flux originating from the atomic beam source. The molecular flux ϕ_m however may have several sources:

$$\phi_m = \phi_r + \phi_{ball} + \phi_{rg} \ . \tag{3.20}$$

- Molecules, which are produced by recombination of two polarized atoms on the surface of the storage cell. The polarization of the recombined molecules devided by the polarization of the atoms is described by the factor β. Recombined molecules constitute the flux ϕ_r into the target gas analyzer.

- Molecules, which are injected into the cell by the atomic beam source. As the degree of dissociation of the dissociator is less than 100% and not all the molecules are pumped away due to the finite pumping speed of the vacuum system, a fraction of molecules enters the storage cell by means of ballistic flow, causing the flux ϕ_{ball} into the target gas analyzer. These molecules are unpolarized.

- Molecules from the residual background gas of the target chamber entering the storage cell. These molecules are also unpolarized as they have left the holding field of the target magnet and experienced a high number of collisions with the stainless steel wall of the target chamber. Residual gas molecules result in the flux ϕ_{rg} into the target gas analyzer.

To separate polarized and unpolarized molecules one can define the fraction of atoms surviving recombination α_r^{TGA} and the initial atomic fraction α_0^{TGA} as measured by the TGA by rewriting equation (3.19) using equation (3.20):

$$\alpha_r^{\mathrm{TGA}} = \frac{\phi_a}{\phi_a + \phi_r} \tag{3.21}$$

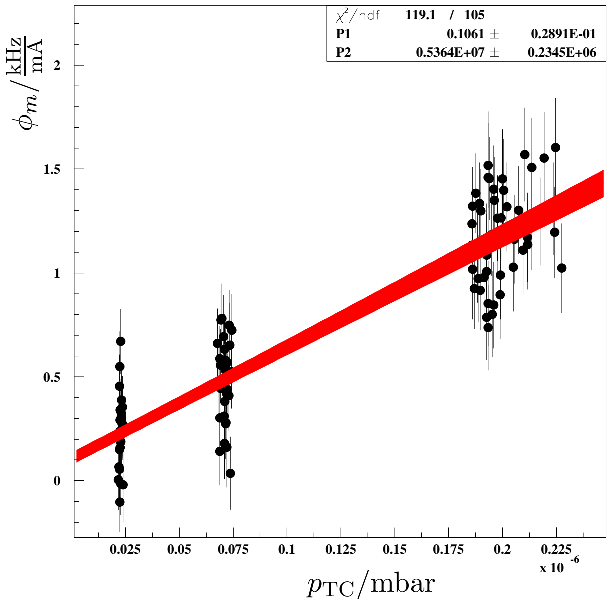

Figure 3.15: Measurement of the residual gas correction. The intensity of a molecular deuterium beam injected into the target chamber by the UGFS is stepwise increased. The molecular flow rate ϕ_m of the TGA increases with the target pressure. The fitted slope yields the residual gas calibration constant c_{rg}. This data has been measured in 2000 with deuterium.

and

$$\alpha_0^{\text{TGA}} = \frac{\phi_a + \phi_r}{\phi_a + \phi_r + \phi_{ball} + \phi_{rg}} . \tag{3.22}$$

The flow rate ϕ_{rg} caused by residual gas from the target chamber is proportional to the target chamber pressure p_{TC}:

$$\phi_{rg} = c_{rg} \cdot p_{\text{TC}} . \tag{3.23}$$

The proportionality factor c_{rg} can be determined by changing the target chamber pressure and measuring the molecular flow into the TGA. The fitted slope of ϕ_m versus p_{TC} then yields the residual gas calibration constant c_{rg}. For this purpose, molecular hydrogen or deuterium gas is injected directly into the target chamber by the unpolarized gas feed system (UGFS). This allows a variation of the background pressure with the corresponding gas type. Due to instabilities in the pressure gauge readings this type of residual gas calibration is repeated periodically. An example for a residual gas calibration is shown in figure 3.15, resulting in a calibration constant of $c_{rg} = 5.364 \pm 0.235 \cdot 10^{-6}\ \frac{\text{kHz}}{\text{mA}\cdot\text{mbar}}$.

In order to derive the amount of molecules which are ballistically injected by the atomic beam source one has to separate them from other sources of molecules. The ballistic flux ϕ_{ball} does not change while the dissociator is running in stable operation. The high frequency transitions between the sextupole magnet system of the atomic beam source (ABS) can be used to change the atomic flux into the storage cell as described in the tables 3.2 and 3.1. On the other hand, the molecular flux stays the same because the sextupole magnets do not influence the trajectories

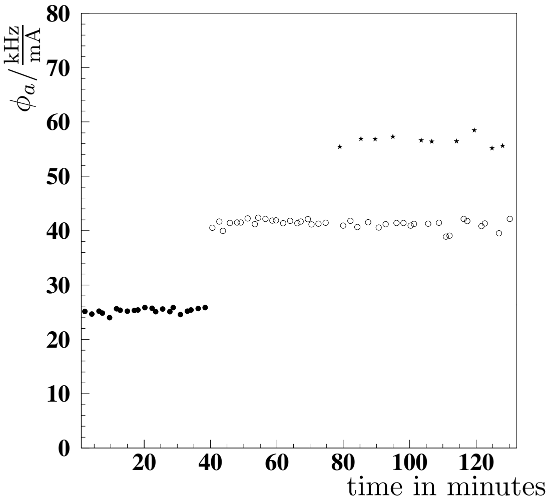

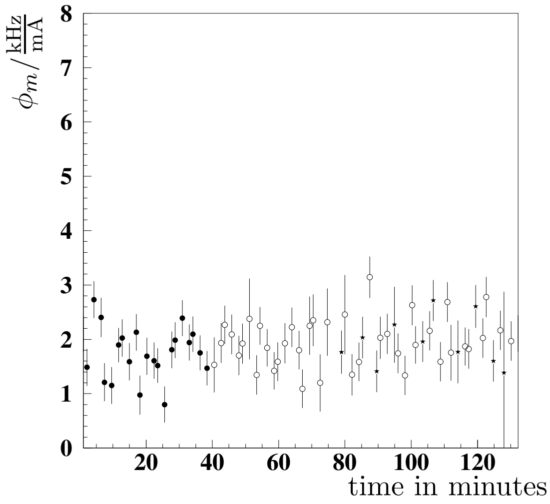

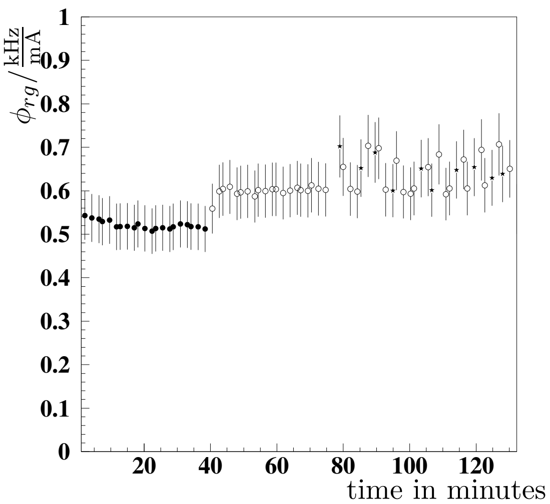

Figure 3.16: Measurement of the flowrates ϕ_a and ϕ_m in three different injection modes of the ABS for the determination of the ballistic flowrate ϕ_{ball}, performed in 2000 with deuterium. All injection modes as listed in table 3.2 have been used, where the filled circles correspond to single state injection, the open circles correspond to two state injection and the stars are measurements with three states injected. ϕ_{rg} in the last figure has been calculated from the target chamber pressure following equation (3.23).

of molecules. Depending on the injection mode (i) of the ABS, equation (3.20) may thus be written as

$$\phi_m^{(i)} = \phi_r^{(i)} + \phi_{ball} + \phi_{rg}^{(i)} \ , \tag{3.24}$$

with $\phi_{ball} = \text{const}$. Rewriting equation (3.21) as

$$\phi_r^{(i)} = \left(\frac{1}{\alpha_r^{\text{TGA}}} - 1 \right) \phi_a^{(i)} \tag{3.25}$$

then leads to

$$\phi_m^{(i)} - \phi_{rg}^{(i)} - \phi_{ball} = \left(\frac{1}{\alpha_r^{\text{TGA}}} - 1 \right) \phi_a^{(i)} \ . \tag{3.26}$$

For the determination of ϕ_{ball} two different injection modes of the atomic beam source are chosen with $\phi_a^{(1)} < \phi_a^{(2)}$. The corresponding values for $\phi_m^{(i)}$ and $\phi_a^{(i)}$ are measured with the TGA. $\phi_{rg}^{(i)}$

is calculated from the measured pressure in the target chamber p_{TC} using equation (3.23). By deviding the two equations (3.26) one obtains

$$\phi_{ball} = \frac{(\phi_m^{(1)} - \phi_{rg}^{(1)})\phi_a^{(2)} - (\phi_m^{(2)} - \phi_{rg}^{(2)})\phi_a^{(1)}}{\phi_a^{(2)} - \phi_a^{(1)}} \; . \tag{3.27}$$

To achieve the best possible precision, the difference in the injected atomic flux ϕ_a should be as large as possible. For this purpose one uses P_e and the single state injection modes in case of deuterium and P_e and the no-state injection mode P_{no} in case of hydrogen[18]. Figure 3.16 shows an example of the technique described to measure the ballistic flow which resulted a value of $\phi_{ball} = 0.31 \pm 0.08$ kHz/mA. These measurements have been performed in 2000 using deuterium gas with different injection modes of three, two and single hyperfine states. The necessary settings of the high frequency transitions in the atomic beam source (ABS) can be infered from table 3.2. The relative change in the residual gas contribution and thus in the target chamber pressure is smaller than in the atomic flowrate. The reason for that behaviour is that a fraction of the defocussed atoms by the ABS sextupole magnet system ends up in the appendix of the ABS and from there diffuses into the target chamber. Even though these atoms do not enter the storage cell ballistically they contribute to the target chamber pressure.

3.6 Breit-Rabi Polarimeter (BRP)

The atomic polarization of the gas sample leaving the cell through the sample and extension tube can be calculated using equations (2.16) and (2.18) after determining the hyperfine population of the sample beam. For this purpose the HERMES experiment uses a Breit-Rabi polarimeter [Gau 92, Bra 95, Bau 02b].

The Breit-Rabi polarimeter (BRP) is located along the axis of the extension tube. The detection unit for the atomic sample beam is similar to the system in the target gas analyzer (TGA) consisting of a chopper, a cross beam ionizer, a quadrupole mass spectrometer (QMS) and a channel electron multiplier (CEM) for single ion detection. The detected atomic beam rate is affected by two adiabatic high frequency transition (HFT) units as described in chapter 2.2 and a system of two sextupole magnets (see figure 3.17).

The HFT units and the sextupole magnets are located in the first vacuum chamber (*sextupole chamber*) while a second separable vacuum chamber contains the beam chopper and the detector (*detection chamber*). Both chambers form a differential pumping system with typical residual

[18]Since P_{no} injection was not possible during the running period with hydrogen in 1996/1997 due to the missing SFT between the sextupole systems, also the single state modes have been used for that purpose. A P_{no} mode does also not exist for the deuterium running period as with the existing HFTs between the sextupole magnet systems one cannot remove all three states from the atomic beam.

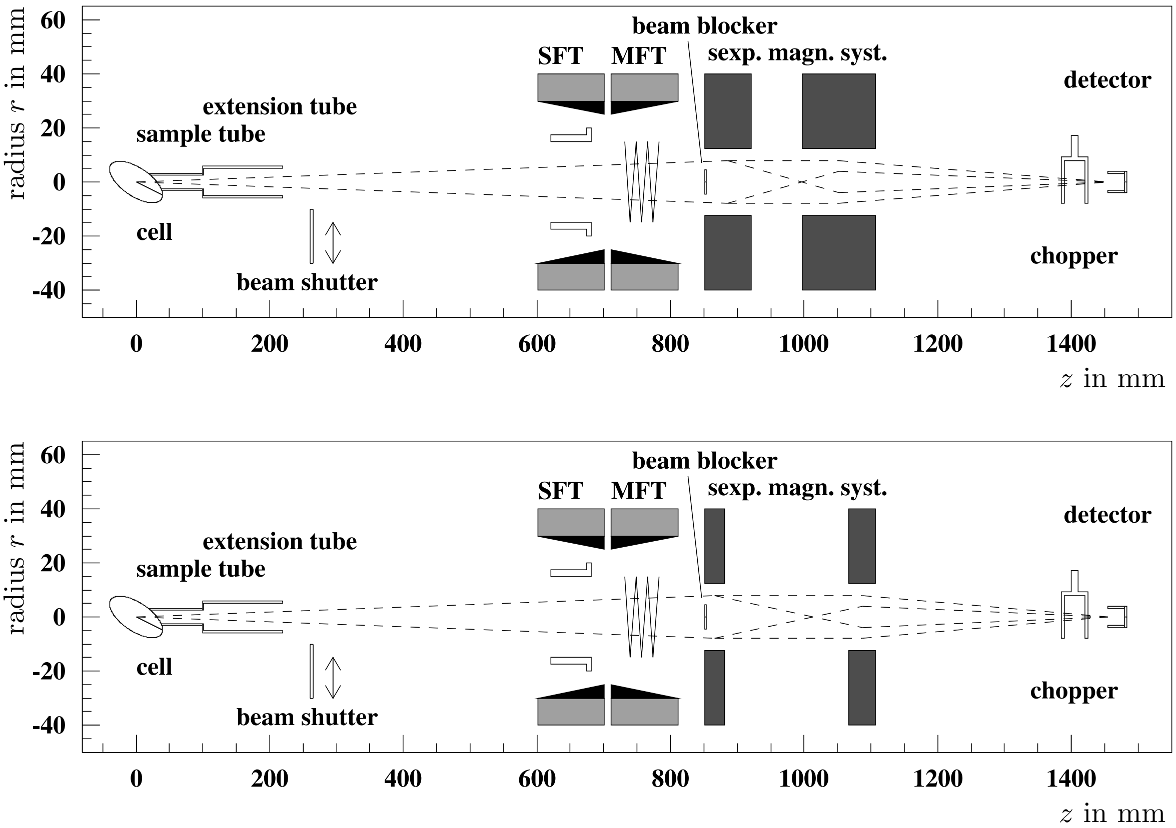

Figure 3.17: Schematic view of the Breit-Rabi polarimeter (BRP) where r is the radial distance to the extension tube axis and z the distance to the cell center along this axis. The particles leaving the extension tube pass two high frequency transition units and are then electron spin selectively separated by the system of two sextupole magnets and focussed to the detector if $m_S = +\frac{1}{2}$. The beam blocker suppresses the transmission of particles with $m_S = -\frac{1}{2}$ that are close to the axis of the magnets where the magnetic force is very weak. The upper plot shows the setup with the sextupole system until September 2000 while the lower plot shows the new optimized setup. The new setup was chosen to optimize the total intensity of the BRP signal (see chapter 3.6.3).

pressures of $2 \cdot 10^{-9}$ mbar in the sextupole chamber and $2.5 \cdot 10^{-10}$ mbar in the detection chamber. Details including the setup of the BRP and TGA vacuum system can be found in appendix A. Two high frequency transition units are applied, first a strong field transition (SFT) followed by a medium field transition (MFT). While the MFT can be used for π transitions[19], the SFT is able to induce both σ and π transitions as its resonator cavity has tilted resonators which provide magnetic field components parallel as well as perpendicular to the static magnetic field.

[19]See chapter 2.2 for details about the possible high frequency transitions.

This differs from the SFT units used in the atomic beam source (ABS). The selection of the transition type is realized by the setting of the static magnetic field. The frequency of the high frequency transition unit stays constant. To find the necessary setting of both static and gradient magnetic field, the beam intensity is observed while scanning the static field at a given gradient field. For matching field values a resonance can be seen by a drop of the count rate for those field values. If the plateau of the resonance is deep and broad enough, these settings are chosen for a standard operation of such a transition type. An optimization of the impedance matching of the MFT unit is done with an external Collins filter (also called π-filter [Mei 92]), whereas the SFT unit is kept in resonance with a feedback loop using a balance mixer to match the phases of the pickup signal and the high frequency entering the resonator. Pickup loops are used to monitor the high frequency amplitude in all transition units.

To align the whole setup of the BRP to the axis of the extension tube an optical telescope can be mounted on the BRP beam axis at the end of the detection chamber. For this procedure the beam blocker, which is located at the entrance of the first sextupole magnet, defines the axis in combination with an alignment cross at the end of the second sextupole magnet.

The sextupole magnet system focusses atoms entering the first magnet with $m_S = +\frac{1}{2}$ into the ionizing volume of the QMS. The focussing effect depends on the velocity of the passing atoms and thus on the temperature of the storage cell as all particles entering the BRP are thermalized with the storage cell walls due to wall bounces in the cell. Hence any sextupole system has an optimal focussing effect for a certain velocity of the passing particles only. Since at cell temperatures lower than 100 K the transmission of the magnet system into the ionizing volume of the QMS gets very low, a new magnet system was designed with the goal of a maximum BRP signal for temperatures between 30 K and 100 K. This topic will be discussed in detail in chapter 3.6.3. Both setups of the BRP are shown in figure 3.17.

The count rate detected by the BRP is proportional to the beam intensity into the BRP. The constant between measured rate and incoming intensity shall be named c in the following context and depends on the geometrical acceptance, detection efficiency of the QMS etc.

The difference to the TGA is that the measurement of the BRP can be affected by a water or molecular hydrogen beam into the detector of the BRP, which causes an apparent atomic signal by means of dissociative ionization. To correct for this effect a beam shutter was installed behind the extension tube which can block the path to the BRP remotely whereas the path to the TGA is not influenced. Measuring the BRP beam rate with a closed beam shutter gives the *background beam rate* which is then subtracted from all other beam rates to take only atoms into account that come from the storage cell. A set of measured beam rates for different transition states of both high frequency transition units is then used to derive the hyperfine population. For the use of any hyperfine transition (i) in the BRP the detected beam rate can be written as

$$S_{(i)} = c \cdot \sum_a \left(\sum_b \sigma_b T^{ab}_{(i)} \right) I_a \ , \tag{3.28}$$

with the transmission probability σ_b of an atom in hyperfine state $|\, b \,\rangle$ through the sextupole magnet system and the intensity I_a of an atom in state $|\, a \,\rangle$. The matrix T^{ab} contains the effect of a hyperfine transition a↔b and was defined by equation (2.22). The complete effect of all selected hyperfine transitions and the sextupole magnets can be described using the *measurement matrix* M^{ia}:

$$S_{(i)} = c \cdot \sum_a M^{ia} I_a \ . \tag{3.29}$$

Collecting more signals than unknowns with a set of at least five (seven) different beam rates $S_{(i)}$ in case of hydrogen (deuterium) the intensities I_a can be calculated with the help of the pseudoinverse matrix [Brn 92]

$$R = (M^T G_S M)^{-1} M^T G_S \ , \tag{3.30}$$

where G_S is the inverse covariance matrix of the measured signals C_S:

$$C_S = \begin{pmatrix} \ddots & & 0 \\ & (\sigma_S)_i^2 & \\ 0 & & \ddots \end{pmatrix} \tag{3.31}$$

where $(\sigma_S)_i$ is the statistical uncertainty of the measured signal $S_{(i)}$. Rewriting equation (3.29) leads to

$$I_a = \frac{1}{c} \cdot \sum_i R^{ai} S_{(i)} \ , \tag{3.32}$$

and with the total intensity I_{tot} being the sum over all hyperfine states one obtains the hyperfine population numbers of the sample beam N_a by

$$N_a = \frac{I_a}{\sum_a I_a} = \frac{I_a}{I_{tot}} \ . \tag{3.33}$$

Hence following equations (2.16) and (2.18) the polarizations can be calculated by

$$(P_e, P_z)^T = M_P^H (N_1, N_2, N_3, N_4)^T \tag{3.34}$$

and accordingly

$$(P_e, P_z, P_{zz})^T = M_P^D (N_1, N_2, N_3, N_4, N_5, N_6)^T \tag{3.35}$$

with

$$M_P^H = \begin{pmatrix} 1 & \cos 2\theta & -1 & -\cos 2\theta \\ 1 & -\cos 2\theta & -1 & \cos 2\theta \end{pmatrix} \tag{3.36}$$

and

$$M_P^D = \begin{pmatrix} 1 & \cos 2\theta_+ & \cos 2\theta_- & -1 & -\cos 2\theta_- & -\cos 2\theta_+ \\ 1 & \sin^2\theta_+ & -\cos^2\theta_- & -1 & -\sin^2\theta_- & \cos^2\theta_+ \\ 1 & -\frac{1}{2}(3\cos 2\theta_+ + 1) & \frac{1}{2}(3\cos 2\theta_- - 1) & 1 & -\frac{1}{2}(3\cos 2\theta_- + 1) & \frac{1}{2}(3\cos 2\theta_+ - 1) \end{pmatrix} . \tag{3.37}$$

If the statistical error of the beam rates $S_{(i)}$ of the BRP is given by the covariance matrix C_S one can calculate the covariance matrix of the intesities C_I by

$$C_I = R\, C_S\, R^T = (M^T\, C_S^{-1}\, M)^{-1} \; . \tag{3.38}$$

The covariance matrix C_N of the hyperfine populations N_a is then given by

$$C_N^{ab} = \sum_{c,d} \left(\frac{\partial N_a}{\partial I_c}\right) C_I^{cd} \left(\frac{\partial N_b}{\partial I_d}\right) \; , \tag{3.39}$$

and the covariance matrix of the polarization vector can be calculated by

$$C_P = M_P^{H,D}\, C_N\, (M_P^{H,D})^{-1} \; . \tag{3.40}$$

Summing over all elements of the covariance matrix C_I gives the statistical error of the total intensity

$$\Delta I_{tot} = \sum_{a,b} C_I^{ab} \; . \tag{3.41}$$

3.6.1 Calibration of the BRP

The analyzing power of the Breit-Rabi polarimeter (BRP) depends on the efficiencies of the high frequency transitions and the transmission probabilities of the sextupole magnet system for all hyperfine states. A calibration of the BRP includes the determination of these values. Each individual transition has to be described by a separate efficiency ε as discussed in chapter 2.2. For example a MFT 2-3 transition in case of hydrogen has to be described by two efficiencies: one for the 1-2 transition (ε_{m13r12}) and another for the 2-3 transition (ε_{m13r23}). Although ε_{m13r12} should be zero because it is unwanted for the MFT 2-3 it still needs to be taken into account when describing this transition.

The two high frequency transition units are positioned very close to each other because of the limited available space. Therefore, the magnetic field values can not be controlled independently due to the crosstalk. For a measurement of the efficiencies of a medium field transition (MFT), both transition units (MFT and SFT) have to be operated at the same time so that the cross talk of the magnetic fields makes it necessary to choose the setting of the static field of the MFT separately for each SFT magnetic field setting. To avoid another MFT setup with the SFT unit not operated, the SFT static and gradient field are always set to the value of one of

Signal $S_{(i)}$	SFT 1-4		SFT 2-4		MFT 1-3	MFT 2-3
	HF	B	HF	B	HF+B	HF+B
off	—	—	—	—	—	—
s14	X	X	—	—	—	—
s24	—	—	X	X	—	—
m13cs14	—	X	—	—	X	—
m23cs14	—	X	—	—	—	X
m13cs24	—	—	—	X	X	—
m23cs24	—	—	—	X	—	X
m13s14	X	X	—	—	X	—
m23s14	X	X	—	—	—	X
m13s24	—	—	X	X	X	—
m23s24	—	—	X	X	—	X

Table 3.3: Switching modes of the BRP and corresponding signals in case of hydrogen. 'HF' indicates the high frequency amplitude and 'B' the static and gradient magnetic fields where an 'X' stands for the activated state of the corresponding hardware. In a calibration all 11 signals are measured while for a polarization measurement only a subset of 6 signals is used.

the transitions. This is indicated by an additional index 'c' which is called 'calibration switch'. A MFT 1-3 transition operated alone with a magnetic field setting of the SFT as it is used for a SFT 1-4 would then be described by the index $_{m13cs14}$ whereas the index for both transitions operated together would be $_{m13s14}$. The SFT can be switched via the high frequency amplitude. It should be noted that the MFT does not affect the magnetic field in the SFT.

In case of hydrogen every MFT transition must be tuned separately for two different SFT field values (SFT 1-4 and SFT 2-4). In case of deuterium four different setups of each MFT transition are required, one for every possible SFT mode (SFT 1-6, SFT 2-6, SFT 3-5 and SFT 2-5). All that leads to the total number of efficiencies to be determined by a calibration measurement of $N_{eff} = 10$ for hydrogen and $N_{eff} = 41$ for deuterium. If the crosstalk of the magnetic fields could be avoided these numbers would significantly decrease to 6 for hydrogen and 14 for deuterium. The total number of measureable beam signals with the BRP including magnetic crosstalk is $N_{BRP} = 11$ in case of hydrogen and $N_{BRP} = 29$ in case of deuterium . Table 3.3 gives an overview over the signals of the BRP and their magnetic field settings in case of hydrogen. A similar overview for deuterium can be found in table 3.4.

The first calibration procedure made use of an additional sextupole magnet in front of the high frequency transition units of the BRP which rejected hyperfine states with $m_S = -\frac{1}{2}$ and reduced the number of unknowns [Bra 95]. Unfortunately the precision of this calibration method strongly depended on the values of the efficiencies and also suffered from limited statistics [Hen 98]. To achieve the required uncertainty of a calibration of less than 3% an alternative calibration method was developed which makes use of the possibility to run the atomic beam source (ABS) in a variety of different injection modes as listed in tables 3.2 and 3.1. If the

Signal $S_{(i)}$	SFT 1-6		SFT 2-6		SFT 2-5		SFT 3-5		MFT 1-4	MFT 2-4	MFT 3-4
	HF	B	HF	B	HF	B	HF	B	HF+B	HF+B	HF+B
off	—	—	—	—	—	—	—	—	—	—	—
s16	X	X	—	—	—	—	—	—	—	—	—
s26	—	—	X	X	—	—	—	—	—	—	—
s25	—	—	—	—	X	X	—	—	—	—	—
s35	—	—	—	—	—	—	X	X	—	—	—
m14cs16	—	X	—	—	—	—	—	—	X	—	—
m24cs16	—	X	—	—	—	—	—	—	—	X	—
m34cs16	—	X	—	—	—	—	—	—	—	—	X
m14cs26	—	—	—	X	—	—	—	—	X	—	—
m24cs26	—	—	—	X	—	—	—	—	—	X	—
m34cs26	—	—	—	X	—	—	—	—	—	—	X
m14cs25	—	—	—	—	—	X	—	—	X	—	—
m24cs25	—	—	—	—	—	X	—	—	—	X	—
m34cs25	—	—	—	—	—	X	—	—	—	—	X
m14cs35	—	—	—	—	—	—	—	X	X	—	—
m24cs35	—	—	—	—	—	—	—	X	—	X	—
m34cs35	—	—	—	—	—	—	—	X	—	—	X
m14s16	X	X	—	—	—	—	—	—	X	—	—
m24s16	X	X	—	—	—	—	—	—	—	X	—
m34s16	X	X	—	—	—	—	—	—	—	—	X
m14s26	—	—	X	X	—	—	—	—	X	—	—
m24s26	—	—	X	X	—	—	—	—	—	X	—
m34s26	—	—	X	X	—	—	—	—	—	—	X
m14s25	—	—	—	—	X	X	—	—	X	—	—
m24s25	—	—	—	—	X	X	—	—	—	X	—
m34s25	—	—	—	—	X	X	—	—	—	—	X
m14s35	—	—	—	—	—	—	X	X	X	—	—
m24s35	—	—	—	—	—	—	X	X	—	X	—
m34s35	—	—	—	—	—	—	X	X	—	—	X

Table 3.4: Switching modes of the BRP and corresponding signals in case of deuterium. 'HF' indicates the high frequency amplitude and 'B' the static and gradient magnetic fields where an 'X' stands for the activated state of the corresponding hardware. In a calibration all 29 signals (plus the beam shutter closed signal) are measured while for a polarization measurement only a subset of 10 signals (plus the beam shutter closed signal) is used.

ABS can be operated in N_{ABS} different modes and the signals in the BRP are measured for all possible modes, one obtains $N_{BRP} \cdot N_{ABS}$ equations with a total of $N_{eff} + N_\sigma + N_{HFS} \cdot N_{ABS}$ unknowns[20]. The resulting equation system can be solved if the degree of freedom N_f given by

$$N_f = (N_{BRP} - N_{HFS}) \cdot N_{ABS} - (N_{eff} + N_\sigma) \tag{3.42}$$

can be made positive.

For a calibration in case of hydrogen 7 ABS modes are used leading to $N_f = 38$. In case of deuterium two calibration modes can be used, one with 5 ABS modes (injecting 2 or 3 hyperfine states, compare table 3.2) leading to $N_f = 72$ and another one with 6 ABS modes (injecting single hyperfine states) leading to $N_f = 95$.

After introducing the vector of unknown parameters $x = (\varepsilon_i, \sigma_j, I_k)$, rewriting equation (3.29) results in

$$f(x) = M \cdot I - S = 0 \ , \tag{3.43}$$

where $f(x)$ is a vector of $N_{BRP} \cdot N_{ABS}$ different functions. Expanding the taylor series for $f(x)$ leads for every element $f_i(x)$ to

$$f_i(x) = f_i(x_0) + \sum_l \frac{\partial f_i}{\partial x_l}(x_l - x_l^{(0)}) + O^2(x_l) = 0 \ . \tag{3.44}$$

With the definition

$$A = \left(\frac{\partial f_i}{\partial x_l}\right) \tag{3.45}$$

equation (3.44) can be solved under the assumption that $O^2(x_l) \approx 0$:

$$x_l = x^{(0)} - (A^T A)^{-1} A^T \cdot f(x^{(0)}) \ . \tag{3.46}$$

Applying least square fits, this equation can be solved iteratively. The beam signals in the Breit-Rabi polarimeter have statistical uncertainties described by the covariance matrix C_S. Error weighting with $G_S = C_S^{-1}$ results in

$$x^{(i+1)} = x^{(i)} - (A^T G_S A)^{-1} A^T G_S \cdot f(x^{(i)}) \tag{3.47}$$

where $(A^T G_S A)^{-1} = C_x$ is the covariance matrix of the fit parameters with the following form:

$$C_x = \begin{pmatrix} C_{\varepsilon,\sigma} & C_{\varepsilon,\sigma,I} \\ C_{I,\varepsilon,\sigma} & C_I \end{pmatrix} \ . \tag{3.48}$$

Only the covariance matrix $C_{\varepsilon,\sigma}$ is used for the calculation of the systematic uncertainty of the polarization measurement. The χ^2-value that is minimized during the iteration process is defined by

$$\chi^2 = (S - M\,I)^T \cdot G_S \cdot (S - M\,I) \ . \tag{3.49}$$

[20] N_{HFS} is the number of hyperfine states and N_σ the number of relative transmission probabilities through the sextupole magnet system for the used gas type.

As C_S and thus G_S are diagonal matrices this formula simplifies to

$$\chi^2 = \sum_i \left(\frac{(S - M\,I)_i}{(\sigma_S)_i} \right)^2 \quad . \tag{3.50}$$

The covariance matrix C_I^{sys} of the systematic uncertainty of the intensities I_a is given by

$$C_I^{sys} = R\,A_\varepsilon C_\varepsilon A_\varepsilon^T R^T \tag{3.51}$$

where

$$A_\varepsilon = \left(\frac{\partial S_l}{\partial \varepsilon_m} \right) \quad \text{and} \quad R = M^{-1} = \left(\frac{\partial I_k}{\partial S_l} \right) \quad . \tag{3.52}$$

The propagation of the systematical error is then treated in the same way as described earlier for the statistical covariance matrix C_I.

There is no guarantee that this algorithm is convergent in all cases. It has been found to be only convergent in case of the BRP calibration with both gas types if the transmission probabilities of the sextupole magnet system were kept fixed. The attempt to fit both efficiencies and transmissions failed.

Nevertheless also the transmission probabilities can be derived by fitting them to the measured data. Due to the beam blocker in the BRP (see figure 3.17) the transmission probability of the hyperfine states with $m_S = -\frac{1}{2}$ is zero. For the evaluation of the hyperfine population and polarization the normalization allows to set one transmission probability to $\sigma_1 = 1$ and thus reduce the number of unknows by one. Then only the knowledge of the relative transmissions $r_{21} = \frac{\sigma_2}{\sigma_1}$ (and additionally $r_{31} = \frac{\sigma_3}{\sigma_1}$ in case of deuterium) is required.

For the hydrogen running period in 1996 and 1997 the ratio r_{21} was fitted to the data resulting [Bau 00, Hen 98]

$$r_{21} = 1.029 \pm 0.015 \tag{3.53}$$

at an operating temperature of the storage cell of 95 K. For other temperatures one has to know the temperature dependence of the ratio $r_{21}(T)$ which Baumgarten fitted to the measured data with a polynomial of third order:

$$r_{21}(T) = 0.972 + 0.075 \left(\frac{100\ \text{K}}{T} \right) - 0.025 \left(\frac{100\ \text{K}}{T} \right)^2 - 0.0022 \left(\frac{100\ \text{K}}{T} \right)^3 \quad . \tag{3.54}$$

As the critical field for deuterium is much smaller than for hydrogen ($B_C^D \simeq \frac{3}{13} \cdot B_C^H$) the difference of the Stern-Gerlach force for the hyperfine states with $m_S = +\frac{1}{2}$ vanishes in high fields. Numerical calculations showed that with a beam blocker of 9 mm diameter the ratios r_{21} and r_{31} can assumed to be unity with a maximum uncertainty less than 0.5%.

After the deuterium running period ended in 2000 the target hardware has been exchanged to be operated with hydrogen gas and a transversal magnetic holding field. At that time also a new sextupole magnet system has been installed into the Breit-Rabi polarimeter. Hence the ratios of transmission probabilities have potentially changed compared to the formerly used magnet system.

3.6.2 Alternative Calibration Method Using Simplex Optimization

In the previous chapter it was mentioned that the transmission ratios of the sextupole magnet system had to be kept constant in order to find a convergence of the algorithm, that analytically calculates the efficiencies from a BRP calibration measurement. In order to be able to derive all necessary parameters including the transmission ratios at the same time, an approach originating from evolutionary operation [Box 57] was adapted for the BRP calibration. The idea of evolutionary operation is to optimize unknown systems by making experiments with certain factor combinations, measuring the response of the system directly and using intelligent algorithms to propose the next (and potentially better) factor combination. The geometrical hyperplane with $k + 1$ corners in case of k independent factors, which moves through the factor space towards the optimal response, is called a *simplex* [Spe 62].
These evolutionary algorithms have mostly been developed for the use in industrial applications and can be found in [Wlt 91]. With only a few modifications they also become usable for scientific applications with a large number of factors in case of numerical instabilities using methods e.g. from the linear algebra. Many original algorithms only allow very small steps in factor space for economical reasons, as a new experiment (with a lot of risks and restrictions) is required at the new vertex, i.e. the next (and potentially better) factor combination.
Nevertheless algorithms have been developed for the use in research, which allow a fast convergence and therefore large steps in factor space. One of these algorithms is the variable size simplex algorithm, which allows the simplex to change its size during its path towards the optimum. The variable size of the simplex guarantees both fast convergence and high precision and is discussed in more detail in [Hen 02].
The rules for the simplex movement are described in appendix B. The optimum in case of the BRP calibration would be a minimum χ^2-value as defined by equation (3.50). The factors to be varied and optimized are then the efficiencies of the BRP hyperfine transition units and the transmissions of the sextupole magnet system. With the possibility to reach a very high precision, this approximative approach to the efficiencies and transmissions results in values, which do not show any significant deviation from the values calculated with the analytical approach as described in the previous chapter. The advantage of the variable size simplex optimization is the higher stability and flexibility with increasing number of unknowns. Especially in case of deuterium the analytical approach has been very sensitive to the starting conditions, which is not the case for the approach by evolutionary operation.
The analysis of a BRP calibration measurement from May 2000 produced the efficiencies and transmission ratios as shown in table 3.5. One can see that the measured signals by the BRP do not allow any systematic access to the efficiency of the 1-2 part of the MFT 3-4 transition

Efficiency	Value (New)	Value (Old)	Efficiency	Value (New)	Value (Old)
$\varepsilon_{\mathrm{m14r12c16}}$	0.894 ± 0.011	0.893 ± 0.010	$\varepsilon_{\mathrm{m14r12c25}}$	0.901 ± 0.011	0.904 ± 0.011
$\varepsilon_{\mathrm{m14r23c16}}$	1.008 ± 0.011	1.013 ± 0.011	$\varepsilon_{\mathrm{m14r23c25}}$	0.995 ± 0.016	1.012 ± 0.021
$\varepsilon_{\mathrm{m14r34c16}}$	0.921 ± 0.015	0.921 ± 0.016	$\varepsilon_{\mathrm{m14r34c25}}$	0.920 ± 0.010	0.921 ± 0.010
$\varepsilon_{\mathrm{m24r12c16}}$	0.010 ± 0.013	-0.019 ± 0.021	$\varepsilon_{\mathrm{m24r12c25}}$	0.000 ± 0.013	0.000 ± 0.012
$\varepsilon_{\mathrm{m24r23c16}}$	0.880 ± 0.012	0.878 ± 0.011	$\varepsilon_{\mathrm{m24r23c25}}$	0.881 ± 0.015	0.878 ± 0.014
$\varepsilon_{\mathrm{m24r34c16}}$	0.971 ± 0.017	0.965 ± 0.018	$\varepsilon_{\mathrm{m24r34c25}}$	0.978 ± 0.012	0.974 ± 0.012
$\varepsilon_{\mathrm{m34r12c16}}$	—	—	$\varepsilon_{\mathrm{m34r12c25}}$	—	—
$\varepsilon_{\mathrm{m34r23c16}}$	0.003 ± 0.010	0.002 ± 0.011	$\varepsilon_{\mathrm{m34r23c25}}$	0.021 ± 0.011	0.022 ± 0.011
$\varepsilon_{\mathrm{m34r34c16}}$	0.910 ± 0.017	0.912 ± 0.016	$\varepsilon_{\mathrm{m34r34c25}}$	0.951 ± 0.013	0.949 ± 0.014
$\varepsilon_{\mathrm{m14r12c26}}$	0.901 ± 0.015	0.905 ± 0.014	$\varepsilon_{\mathrm{m14r12c35}}$	0.899 ± 0.009	0.900 ± 0.010
$\varepsilon_{\mathrm{m14r23c26}}$	1.017 ± 0.019	1.028 ± 0.018	$\varepsilon_{\mathrm{m14r23c35}}$	1.001 ± 0.012	1.006 ± 0.012
$\varepsilon_{\mathrm{m14r34c26}}$	0.898 ± 0.010	0.901 ± 0.013	$\varepsilon_{\mathrm{m14r34c35}}$	0.923 ± 0.010	0.926 ± 0.012
$\varepsilon_{\mathrm{m24r12c26}}$	0.003 ± 0.009	-0.005 ± 0.009	$\varepsilon_{\mathrm{m24r12c35}}$	0.001 ± 0.011	-0.007 ± 0.010
$\varepsilon_{\mathrm{m24r23c26}}$	0.912 ± 0.010	0.914 ± 0.010	$\varepsilon_{\mathrm{m24r23c35}}$	0.910 ± 0.014	0.915 ± 0.013
$\varepsilon_{\mathrm{m24r34c26}}$	0.962 ± 0.013	0.967 ± 0.011	$\varepsilon_{\mathrm{m24r34c35}}$	0.969 ± 0.012	0.966 ± 0.014
$\varepsilon_{\mathrm{m34r12c26}}$	—	—	$\varepsilon_{\mathrm{m34r12c35}}$	—	—
$\varepsilon_{\mathrm{m34r23c26}}$	0.026 ± 0.015	0.025 ± 0.014	$\varepsilon_{\mathrm{m34r23c35}}$	-0.006 ± 0.015	-0.002 ± 0.013
$\varepsilon_{\mathrm{m34r34c26}}$	0.946 ± 0.012	0.942 ± 0.011	$\varepsilon_{\mathrm{m34r34c35}}$	0.891 ± 0.013	0.896 ± 0.012
$\varepsilon_{\mathrm{s16}}$	0.956 ± 0.012	0.958 ± 0.011	$\varepsilon_{\mathrm{s36}}$	0.789 ± 0.011	0.784 ± 0.013
$\varepsilon_{\mathrm{s26}}$	0.980 ± 0.010	0.977 ± 0.012	$\varepsilon_{\mathrm{s35}}$	0.955 ± 0.013	0.955 ± 0.014
$\varepsilon_{\mathrm{s25}}$	0.998 ± 0.009	0.998 ± 0.009			

Table 3.5: The table contains the list of transition efficiencies, which are needed to describe the BRP signals in case of deuterium and the corresponding results of a calibration measurement taken in May 2000. The new results have been determined using a variable size simplex algorithm and agree with the old results from the previously used method. The transmission ratios r_{21} and r_{31} have been fitted to be $r_{21} = r_{31} = 1.001 \pm 0.003$, which agrees nicely with the expectation from chapter 3.6.1.
The values of the $\varepsilon_{\mathrm{m34r12cxy}}$-efficiencies are missing because a BRP calibration measurement is not sensitive to these values. They can be neglected completely for the description of a BRP measurement.

($\varepsilon_{\mathrm{m34r12cxy}}$). The reason is that any transition between the hyperfine states $|1\rangle$ and $|2\rangle$ can not be observed by the BRP, unless a transition exchanging the population of state $|2\rangle$ with any state with $m_S = -\frac{1}{2}$ takes place after the MFT and before the atoms enter the sextupole magnet system. Otherwise a MFT 1-2 transition will not change the detected signal after the sextupole magnet system as $r_{21} = 1$.

3.6.3 The Total Intensity of the BRP I_{tot}

The temperature dependent total intensity $I_{\text{tot}}(T)$ of the BRP is defined by the properties of the sextupole magnet system. The knowledge about its structure is required in order to improve the statistical uncertainty of a polarization measurement by an increased total intensity. It is additionally relevant for the comparison of the atomic flux into the BRP and into the TGA. This will be of interest when trying to investigate the surface properties to restrict the possible sampling corrections in chapter 5 because TGA and BRP are sensitive to different parts of the storage cell which have different surface properties.

A setup of two sextupole magnets may focus the atoms to the detector along one of two different types of trajectories: Fast atoms will result in a parallel beam after the first magnet and then focussed into the detector by the second magnet. Atoms that are too slow will be deflected too strongly by the first magnet and cross the sextupole axis. Nevertheless there is also a small velocity window for these slower atoms as the second magnet may exactly compensate the increased deflection of the first magnet and thus still focus the atoms to the detector. Both velocity windows can be seen in figure 3.21 showing the transmission probability $P_\sigma(v)$ as a function of the velocity.

A new magnet system was designed to match the higher and broader of the two velocity windows of the magnet system to the velocities of the sample beam.

The velocity distribution in the target gas $N(v,T)$ is proportional to Maxwells velocity distribution $f(v,T)$ so that with a gas temperature T the number of atoms with a velocity between v and $v + \mathrm{d}v$ is given by

$$N(v,T)\,\mathrm{d}v \propto \; f(v,T)\,\mathrm{d}v = \left(\frac{m}{k_b T}\right)^{\frac{3}{2}} \cdot e^{-\frac{mv^2}{2k_bT}}\, v^2\,\mathrm{d}v \;. \tag{3.55}$$

The total beam intensity into the BRP is proportional to the integrated number of atoms $\dot{N}_v(v,T)\mathrm{d}v$ with velocities between v and $v+\mathrm{d}v$ entering the sextupole acceptance per unit time and the average probability $P_\sigma(v)\mathrm{d}v$ of these atoms to be focussed to the detector by the magnet system:

$$I_{\text{tot}} \propto \int_0^\infty \frac{1}{v}\, P_\sigma(v)\, \dot{N}_v(v,T)\,\mathrm{d}v \;, \tag{3.56}$$

with the factor $\frac{1}{v}$ originating from the detection probability in the QMS.

The total number of atoms entering the sextupole acceptance per unit time $\dot{N}_{\text{tot}}$ is given by the number of atoms per unit time injected by the ABS $\dot{N}_{\text{ABS}}$ and by the geometry, where $\Delta\Omega$ denotes the solid angle of the sextupole acceptance:

$$\dot{N}_{\text{tot}} \propto \dot{N}_{\text{ABS}}\Delta\Omega \;. \tag{3.57}$$

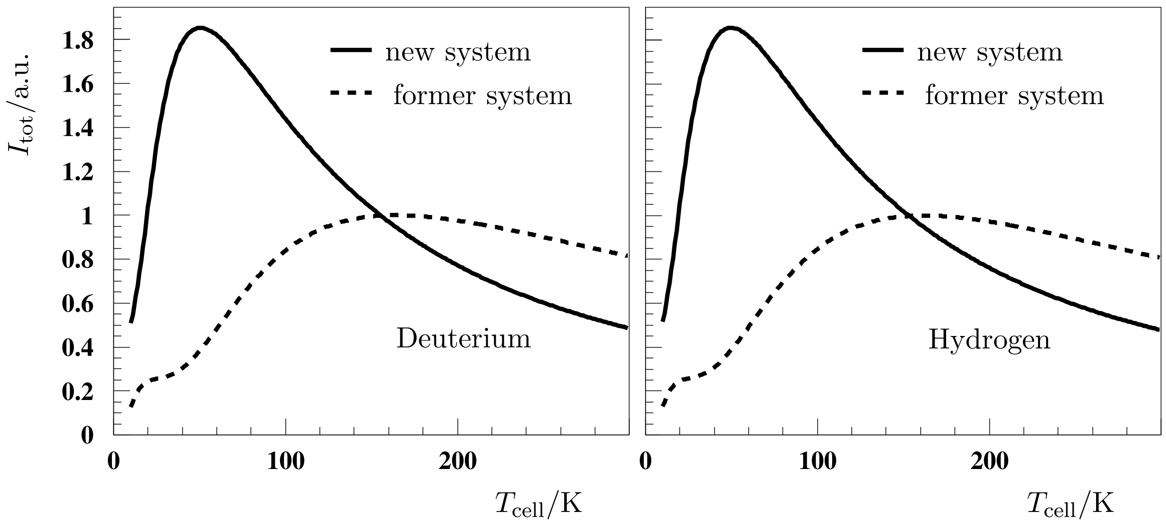

Figure 3.18: Simulated total transmission through the formerly used and the new magnet systems of the BRP for both gas types. A clear improvement is achieved for temperatures around and below the operating point ($T^H_{\rm cell} \leq 95$ K, $T^D_{\rm cell} \leq 60$ K). The hydrogen results have been renormalized to the deuterium results in order to allow an easier comparison of the gain factors, which are between 1.75 at 95 K and about 4 at 60 K.

As $\dot{N}_v(v,T)\,\mathrm{d}v$ is proportional to the flux density (which is given by the product of atomic density and their velocity v)

$$\dot{N}_v(v,T)\,\mathrm{d}v = \frac{\dot{N}_{\rm tot}}{\langle\, v\,\rangle}\, f(v,T)\, v\,\mathrm{d}v \ , \tag{3.58}$$

equation (3.56) can now be rewritten as

$$I_{\rm tot} \propto \frac{\dot{N}_{\rm tot}}{\langle\, v\,\rangle} \int\limits_0^\infty P_\sigma(v)\, f(v,T)\,\mathrm{d}v \ . \tag{3.59}$$

Simulations of the trajectories of atoms through the sextupole system of the BRP have been carried out. It was observed, also experimentally, that $I_{\rm tot}$ drops significantly at temperatures around and below the operating temperature of $T_{\rm cell} \simeq 95$ K. Aiming for the lowest possible statistical uncertainty in the low temperature region[21] a new setup of sextupole magnets has been found where the maximum of $I_{\rm tot}$ is at cell temperatures around $T_{\rm cell} \simeq 50$ K. The temperature dependences of $I_{\rm tot}$ simulated by a Monte-Carlo tracking program is shown in figure 3.18 for both gas types.

Nevertheless studies showed that a precise prediction is impossible because the relative alignment of the BRP and storage cell center (and thus the opening of the extension tube) changes

[21]Target studies concerning recombination and depolarization processes require cell temperatures of $T_{\rm cell} \leq$ 100 K to allow access to the recombination and spin relaxation parameters (see chapter 4).

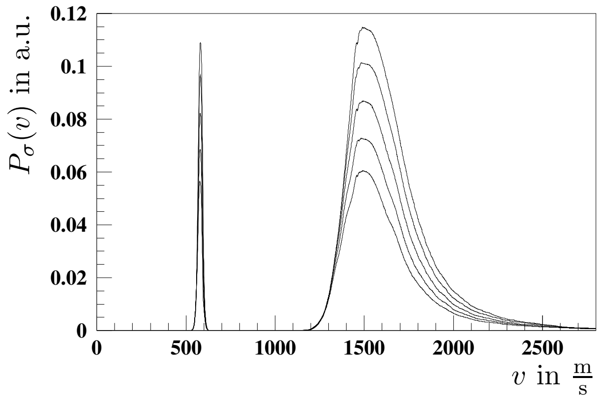

Figure 3.19: Simulated transmission function $P_\sigma(v)$ of the BRP sextupole magnet system atoms in state $|\,1\,\rangle$ for a relative misalignment between BRP and storage cell of 0, 0.25, 0.5, 0.75 and 1.0 mm (top to bottom). The unknown degree of misalignment makes measurements of $P_\sigma(v)$ necessary in order to understand $I_{\text{tot}}(T)$.

with the temperature of the cell which causes thermal contraction and therefore movement of the cell. The consequence of a relative misalignment between BRP and storage cell for the transmission function $P_\sigma(v)$ can be seen in figure 3.19. The degree of misalignment is not precisely measureable which causes large uncertainties in the theoretical prediction of $P_\sigma(v)$.
To understand the temperature dependence of I_{tot} completely it was therefore necessary to perform measurements of $P_\sigma(v)$.
In order to obtain the velocity distribution $P_\sigma(v)$, a beam modulation technique has been used to measure time of flight (TOF) spectra of atoms passing the sextupole magnet system of the BRP. For this purpose the BRP chopper was stopped in the *open* position and the signal in the BRP was measured by the time resolving counter (TRC) of the digital signal processor (DSP) board with 5 μsec bin length. The beam modulation was realized by switching the MFT 3-4 transition of the BRP for deuterium periodically on and off where the magnetic field values stayed constant and only the high frequency was switched. A programmable pulser was used to switch the high frequency of the MFT unit. The rising edge of the pulser signal was used to trigger the TRC. In order to obtain the best possible statistical precision the ABS was operated in injection mode P_z^- with the BRP SFT 3-5 permanently on so that (in the ideal case) only states $|\,3\,\rangle$ and $|\,4\,\rangle$ will enter the BRP. The SFT 3-5 then leaves only the states $|\,4\,\rangle$ and $|\,5\,\rangle$ in the sample beam which are defocussed by the sextupole system resulting in a vanishing signal in the BRP. The pulsed switching of the MFT 3-4 will leave states $|\,3\,\rangle$ and $|\,5\,\rangle$ in the sample beam which results an increased signal in the BRP as state $|\,3\,\rangle$ is focussed to the detector.
The detected signal in the BRP shows two steps caused by the two different drift times for the passage of the sextupole magnet system, where the later step originates from slower atoms. The integrated distribution of drift times results - beside a constant background - the time distribution of counts in the BRP detector, if the time that the high frequency of the MFT is on is larger than the maximal drift time of the atoms into the detector. The velocity of an atom is simply calculated by dividing the path length from the MFT 3-4 to the detector ($l \approx 610$ mm)

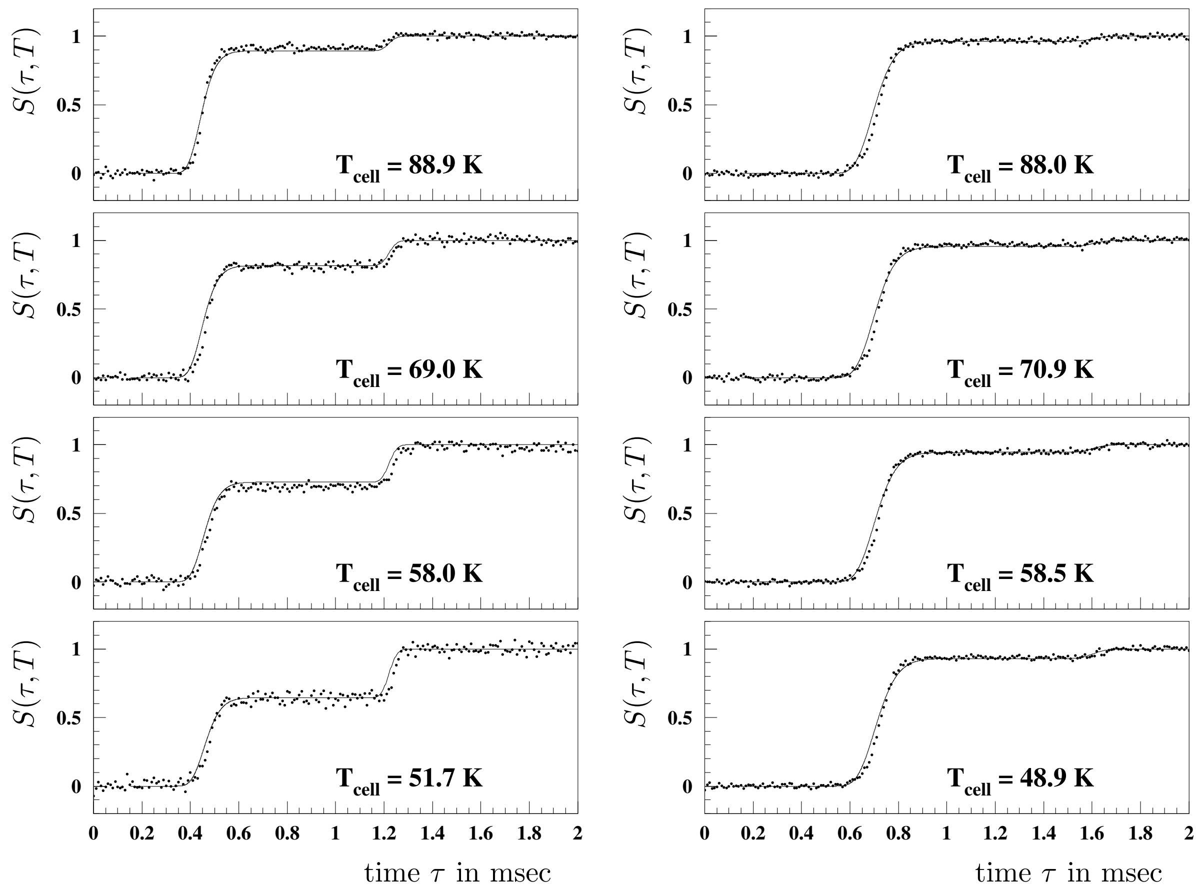

Figure 3.20: Results of a TOF measurement of deuterium atoms passing the former (left side) and new (right side) sextupole magnet system for 4 different storage cell temperatures. The plots show the scaled and normalized measured signal $S(\tau, T)$ as a function of the time τ (dots). The solid lines indicate calculated signal with a Maxwellian $f(v, T)$ and the parametrized velocity distribution $P_\sigma(v)$ from equation (3.62) with the parameters as listed in table 3.6 fitted to the measured TOF signals.

by the time it needed to travel along that path ($v = \frac{l}{t}$). The signal $S(\tau, T)$ at any given time τ is described by the integral

$$S(\tau, T) = \int_0^\tau \dot{N}(v, T)\, \frac{\mathrm{d}v}{\mathrm{d}t}\, \mathrm{d}t \qquad (3.60)$$

and was measured for 4 different storage cell temperatures for both magnet systems, the formerly one used until august 2000 and the newly installed system in 2001. The measured data points of these TOF measurements are shown in figure 3.20. Approximating the velocity windows in $P_\sigma(v)$ with Gaussians $g_i(v)$

$$g_i(v) = \frac{1}{\sigma_i \sqrt{\pi}} \cdot e^{-\frac{(v-v_i)^2}{\sigma_i^2}} , \qquad (3.61)$$

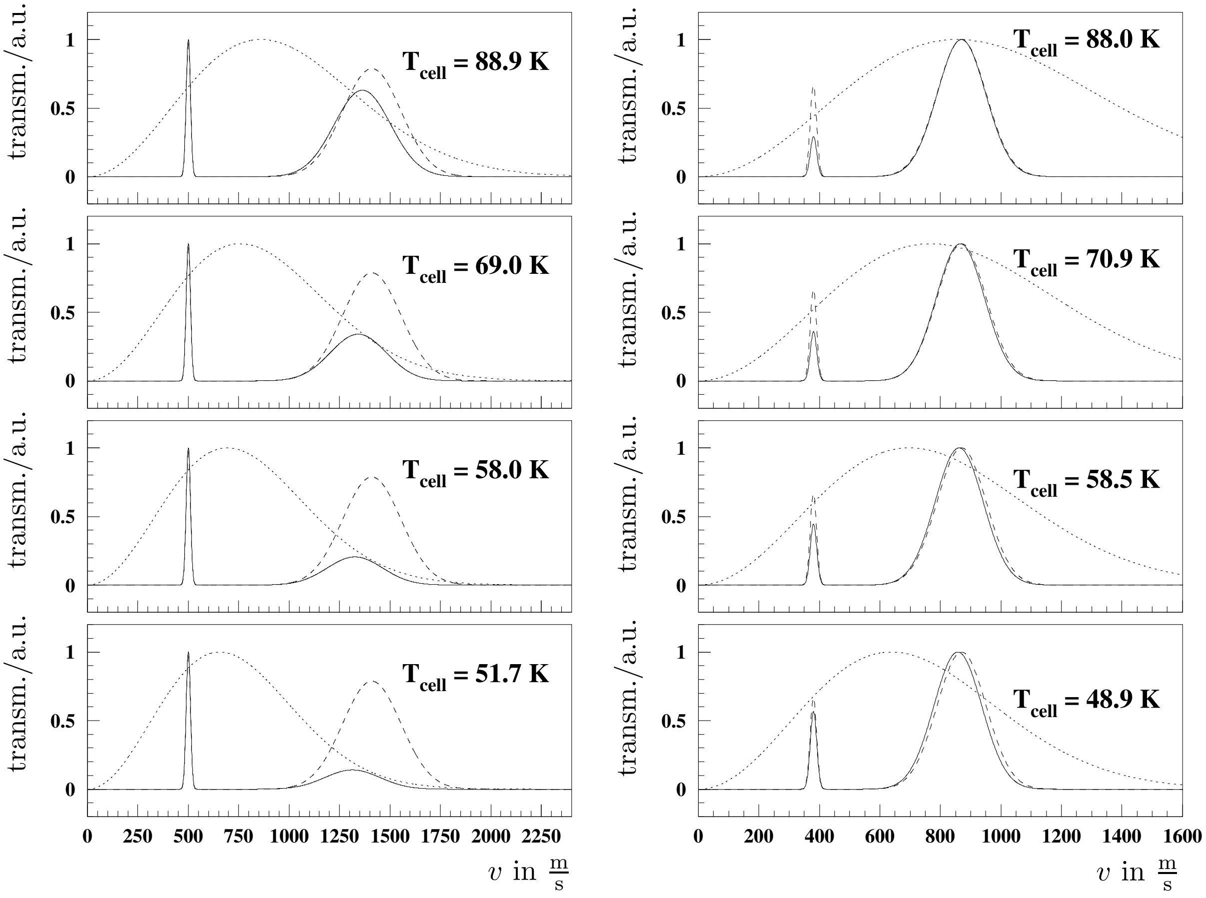

Figure 3.21: The velocity dependent transmissions through the sextupole magnet systems (old system on the left side and new system on the right side): The transmission function $P_\sigma(v)$ of equation (3.62) (dashed line), the Maxwellian velocity distribution $f(v,T)$ (dotted line) and the product of both (solid line).

the velocity distribution can be parametrized by

$$P_\sigma(v) = (1-f)g_1(v) + f\,g_2(v)\ . \tag{3.62}$$

The parameters have been fitted to the measured data as seen in figure 3.20. Table 3.6 shows the fitted parameters for both magnet systems. Figure 3.21 displays the velocity distribution $P_\sigma(v)$ as fitted to the measured data in figure 3.20 for the different temperatures of the storage cell. The

	Old System	New System
v_1	1321 $\frac{\mathrm{m}}{\mathrm{s}}$	875 $\frac{\mathrm{m}}{\mathrm{s}}$
σ_1	163 $\frac{\mathrm{m}}{\mathrm{s}}$	97 $\frac{\mathrm{m}}{\mathrm{s}}$
v_2	494 $\frac{\mathrm{m}}{\mathrm{s}}$	378 $\frac{\mathrm{m}}{\mathrm{s}}$
σ_2	13 $\frac{\mathrm{m}}{\mathrm{s}}$	15 $\frac{\mathrm{m}}{\mathrm{s}}$
f	0.935	

Table 3.6: Fitted parameters of $P_\sigma(v)$ as given in equation (3.62) for both the formerly used (old) and the new sextupole magnet system in the BRP.

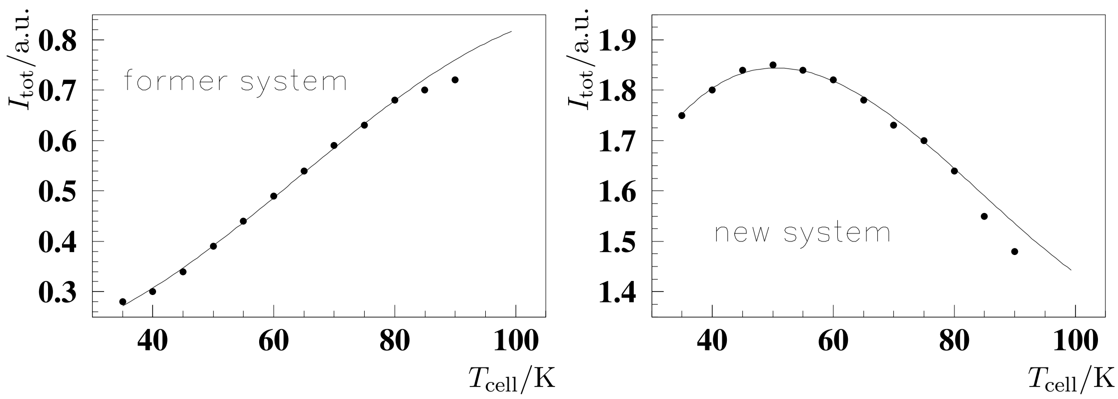

Figure 3.22: The solid line represents the simulated total transmission through the formerly used and the new magnet systems of the BRP for deuterium whereas the dots are calculated from TOF-measurements. For cell temperatures $T_{\mathrm{cell}} \leq 80$ K the measurements agree nicely with the results from the simulation. At higher temperatures the relative misalignment between the BRP and the sample tube axis becomes significant, leading to a divergence of measurement and prediction.

geometrical transmission $P_\sigma(v)$ (dashed line) with the two velocity windows (of approximated Gaussian shape) has to be weighted by a Maxwellian distribution (dotted line) resulting in the total transmission (solid line) of this model. It also shows how much better the upper velocity window of the new sextupole magnet systems fits with the Maxwellian velocity distribution for temperatures around the operating temperature of the storage cell. Taking the fluctuation of the measured data into account, the improved statistics achieved with the new magnets is obvious from figure 3.20. The measureable improvement becomes clearer with decreasing temperature of the storage cell.

The total intensity $I_{\mathrm{tot}}(T)$ can now be calculated using this model of $P_\sigma(v)$ and equation (3.59). As already mentioned the relative movement between the cell and the BRP by thermal expansion of the cell changes the BRP acceptance to this position significantly. Thus the results from the TOF measurements may only be compared to the simulated behaviour of $I_{\mathrm{tot}}(T)$ as seen in figure 3.18 for temperatures below about 80 K, where the thermal movement of the cell becomes negligible. The measured results of I_{tot} in case of deuterium for both magnet systems are compared with the simulated behaviour in figure 3.22. As mentioned the predicted behaviour by the simulation agrees nicely with the results from the measurements for the low temperature region $T_{\mathrm{cell}} \leq 80$ K. The good agreement with the simulations is important insofar, as one can use the comparison of the temperature corrected BRP intensity and the atomic flux ϕ_a of the

TGA to determine the recombination properties of the sample and extension tube, which is necessary to understand the sampling corrections for the HERMES target.

Chapter 4

Interactions inside the Storage Cell

Inside the storage cell the atoms of the target gas may experience several interactions, which have an influence on the average target polarization P^T. These interactions may be classified by:

- Recombination processes and
- Spin relaxation processes caused by:
  - Wall collisions,
  - Spin exchange collisions and
  - Resonant interaction of HERA beam and the target gas.

Recombination and relaxation by wall collisions are surface effects whereas spin exchange collisions and resonant interaction of beam and target gas happen in the gas phase.
The experience after 6 years of operating the target with polarized hydrogen or deuterium gas internal to the HERA storage ring shows, that the interaction of the HERA beam and the storage cell changes both recombination and spin relaxation properties of the cell surface.

4.1 Recombination Processes

The atoms which are injected into the HERMES target storage cell may recombine to molecules. This recombination process can in principle take place either on the storage cell walls (surface recombination) or in the gas phase (volume recombination). At the low gaseous densities of the HERMES target the volume recombination is negligible.
Two types of processes of surface catalysis can be distinguished:

1. the Langmuir-Hinshelwood (L-H) process, where two adsorbed atoms thermalized with the storage cell wall react with each other and

2. the Eley-Rideal (E-R) process, where an atom from the gas phase impinges on an adsorbed surface atom and reacts directly with it [Hol 94]. The impinging atom is not thermalized with the storage cell wall because thermalization takes place on the surface after the adsorption of a particle.

Both reaction types have been investigated in surface science using chemisorbed atoms or molecules on metal surfaces. Evidence for the existence of both (L-H) [Eng 78, Con 78] and (E-R) [Kui 91, Ret 92] type reactions has been found although it took until the early nineties to prove the (E-R) mechanism experimentally. Chemisorbed atoms have a typical binding energy of above 1 eV and they can not evaporate at room temperatures. The experimental preparation of surfaces with a coverage of one or more monolayers of chemisorbed atoms is a standard technique in surface science.
Atoms may also be bound to the surface by a different effect caused by the Van-der-Waals interaction. The binding energies of these so-called physisorbed atoms are between 10 meV and 100 meV. With such a weak binding, physisorbed atoms will evaporate at room temperatures after staying on the wall for less than nanoseconds. Hence physisorbed atoms are difficult to access experimentally.
A Drifilm coating as used on the HERMES storage cell is a surface without chemisorption sites because it is chemically saturated and (in the ideal case) has no unpaired electrons where other atoms could couple to. The surface of a Drifilm coating consists of silicon methyl groups ($CH_3 - Si$). The hydrogen atoms of the Drifilm surface are of course chemically bond so that one can understand a Drifilm coating as a surface with a saturated monolayer of chemisorbed hydrogen with a bond strength of about 415 $\frac{kJ}{mol}$[1]. Measurements at the HERMES target indicated, that these chemisorbed hydrogen atoms may be released from their position by the impinging radicals H_1 or D_1 from the target gas [Bau 00] because the bond strength of a hydrogen molecule at 436 $\frac{kJ}{mol}$ is higher than for the chemical bound of a hydrogen atom to the Drifilm structure. These measurements have been performed with a new storage cell and polarized deuterium atoms as target gas, where it could be seen that the hydrogen atoms of the CH_3-groups recombine with the impinging deuterium radicals and are then slowly replaced by deuterium resulting in CH_2D-groups on the surface. This effect is observable in the measured fraction of the atomic masses 2,3 and 4 (H_2 or D_1, HD and D_2).
Baumgarten was able to distuinguish between in total three different reaction mechanisms: (*i*) An activated E-R process with an activation energy of 31.6 meV (68 meV) in case of hydrogen (deuterium) for temperatures above 120 K. For lower temperatures L-H processes (*ii*) between two physisorbed atoms and (*iii*) between one physisorbed and one chemisorbed atom from the

[1] A bond strength of 415.1 $\frac{kJ}{mol}$ has been calculated for $CH_3Si(CH_3)_3$ which is chemically similar to Drifilm (CH_3SiO_3) [Dan 64]

methyl groups could be seperated. As the first L-H process (*ii*) is density dependent it is not only proportional to the mean sticking time of an atom on the surface but additionally to the average number of visited surface sites. This interpretation is consistent with a measured[2] binding energy of physisorption of about $E_b \simeq 23$ meV and an activation energy for jump diffusion of about $E_j \simeq 8$ meV in case of hydrogen.
It is remarkable that the density dependent process was only identifiable in measurements after a long exposure of the storage cell to the HERA beam. Since the storage cell temperature usually is kept below 140 K, a small amount of water originating from the dissociation in the atomic beam source (compare chapter 3.4) freezes on the surface and grows into an ice layer on top of the Drifilm surface. The bond strength of a water molecule ($\mathrm{H-OH}$) of 498 $\frac{\mathrm{kJ}}{\mathrm{mol}}$ is higher than the $\mathrm{H-H}$ bond strength. The same applies for the case of deuterium, where the bond strength of $\mathrm{D-OD}$ is larger than the one of $\mathrm{D-D}$ bindings. As a result, the second L-H process (*iii*) with chemisorbed atoms is strongly suppressed and the density dependent and weaker first L-H process (*ii*) between two physisorbed atoms becomes dominant.
The growing of the ice layer is affected by the continous irradiation of the storage cell surface by the HERA beam. This irradiation changes the chemical structure on the surface causing the surface to become less hydrophobic. On the other hand, the energy of the impinging synchrotron photons causes the water molecules to desorb again. Thus the time constant for the coverage with ice is determined by the radiation dose interacting with the storage cell and is not limited by the amount of available water in the injected beam.

4.2 Spin Relaxation

Three different spin relaxation mechanisms are observable at the HERMES target causing a change in the hyperfine state population of the target gas inside the storage cell. Analogous to the recombination process, one possible relaxation process takes place on the wall of the storage cell. Another possibility for spin relaxation is given by two-body spin exchange collisions of atoms in the gas phase. Additionally, the high frequency field originated from the HERA beam can cause a depolarization of the target atoms under certain conditions [Kol 98, Kin 91a, Kin 91b, Kin 93]. Spin relaxation of atomic hydrogen by wall or spin exchange collisions with different types of wall coatings has been under study already in the context of hydrogen maser research for low holding fields [Gol 61, Ber 65]. Further studies of the magnetic field dependence of spin relaxation for the HERMES targets [Bra 95] as well as studies of the temperature dependence [Pri 93, Pri 94, Kol 98], of the density dependence and an analysis of the transition spectra

[2] The energy values have been derived by applying spin relaxation measurements at the HERMES target to a temperature dependent relaxation model [Bau 00].

[Bau 00] followed. Measurements of spin relaxation of other atomic species on Drifilm surfaces have also been performed on sodium [Lev 88, Swe 88], rubidium [Cam 87] and alkalis [Ste 94].

4.2.1 Wall Relaxation

The atoms injected by the atomic beam source (ABS) experience a certain number of wall collisions during their diffusion process through the storage cell. An attractive Van-der-Waals potential between the storage cell wall and the diffusing atom causes the atom to be physisorbed, i.e. staying for a certain time close to the surface until its energy following the Boltzmann distribution is large enough to be desorbed again. The mean occupation time on the wall τ_s is described by an Arrhenius equation:

$$\tau_s = \tau_0 \cdot e^{\left(\frac{E_b}{kT}\right)} \ , \tag{4.1}$$

where τ_0 is the high temperature limit of τ_s, E_b is the adsorption energy (or binding energy) and kT equals the thermal energy of the atom. For the HERMES storage cell the mean occupation time is of the order of $\tau_s \approx 10^{-10}$ s. Depending on the surface type and temperature as well as on the external magnetic field one can give a probability that the atom leaves the wall in a certain hyperfine state. This is described by means of a transition probability matrix $W_{\mathrm{b}\to\mathrm{a}}$, which represents the probability to find an atom in state $|\, a\,\rangle$ that has been in state $|\, b\,\rangle$ prior to the wall collision.

During the time an adsorbed atom stays on the wall, the magnetic moment of its unpaired electron interacts with magnetic moments on the surface by means of dipolar coupling and with other unpaired electrons by means of exchange interaction. The adsorbed atom diffuses on the surface and experiences various interaction strengths from site to site. Bouchiat and Brossel concluded from their measurements of the relaxation strength with different cell coatings [Bou 63a, Bou 63b, Bou 65] that the major part of the spin relaxation is caused by dipole-dipole interaction with the nuclear dipoles of the coating.

The other main contribution to spin relaxation results, if unpaired electron spins are present on the surface. Due to the Pauli principle an energy difference might exist for parallel and antiparallel spins, which is called the exchange energy [And 63].

The theoretical description and calculation of the transition probability matrix for the HERMES target can be found in [Bau 00].

In a strong magnetic field the nuclear spins are mostly decoupled from the electron spins as explained in chapter 2.1. As all relaxation processes couple to the electron spin, the resulting relaxation of the nucleons is by far lower than of the electrons. This can be expressed using the relaxation probabilities γ_z of the nuclear spin and γ_e of the electron spin with a usual ratio of

$$\frac{\gamma_e}{\gamma_z} \simeq 50 \tag{4.2}$$

at cell temperatures of $T_{\text{cell}} \simeq 100$ K.

4.2.2 Spin Exchange Relaxation

This interaction in the gas phase causes two colliding atoms to undergo spin exchange during their collision, where the hyperfine states can be changed via an interaction of the electron spins. First theoretical descriptions of spin exchange collisions have been made by Purcell and Fields [Pur 56] for interstellar gas collisions. To calculate the cross section σ_{se} for spin exchange collisions, they used the phase shift difference

$$\Phi = \int_0^\infty \frac{V_t - V_s}{\hbar}\,\mathrm{d}t \tag{4.3}$$

of the molecular singlet (V_s) and triplet (V_t) interaction potential. The spin exchange cross section is then given by

$$\sigma_{se} = 2\pi \int_0^\infty \sin^2\left(\frac{\Phi}{2}\right) \cdot b\,\mathrm{d}b \tag{4.4}$$

where b is the impact parameter. As for the integrated phase $\Phi \gg 2\pi$ holds, the spin state of the electron after the collision follows a statistical distribution. Thus the spin exchange probability is $\frac{1}{2}$. In this description also collisions are taken into account after which the hyperfine population is unchanged. Equation (4.4) is a straight line approximation to the deflection of the atoms by the scattering process [Dal 65, Mas 34, Swe 85]. The complete description is given by a partial wave analysis [Wit 56], summing over all partial waves with an angular momentum l

$$\sigma_{se} = \frac{\pi}{k^2} \sum_{l=0}^{\infty} (2l+1) \sin^2\left(\phi_l^s - \phi_l^t\right) , \tag{4.5}$$

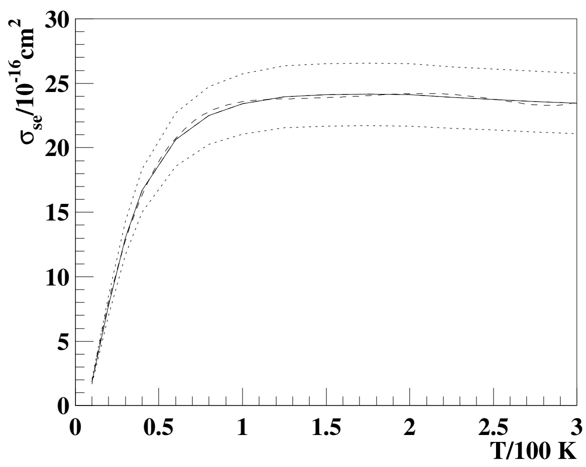

Figure 4.1: The spin exchange cross section $\sigma_{se} = \frac{\sigma_+ + \sigma_-}{2}$ versus temperature (solid line) as calculated by Allison [All 72]. The dotted curves indicate the quoted systematical uncertainty of 10%. The dashed line is a fit with a polynomial of 5th order in $\frac{T}{100\ \mathrm{K}}$. Measurements gave a good agreement with this calculation [Des 76].

$\sum_i m_F$	Hydrogen	Deuterium
3		$\|11\rangle$
2	$\|11\rangle$	$\|12\rangle\,\|16\rangle$
1	$\|12\rangle\,\|14\rangle$	$\|13\rangle\,\|15\rangle\,\|22\rangle\,\|26\rangle\,\|66\rangle$
0	$\|13\rangle\,\|22\rangle\,\|24\rangle\,\|44\rangle$	$\|14\rangle\,\|23\rangle\,\|25\rangle\,\|36\rangle\,\|56\rangle$
-1	$\|23\rangle\,\|34\rangle$	$\|24\rangle\,\|33\rangle\,\|35\rangle\,\|46\rangle\,\|55\rangle$
-2	$\|33\rangle$	$\|34\rangle\,\|45\rangle$
-3		$\|44\rangle$

Table 4.1: Pairs of hyperfine states of hydrogen and deuterium for which spin exchange collisions are allowed by angular momentum conservation. A spin exchange collision is only possible within the same group, so that for example $|\,11\,\rangle$ can never relax by means of spin exchange collisions.

where $k = \mu v/h$ is the wave constant [Kni 88] and $\phi_l^{s,t}$ are the phase shifts for the singlet and triplet potentials. A measurement of σ_{se} [Des 76] resulted a nearly constant value of $\sigma_{se} = 2.31(28) \cdot 10^{-15}\,\mathrm{cm}^2$ in a temperature range between 77 and 363 K, which is in good agreement with calculations done by Allison [All 72] as seen in figure 4.1.

The effect of spin exchange collisions on the hyperfine population is given by a tensor M^i_{jk}, which describes the probability to find an atom in state $|\,i\,\rangle$ after a collision of two atoms in the states $|\,j\,\rangle$ and $|\,k\,\rangle$ prior to the collision [Wal 93]:

$$\frac{\mathrm{d}N_i}{\mathrm{d}t} \propto \sum_{j,k} M^i_{jk}\, N_j\, N_k \ . \tag{4.6}$$

Due to the conservation of angular momentum the sum of the magnetic quantum numbers m_F of the total angular momentum before and after the spin exchange collision has to be the same:

$$\Delta \sum_i m_F = 0 \ . \tag{4.7}$$

This results in the effect, that pairs of hyperfine states form groups which can not be left by means of spin exchange collisions, i.e. any initial configuration $|\,ij\,\rangle$ must result a final configuration $|\,kl\,\rangle$ of the same group. The possible groups are listed in table 4.1. One can immediately see that if an initial population of the gas consists only of one pure state ($|\,1\,\rangle$ or $|\,3\,\rangle$ in case of hydrogen and $|\,1\,\rangle$ or $|\,4\,\rangle$ in case of deuterium) no relaxation by means of spin exchange collisions is possible.

Another interesting result of the angular momentum conservation in spin exchange collisions is the polarization transfer between nucleons and electrons. It can be used to polarize nucleons in laser driven sources (LDS). For this purpose hydrogen or deuterium atoms are polarized by spin exchange collisions with optically pumped potassium [Cou 92, Stn 95].

4.2.3 Bunch Field Induced Depolarization

The beam current of the HERA electron/positron storage ring is strongly bunched to provide a maximal luminosity for the collider experiments H1 and ZEUS. The time between two adjacent bunches is $\tau_{\rm bunch} = 96.06$ ns. Typically most of the 220 RF buckets are filled, so that the frequency is given by $\nu_{\rm bunch} = \frac{1}{\tau_{\rm bunch}} = 10.41$ MHz. A large number of harmonics contributes to the induced magnetic high frequency field close to the HERA beam, because the bunches are very short. If the transition frequency between two hyperfine states $|\,i\,\rangle$ and $|\,j\,\rangle$ given by $\nu_{ij} = \frac{|E_i(B)-E_j(B)|}{h}$ at a certain magnetic holding field B (compare chapter 2.1) matches one or several of these harmonics, resonant depolarization occurs. Measurements of bunch field induced depolarization at the HERMES target have been presented in case of hydrogen [Kol 98, HER 98b] and deuterium respectively [Bau 00]. Following these measurements the value of the magnetic holding field has been chosen such that no transition frequencies match the beam harmonics. In the following, it is assumed that no bunch field induced transitions may occur in the HERMES storage cell.

4.3 Master Equation for Coaction of Spin Relaxation Processes

The spin relaxation processes inducing a change in the hyperfine population of the gas inside the storage cell can be described by a so-called *master equation* [Bra 95, Stn 95, Bau 00]. The time dependence of the hyperfine state $|\,i\,\rangle$ is hence given by

$$\frac{\mathrm{d}N_i}{\mathrm{d}t} = \frac{1}{\tau_d}\left((N_i^{\rm inj} - N_i) + \frac{\tau_d}{\tau_f}\sum_k R_{jk}N_k + \frac{\tau_d}{\tau_{se}}\sum_{jk} M^i_{jk}N_jN_k \right) \ . \tag{4.8}$$

In this equation three time constants appear: τ_d (the diffusion time) is the mean occupation time of the atoms within the storage cell, τ_f is the mean time of flight between to wall collisions and τ_{se} is the mean time between two spin exchange collisions. The first part of equation (4.8) represents the incoming and outgoing flux, the third term wall relaxation and the last term spin exchange relaxation.

Following the formulation of Abragam [Abr 61] and using the transition probabilities $W_{\rm k\to j}$, the change in the hyperfine population N_i is proportional to the amount of atoms flipping into state $|\,i\,\rangle$ minus the amount of atoms leaving state $|\,i\,\rangle$:

$$\frac{\mathrm{d}N_i}{\mathrm{d}t} \propto \sum_j W_{\rm j\to i}N_j - N_i\sum_j W_{\rm j\to i} = \sum_j \left[W_{\rm j\to i} - \left(\sum_k W_{\rm k\to i}\right)\delta_{ij} \right] N_j \ , \tag{4.9}$$

with the Kronecker symbol δ_{ij}. The wall relaxation matrix R_{jk} can then be described by

$$R_{jk} = W_{\rm k\to j} - \delta_{jk}\sum_l W_{\rm l\to j} \ . \tag{4.10}$$

$\|q\rangle$	m_q	$q_\uparrow$	$q_\downarrow$
$\|1\rangle$	$+\frac{3}{2}$	1	0
$\|2\rangle$	$+\frac{1}{2}$	$\cos\theta_+$	$\sin\theta_+$
$\|3\rangle$	$-\frac{1}{2}$	$\cos\theta_-$	$\sin\theta_-$
$\|4\rangle$	$-\frac{3}{2}$	0	1
$\|5\rangle$	$-\frac{1}{2}$	$-\sin\theta_-$	$\cos\theta_-$
$\|6\rangle$	$+\frac{1}{2}$	$-\sin\theta_+$	$\cos\theta_+$

$\|q\rangle$	m_q	$q_\uparrow$	$q_\downarrow$
$\|1\rangle$	+1	1	0
$\|2\rangle$	0	$\cos\theta$	$\sin\theta$
$\|3\rangle$	-1	0	1
$\|4\rangle$	0	$-\sin\theta$	$\cos\theta$

Table 4.2: Coefficients m_q, $q_\uparrow$ and $q_\downarrow$ for any hyperfine state $|\,q\,\rangle$ of the spin exchange tensor M^i_{jk} for deuterium (left) and hydrogen (right).

The spin exchange relaxation tensor M^i_{jk} can be calculated following the description in [Wal 93] after introducing the notation

$$|\,q\,\rangle = q_\uparrow \left|\uparrow, m_q - \frac{1}{2}\right\rangle + q_\downarrow \left|\downarrow, m_q + \frac{1}{2}\right\rangle \tag{4.11}$$

for any hyperfine state $|\,q\,\rangle$ with $m_q = \langle\,q\,|\,F_z\,|\,q\,\rangle$ and the coefficients $q_{\uparrow,\downarrow}$ as given in table 4.2. The calculation is then done by:

$$\begin{aligned} M^i_{jk} = \sum_l \; & -2\,\langle\,i\,|\,j\,\rangle\,\langle\,l\,|\,k\,\rangle\,(i_\uparrow j_\uparrow k_\downarrow l_\downarrow + i_\downarrow j_\downarrow k_\uparrow l_\uparrow) \\ & +\langle\,m_i\,|\,m_j\,\rangle\,\langle\,m_l\,|\,m_k\,\rangle\,(i_\uparrow j_\uparrow k_\downarrow l_\downarrow + i_\downarrow j_\downarrow k_\uparrow l_\uparrow)^2 \\ & +\langle\,m_i\,|\,m_j-1\,\rangle\,\langle\,m_l\,|\,m_k+1\,\rangle\,(i_\downarrow j_\uparrow k_\downarrow l_\uparrow)^2 \\ & +\langle\,m_i\,|\,m_j+1\,\rangle\,\langle\,m_l\,|\,m_k-1\,\rangle\,(i_\uparrow j_\downarrow k_\uparrow l_\downarrow)^2 \;. \end{aligned} \tag{4.12}$$

For times that are large compared to τ_d, the hyperfine population converges towards a dynamical equilibrium (*steady state*). The steady state population is of practical interest, because the Breit-Rabi polarimeter (BRP) requires a stable hyperfine state population for a polarization measurement, which takes a multiple of τ_d. The solution of the nonlinear algebraic equation system of equation (4.8) in the steady state $\left(\frac{\mathrm{d}N_i}{\mathrm{d}t} = 0\right)$ can be solved directly in case of hydrogen or with the help of a numerical iteration algorithm in case of deuterium [Bau 00].

4.3.1 Time Resolved Polarization Measurements

In order to show that the master equation (4.8) is suitable to describe the behaviour of the target gas in the storage cell, polarization measurements have been carried out with a time resolution of 25 μs. These measurements yield the time dependence of the hyperfine state population as seen by the BRP which is then compared to the prediction from the master equation. The time constants τ_d, τ_f and τ_{se} are the parameters of the fit of the master equation to the measured data.

For this purpose the beam modulation technique used for the time of flight measurements explained in chapter 3.6.3 can be applied to the WFT in the appendix of the ABS. In this way the injected hyperfine state population can be switched roughly ten times per second. In parallel, a SFT 3-5 transition between the sextupole magnets of the ABS is operated permanently. Thus the injection mode changes from states $|\,1\,\rangle + |\,2\,\rangle$ (with WFT 1-4/2-3 off) to states $|\,3\,\rangle + |\,4\,\rangle$ (with WFT 1-4/2-3 on). If the transmissions of the sextupole magnets and the transition efficiencies are assumed to equal unity, this may be represented as

$$\begin{pmatrix}1\\1\\1\\1\\1\\1\end{pmatrix} \overset{\text{sixpole}}{\Longrightarrow} \begin{pmatrix}1\\1\\1\\0\\0\\0\end{pmatrix} \overset{\text{SFT 3-5}}{\Longrightarrow} \begin{pmatrix}1\\1\\0\\0\\1\\0\end{pmatrix} \overset{\text{sixpole}}{\Longrightarrow} \begin{pmatrix}1\\1\\0\\0\\0\\0\end{pmatrix} \overset{\text{WFT 1-4/2-3}}{\Longrightarrow} \begin{pmatrix}0\\0\\1\\1\\0\\0\end{pmatrix} . \tag{4.13}$$

With the knowledge of sextupole transmissions and transition efficiencies (values for both are given in chapter 6.1) the injected hyperfine state population can be calculated correctly. Between the flipping of injected states, the hyperfine state population of the target gas has enough time to stablize as the time between two flips (100 ms) is large compared to τ_d (5 ms).

The time dependent changes of the hyperfine state population are measured by performing a polarization analysis of in total ten different spectra from the time resolving counter of the BRP, one for each BRP state of a polarization measurement (see table 3.4). After that the data is rebinned so that the time distance between two points is about 0.5 ms.

The measurements have been performed at a cell temperature of $T_{\text{cell}} \simeq 89$ K and the extracted hyperfine state behaviour can be seen in figure 4.2. The trigger pulse of the WFT switching on is at $t = 0$. It takes about 1.1 ms until the change of the injection mode can be recognized by the BRP, i.e. the time of flight between ABS WFT and storage cell plus the time of flight between storage cell and BRP detector. At a nozzle temperature of 100 K the velocity with optimal transmission through the ABS sextupole magnet system for deuterium is about 1500 $\frac{\text{m}}{\text{s}}$ [Loz 93]. The distance between storage cell and BRP detector is 140 cm and the distance between ABS WFT and storage cell is 20 cm. The total path of 165 cm requires a time of flight of 1.06 ms at the given velocity which agrees nicely with the 1.1 ms one derives from the measurements.

After this *detector drift time* of 1.1 ms the master equation is fitted to the measurements for each individual hyperfine state. This fit is represented by the solid line in the figures. It is obvious from the upper figure that at the time the states $|\,1\,\rangle$ and $|\,4\,\rangle$ reach an equal population ($N_1 \simeq N_4$), N_6 reaches its maximum. This is explained within the relaxation model as the change in N_6 depends on the product $N_1 \cdot N_4$ which is maximal in the crossing point of both population numbers. This point is reached 4.1 ms after the injected population $\vec{N}^{\text{inj}}$ into the storage cell changes. With the same reasoning N_5 reaches a maximum at $N_2 \simeq N_3$ after 3.4 ms

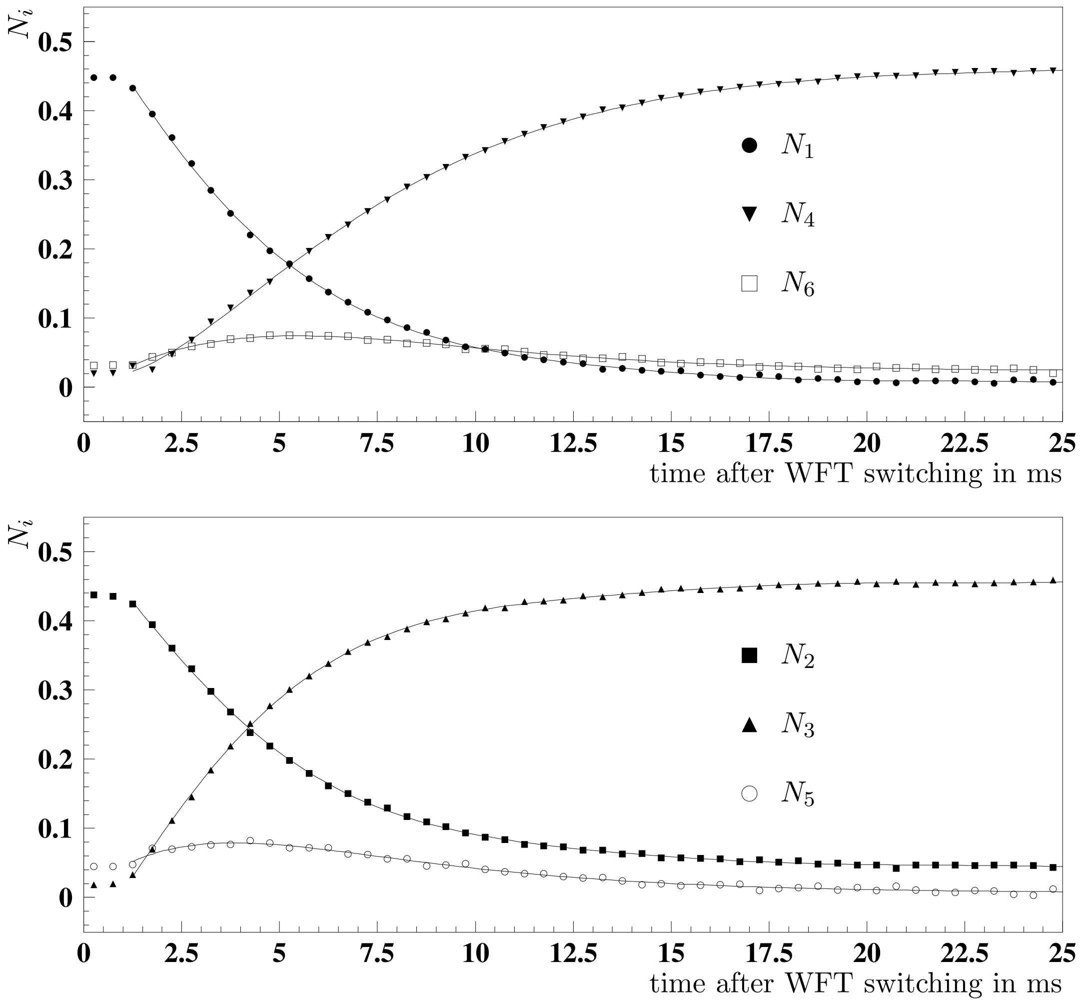

Figure 4.2: Time dependence of the hyperfine state behaviour inside the storage cell after switching the injection from states $|\,1\,\rangle + |\,2\,\rangle$ to states $|\,3\,\rangle + |\,4\,\rangle$. The symbols refer to measured population numbers, the solid line represents the behaviour predicted by the master equation.

as seen in the lower figure.

The fitted parameters of equation (4.8) are the time constants τ_d, τ_f and τ_{se}:

$$\begin{aligned} \tau_d &= 4.45 \pm 0.01 \text{ ms} \\ \tau_f &= 10.31 \pm 0.21\ \mu\text{s} \\ \tau_{se} &= 1.48 \pm 0.09 \text{ ms} \end{aligned} \tag{4.14}$$

At a cell temperature of 89 K, the diffusion time of $\tau_d = 4.45$ ms is equivalent to an average trajectory length of roughly 432 cm before an atom leaves the storage cell geometry. The value

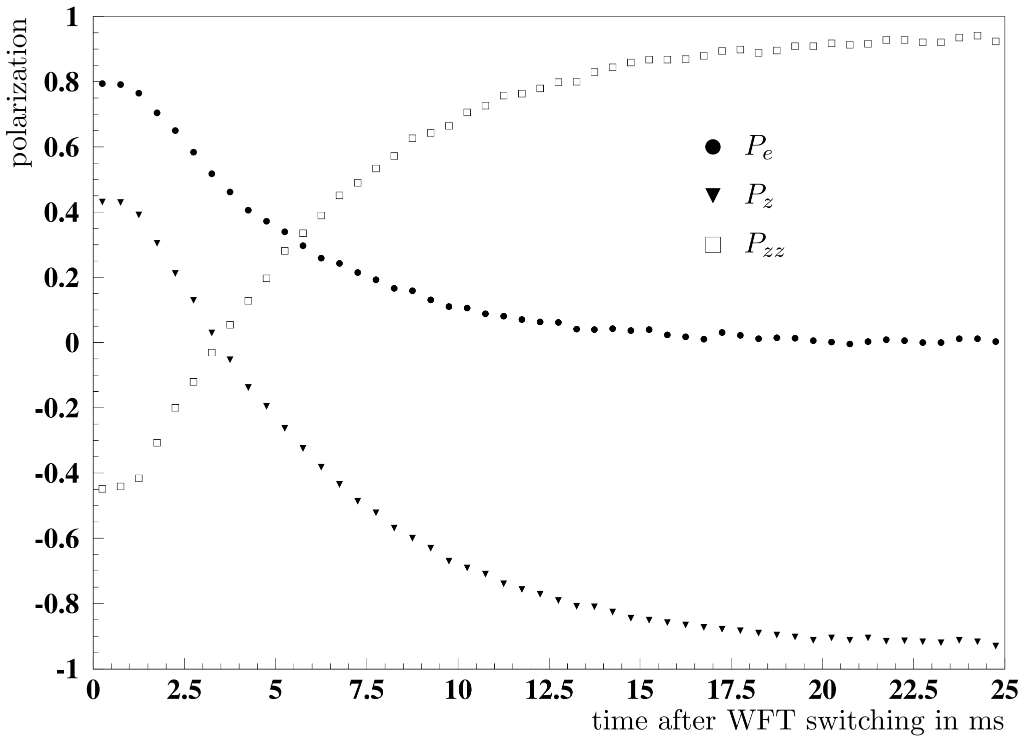

Figure 4.3: Time dependence of the polarization behaviour inside the storage cell after switching the injection from states $|\,1\,\rangle + |\,2\,\rangle$ to states $|\,3\,\rangle + |\,4\,\rangle$. The data points are calculated from the rebinned hyperfine state population numbers shown in figure 4.2.

resulting from a molecular flow simulation is 431 cm. As $\tau_s \ll \tau_f$, the average number of wall collision $\langle\, c\,\rangle$ can be calculated from (4.14) by

$$\langle\, c\,\rangle = \frac{\tau_d}{\tau_f} = 431.6 \pm 8.8 \tag{4.15}$$

which also meets the expectations from the simulation of $\langle\, c\,\rangle \simeq 429$.
The time dependent behaviour of the polarizations P_e, P_z and P_{zz} can be seen in figure 4.3. They are calculated from the corresponding hyperfine state populations in figure 4.2. One can see, that about 20 ms after a new injection mode of the ABS is selected, the polarizations reached the dynamical equilibrium (steady state). During this time, the target status is marked 'undefined' for the HERMES analysis. In former times, the duration of this 'undefined' target status had to be conservatively estimated and was roughly 600 – 800 ms.

Chapter 5

Sampling Corrections

In chapter 1.4 the necessity of sampling corrections to correlate the measured quantities of atomic polarization (by the BRP) and atomic fraction (by the TGA) as analyzed from a sample of the target gas originating from the center of the storage cell to the average values along the storage cell as seen by the HERA beam has already been mentioned. These sampling correction functions $c_\alpha(\alpha_r^{\mathrm{TGA}})$ and $c_p(P_a^{\mathrm{BRP}})$ depend strongly on the distribution of recombination and wall relaxation probablities per wall collision along the storage cell. This becomes evident if one compares the histories of a particle entering the TGA and another particle still inside the storage cell: They both experience a different amount of wall collisions at different places of the storage cell geometry. This comparison is of special interest because the difference in these particles history directly leads to the sampling correction c_α.

If the storage cell is not yet exposed to the HERA beam, one can assume that the recombination and wall relaxation probabilities per wall collision are constant over the entire surface of the storage cell, or at least that microscopic inhomogeneities by different types of surface sites are equally distributed. Under normal operation no influence of the HERA beam on the target performance has been observed. Nevertheless certain limited periods of impact on the cell have been found, when the beam tuning was non-optimal or the HERA beam was accidentally lost near the HERMES target region. During such occasions especially the values of α_r^{TGA} and P_e were affected. Another experimental finding is that during injection the storage cell temperature increases and P_e decreases due to bunch field depolarization [Kol 98].

During the periods when α_r^{TGA} and P_e have been affected, increased synchrotron and/or charged rates have been measured by the HERMES hodoscopes and the vacuum pressure increases, which indicates an unusual rise of the heat load at certain points of the beam pipe. Possible mechanisms how the HERA beam could affect the surface properties of the storage cell might be:

- desorption of the surface coating by synchrotron radiation,

- bombardment of the storage cell walls with charged particles,
- chemical reactions of ionized hydrogen or deuterium radicals with the cell surface,
- removal of the ice layer on the storage cell wall by radio frequency heating due to the wake fields or
- contamination of the storage cell surface by sputtered material from collimator C2.

Since the exact effect of the HERA beam on the surface properties is unknown, any possible distribution of recombination and wall relaxation probabilities has to be considered for a limitation of the possible sampling corrections.

5.1 Molecular Flow Simulations

With gas densities inside the storage cell of between 10^{12} and 10^{13} atoms/cm^3 the mean free path of an atom is of the order of several meters which is large compared to the mean path between two wall collisions inside the storage cell, which is of the order of centimeters. Thus atom-atom collisions in the volume can be neglected and the behaviour of the target gas can be described by molecular flow [Knu 09]. It is assumed that both atoms and molecules are physically adsorbed on the surface for a short time period whenever they collide with a wall. During this time the atoms thermalize with the surface until they evaporate back into the gas phase. As adsorption and desorption are decoupled processes, the desorption can be assumed to be isotropic and thus to be described by a $\cos\theta$-distribution, where θ is the desorption angle relative to the surface normal [Knu 15, Com 85]:

$$\frac{\mathrm{d}\sigma}{\mathrm{d}\Omega} \propto \cos\theta \ . \tag{5.1}$$

Integrating over the azimuth angle ϕ, which is equally distributed between 0 and 2π results in a probability distribution for the desorption angle θ of

$$\frac{\mathrm{d}\sigma}{\mathrm{d}\theta} \propto \sin 2\theta \ . \tag{5.2}$$

To determine the history of particles travelling through the target storage cell Monte-Carlo simulations have been developed. In such a simulation the path of a target gas atom through the cell is calculated using the above mentioned desorption angle distribution after each wall collision within a certain geometry. The geometry of the storage cell is implemented by a combination of surfaces of simple bodies, i.e. tubes with circular or elliptic cross section, balls, cylinders, plains, cones and tori.

By recording the history of these particles, information about how often the particles collide with which part of the cell walls becomes available [Hen 98]. This information is stored in so-called *local particle history files* (LPH-files) $C_k^i(z)$. A wall collision is randomly chosen and all collision ages C_k of the colliding particle on distinguishable surface types k are written into one file for each of these surface sections, now indicated by z. The counting variable i denotes the different particles, whose history has been written to file. The amount of different surface types k is in principle unlimited. For the simulations of the HERMES storage cell in total $k = 32$ surfaces have been distinguished with 28 bins of 2 cm width in the beam tube and 4 different surfaces for all side tubes[1].

With this simulated data any scenario of the distribution of recombination and wall depolarization probabilities along the storage cell can be analyzed. If $(1 - p_{wd})$ is the polarization loss by wall collisions, p_{wd} can be calculated based on the local particle history for each of the cell sections z by:

$$p_{wd}(z) = \frac{1}{n} \cdot \sum_{i=1}^{n} \prod_{k=1}^{32} (1 - \gamma_p^{(k)})^{C_k^i(z)} \ , \tag{5.3}$$

with a total number of entries n per file, the polarization loss from spin exchange collisions $(1-p_{se})$ and the injected polarization P^{inj}. $\gamma_p^{(k)}$ denotes the spin relaxation probability per wall collision on the surface k. The calculation of the atomic fraction in these cell sections can be carried out analogous, where only the depolarization probabilities are replaced by recombination probabilities $\gamma_r^{(k)}$:

$$n_a(z) = \frac{1}{n} \cdot \sum_{i=1}^{n} \prod_{k=1}^{32} (1 - \gamma_r^{(k)})^{C_k^i(z)} \ . \tag{5.4}$$

For average values along the storage cell, the first 28 bins (representing cell surfaces within the beam tube) have to be weighted with the normalized atomic density $\rho(z)$, e.g.

$$n_a = \sum_{z=1}^{28} \rho(z) \cdot n_a(z) \ , \tag{5.5}$$

and for p_{wd} correspondingly. The atomic density can also be calculated based on the results of the simulation by

$$\rho(z) = \rho_k = \frac{\sum_{i,z} C_k^i(z)}{\sum_{i,k,z} C_k^i(z)} \ . \tag{5.6}$$

The values at the place of the detectors are the corresponding z-bin of the distributions p_{wd}(BRP) and $n_a(\text{TGA}) = \alpha_r^{\text{TGA}}$. The average value along the storage cell for p_{wd} following equation (5.5) is given by:

$$p_{wd} = \sum_{z=1}^{28} \rho(z) \cdot p_{wd}(z) \ , \tag{5.7}$$

[1]The three side tubes are described by one parameter each plus one for the *intermediate plane* at the passage from the sample tube to the extension tube.

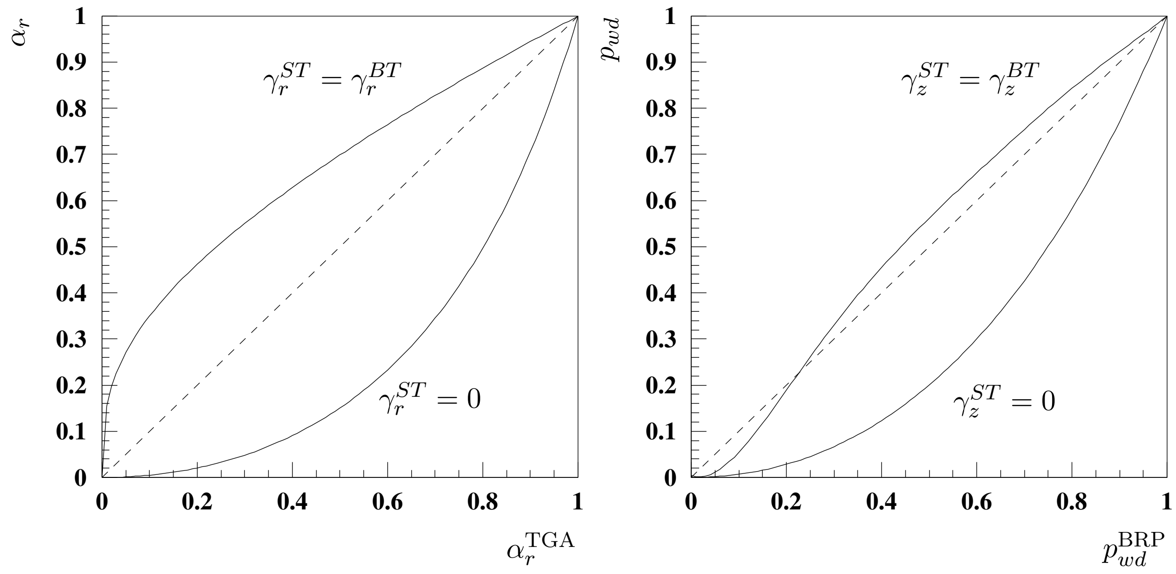

Figure 5.1: Ranges of possible correlations functions between the value at the place of the detector and its corresponding average value along the storage cell. The left picture shows the range in case of recombination, the right picture shows the range in case of wall depolarization. Acceptable uncertainties of α_r and p_{wd} can only be achieved with α_r^{TGA} and p_{wd}^{BRP} being close to unity. The uncertainty grows with increasing recombination/depolarization.

whereas for the average α_r the amount of molecules $n_m = 1 - n_a$ needs to be taken into account as they have less thermal velocity and thus stay longer inside the storage cell, so that

$$\alpha_r = \frac{n_a}{n_a + \sqrt{2} \cdot n_m} = \frac{n_a}{\sqrt{2} + (1 - \sqrt{2}) \cdot n_a} \ . \tag{5.8}$$

By looking at the results for all physically meaningful scenarios (i.e. all reasonable combinations of surface parameters) one finds a range of possible correlation functions between the value at the place of the detector and the average value along the storage cell as seen by the HERA positron beam. For the two detectors (TGA and BRP) this results in two ranges as seen in figure 5.1 correlating α_r and α_r^{TGA} or p_{wd} and p_{wd}^{BRP} respectively. As this correlation for spin exchange relaxation is very close to the diagonal ($c_p^{se} \simeq 1$) [Bau 00], the sampling correction c_p is defined by wall depolarization only. The resulting uncertainty becomes very large if α_r^{TGA} or p_{wd}^{BRP} deviate significantly from unity.

Hence the ranges from figure 5.1 give physically meaningful limits for the sampling correction functions c_α and c_p. The most extreme scenarios have been chosen such that the lower limit is given by non-recombining/depolarizing side tubes and a beam tube that recombines/depolarizes least in the cell center and stronger towards its ends, whereas the upper limit is given by the

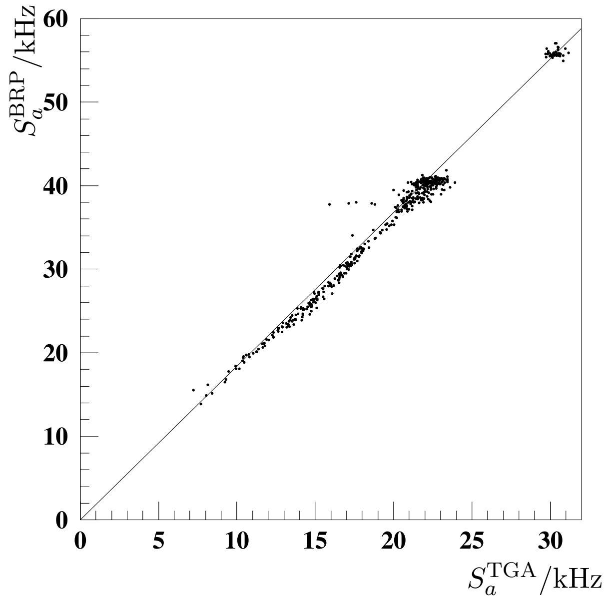

Figure 5.2: Atomic beam signals of BRP and TGA during the recovery period after an accidental HERA beam loss. The proportionality of both signals indicate a constant recombination probability for wall collisions inside the sample and extension tube. The storage cell temperature was constant around $T_{\mathrm{cell}} \simeq 100$ K.

completely homogeneous case of equal recombination/depolarization strength everywhere inside the storage cell. Theoretically one can think of a sampling correction even above the given upper limit, i.e. if all recombination/depolarization occurs on the walls of the sample or extension tube. Measurements after an accidental loss of the HERA beam prove that this scenario can be excluded.

As described in chapter 3.5.1 such a beam loss can cause a very sudden drop of the atomic fraction. α^{TGA} typically recovered slowly within several ten hours. The measured atomic beam intensities of the BRP and the TGA during this recovery period are plotted in figure 5.2. The proportionality of both signals indicates that the recombination probability per wall collision in the sample and extension tube γ_r^{ST} is constant during the complete recovery period as the particles entering the TGA have experienced more than twice the amount of wall collisions in the sample and extension tube than those entering the BRP. Hence if the recombination parameter of the corresponding surfaces would change, the two signals would not be proportional.

This leads to the fact that a beam loss changes the surface properties of the beam tube only while the sample and extension tube are not affected. Assuming that the quality of the surface is homogenously distributed if a cell was not yet exposed to the HERA beam, the recombination strength in the side tubes can only be less than or equal to the recombination strength inside the beam tube:

$$\gamma_r^{ST} \leq \gamma_r^{BT} \ . \tag{5.9}$$

Since it is basically unknown which correlation function (and thus which sampling correction) within the given range is correct, the complete range has to be considered. To apply the sampling correction, the average of the two limits is used with the systematic uncertainty of the half difference of these limits. This method of error estimation is very conservative.

During the data taking periods at the HERMES experiment both α_r^{TGA} and p_{wd} have always been well above 0.9, where linear approximations for the sampling corrections might be used, which are given by

$$c_\alpha = 1.68 - \frac{0.68}{\alpha_r^{\mathrm{TGA}}} \pm \left(-1.13 + \frac{1.13}{\alpha_r^{\mathrm{TGA}}}\right) \quad \text{and} \tag{5.10}$$

$$c_p = 1.46 - \frac{0.46}{p_{wd}} \pm \left(-0.68 + \frac{0.68}{p_{wd}}\right) \ , \tag{5.11}$$

where p_{wd} can be calculated correcting the measured value P^{BRP} for the polarization loss caused by spin exchange relaxation and for the initial polarization as injected by the atomic beam source:

$$p_{wd} = \frac{P^{\mathrm{BRP}}}{p_{se} \cdot P^{\mathrm{inj}}} \ . \tag{5.12}$$

The sampling corrections (5.10) and (5.11) have been calculated for the large storage cell of 29.8×9.8 mm elliptical cross section of the beam tube. Similar calculations can be done for the smaller cell with a cross section of 21.0×8.9 mm, which was installed in December 1999. Additionally, the diameter of the sample tube has been increased from 5 mm to 6 mm.
In the case of a smaller beam tube cross section and a larger sample tube cross section, the two limits from figure 5.1 move further away from each other. This increases the uncertainty with the presence of a significant amount of recombination or depolarization. Furthermore the sampling correction and thus the average value along the storage cell at a given measured value by the analyzers are reduced. The corresponding results for the sampling corrections are then given by

$$c_\alpha = 1.83 - \frac{0.83}{\alpha_r^{\mathrm{TGA}}} \pm \left(-1.27 + \frac{1.27}{\alpha_r^{\mathrm{TGA}}}\right) \quad \text{and} \tag{5.13}$$

$$c_p = 1.55 - \frac{0.55}{p_{wd}} \pm \left(-0.77 + \frac{0.77}{p_{wd}}\right) \ . \tag{5.14}$$

5.2 The Diffusion Equation

Instead of deducing the sampling corrections from the molecular flow simulation, they can also be calculated analytically by describing the diffusion process of the target gas inside the storage cell with the help of the one-dimensional diffusion equation [Bau 02a]

$$\frac{\partial \rho}{\partial t} = D \frac{\partial^2 \rho}{\partial z^2} + q \ , \tag{5.15}$$

where ρ is the particle density and D the diffusion constant [Fic 55]. The source density q can be used to describe the (non-diffusive) appearance or disappearance of atoms, which are either ballistically injected by the ABS or recombine on the cell walls. Equation (5.15) is derived from the continuity equation for tubes of constant cross section and temperature.

The injection of the ABS can be modeled by a steady delta-like source at $z = 0$, i.e. the cell center. Thus the density is constant in time, leading to

$$D\frac{\partial^2 \rho}{\partial z^2} = -\frac{\dot{\rho}_{\rm inj}}{S}\delta(z) \ , \tag{5.16}$$

where $\dot{\rho}_{\rm inj}$ represents the constant number of injected atoms per unit time and S stands for the cross-section of the beam tube. With the approximation of vanishing densities at the ends, this equation can be solved by a triangular density profile

$$\begin{aligned} \rho(z) &= \rho_0(1 - \tfrac{|z|}{L}) \quad \text{for} \quad |z| < L \\ \rho(z) &= 0 \qquad\qquad\quad \text{for} \quad |z| \geq L \quad , \end{aligned} \tag{5.17}$$

where $2L$ is the length of the beam tube and $\rho_0 = \rho(0)$ is the central density. This triangular density profile agrees well with the results for $\rho(z)$ from the molecular flow simulation.
If recombination and relaxation in the sample and extension tube can be neglected, the properties of the gas in the storage cell center are identical to the properties of the gas diffusing out the sample tube. Following the description in [Bau 02a] the average normalized atomic density in the presence of recombination may be limited by

$$\rho_a(0,\gamma_r) \geq \bar{\rho}_a(\gamma_r) \geq \frac{\rho_a^2(0,\gamma_r)}{1+\eta(1-\rho_a(0,\gamma_r))} \ , \tag{5.18}$$

where η is the ratio of conductances of the side tubes ($C^{\rm IT}$ - injection tube and $C^{\rm ST}$ - sample tube) relative to the beam tube ($C^{\rm BT}$):

$$\eta = \frac{C^{\rm IT} + C^{\rm ST}}{2 \cdot C^{\rm BT}} \ . \tag{5.19}$$

The factor 2 originates from the fact that $C^{\rm BT}$ is defined as the conductance of one wing of the beam tube only, which is half of its total value. This definition has been chosen for symmetry reasons in the calculations.
The atomic fraction α can be expressed by the normalized atomic density using

$$\alpha(z,\gamma_r) = \frac{\rho_a}{\rho_t} = \frac{\rho_a}{\sqrt{2} - (\sqrt{2}-1)\rho_a} \ , \tag{5.20}$$

with the total normalized target density ρ_t. Making use of equation (5.18) one can now determine also limits for the density weighted average value of α from a known value $\rho_a(0)$ by

$$\frac{\sqrt{2}\ \rho_a(0)}{1+(\sqrt{2}-1)\rho_a(0)} \geq \alpha \geq \frac{\rho_a^2(0)}{\sqrt{2}[1+\eta(1-\rho_a(0))] - (\sqrt{2}-1)\rho_a^2(0)} \ , \tag{5.21}$$

with a relative systematic uncertainty again calculated by

$$\frac{\Delta\alpha}{\alpha} = \frac{\alpha_{\max} - \alpha_{\min}}{\alpha_{\max} + \alpha_{\min}} \ . \tag{5.22}$$

Similar to figure 5.1 the uncertainty becomes large if α deviates significantly from unity. In such a case stronger restrictions on the possible distribution of recombination and wall relaxation parameters have to be found to result in a small uncertainty. These restrictions can be based on measured quantities by the analyzers. From a comparison of the total atomic rates entering the TGA and the BRP, one can get a proof for the stability of the sample and extension tube parameters with time, if α varies significantly during the time of the measurement. Together with the measured quantity α_r^{TGA} it may be possible to limit the recombination parameter of the sample and extension tube in order to decrease the upper limit resulting in a smaller corridor of possible values for α_r [Hen 98].

The calculation for wall relaxation can be done in the same way as presented for recombination. A complete treatment of wall relaxation can be found in [Bau 00].

Chapter 6

Target Polarization of the Run 2000

During the running period of the year 2000, from January to September, very stable running conditions have been observed. The target chamber was never vented[1] during this time and the injected atomic deuterium flux into the storage cell by the atomic beam source was very stable. In addition, the vacuum system of the target gas analyzer and the Breit-Rabi polarimeter did not fail and both detectors including the high frequency transitions operated in a stable manner. In this chapter the stability of the target components will be demonstrated, resulting in a unique value for the target polarization for the whole running period. The validity of a constant target polarization with small errors for the complete data taken in 2000 is shown by the proven long term stability of the target operation. This situation differs from the previous running periods, where the target polarization often changed caused by unstable running conditions.
The target polarization is given by equation (1.6)

$$P^T = \alpha_0 \cdot (\alpha_r + (1 - \alpha_r) \cdot \beta) \cdot P_a \ , \tag{6.1}$$

which may be rewritten using the total atomic fraction α_{tot} by

$$P^T = \alpha_{\text{tot}} \cdot P_a \ , \tag{6.2}$$

where α_{tot} is then given by

$$\alpha_{\text{tot}} = \alpha_0 \cdot (\alpha_r + (1 - \alpha_r) \cdot \beta) \ . \tag{6.3}$$

Knowing the uncertainties of both α_{tot} and P_a, the total uncertainty of the target polarization ΔP^T is calculated by

$$\Delta P^T = \sqrt{\left(\frac{\Delta\alpha_{\text{tot}}}{\alpha_{\text{tot}}}\right)^2 + \left(\frac{\Delta P_a}{P_a}\right)^2} \cdot P^T \ . \tag{6.4}$$

[1]A venting of the target chamber becomes necessary if e.g. the storage cell surface has been damaged during an accidental beam loss into the storage cell walls when the storage cell needs to be replaced.

6.1 Atomic Polarization P_a

For the main analysis of the HERMES data only the positive and negative nuclear polarizations P_z^+, P_z^-, P_{zz}^+ and P_{zz}^- are of interest. The following facts prove that there has been no detectable nuclear depolarization present in the HERMES target during the running period in 2000.

The first argument for a non-depolarizing target storage cell wall is the absence of a temperature dependence of the nuclear polarization. If nuclear wall depolarization has a measurable strength $\gamma_z > 0$, one will see an increase of γ_z with decreasing temperature as the particles stick to the wall much longer according to equation (4.1). Moreover, they will also spend a longer average time τ_c at each site before moving along the surface via jump diffusion. The temperature dependence of γ_z can be expressed by

$$\gamma_z(T) \propto \tau_s \tau_c = \gamma_z^0 \cdot e^{\left(\frac{E_b+E_j}{k_b T}\right)} \tag{6.5}$$

with the the binding energy on the surface E_b and the activation energy for jump diffusion E_j. Baumgarten calculated values of about $28-32$ meV for the sum E_b+E_j from relaxation studies in [Bau 00] for a depolarizing surface. These studies have been repeated for the case of the cell surface during the running period in 2000, where the sum was around $E_b + E_j \simeq 22$ meV. This decrease can be interpreted by a vanishing activation energy for jump diffusion $E_j \simeq 0$ meV. The resulting value of $E_b \simeq 22$ meV is then comparable to the corresponding energy for hydrogen. The vanishing E_j means, that the Drifilm coating (including the water coverage) has been more 'flat' in the sense that the barriers between neighbouring sites are much smaller than for formerly installed storage cells. Thus essentially no localized states exist for the storage cell from 2000. Another consequence of that is a lower local fluctuating magnetic field on the surface [Bau 00] and thus less depolarization. The temperature dependence for the storage cell from 2000 with deuterium gas is shown in figure 6.1. The missing temperature dependence within the full temperature range down to 44 K in case of the cell from 2000 indicates that no depolarization

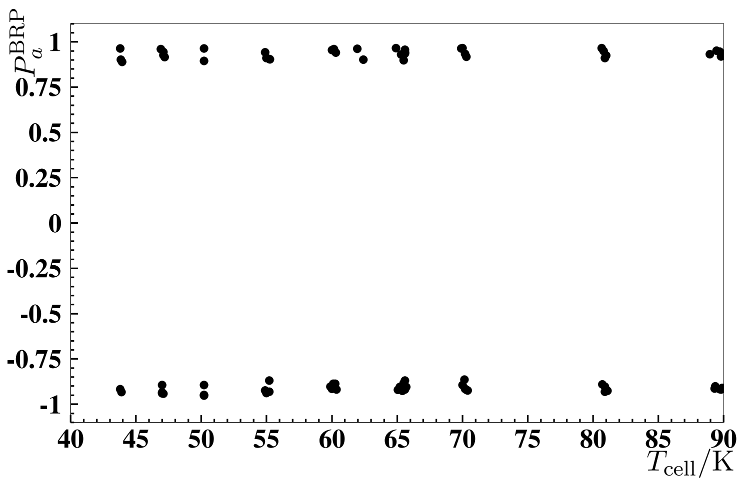

Figure 6.1: Measured vector polarization P_z^{BRP} of deuterium as a function of the cell temperature T_{cell} measured in August 2000. No dependence of the nuclear polarization on the cell temperature can be seen.

ε_{s26}	0.993 ± 0.002	ε_{w14r12}	1.000 ± 0.001
ε_{s35}	0.973 ± 0.002	ε_{w14r24}	1.007 ± 0.029
ε_{t35}	0.980 ± 0.001	ε_{w14r23}	1.000 ± 0.001
ε_{m14r12}	0.988 ± 0.003	ε_{w14r14}	0.997 ± 0.016
ε_{m14r23}	0.993 ± 0.003	ε_{w14r13}	0.995 ± 0.013
ε_{m14r34}	0.982 ± 0.004	ε_{w14r34}	1.000 ± 0.001
		ε_{w14r56}	0.982 ± 0.026

Table 6.1: Fitted transition efficiencies of the ABS in case of deuterium for the first five injection modes of table 3.2. The uncertainties were calculated from the statistical uncertainties of the measured hyperfine populations.

occurs, neither on the cell walls nor in the gas phase by spin exchange collisions. The effect of spin exchange collisions in case of deuterium was less than 0.2%, as mentioned in chapter 4.2.2 already.

Another possibility to prove that the storage cell in 2000 did not depolarize the nucleons in the target gas is to compare the measured polarization by the BRP P^{BRP} with the polarization P^{inj} injected by the ABS. If both agree, no depolarization can have occured during the path of the atoms through the storage cell. The injected polarization can not be measured directly but has to be calculated using the transmissions of the sextupole magnet system and the efficiencies of the high frequency transitions of the ABS that are needed to inject P_z^+ and P_z^-.

The transmission probabilities of the sextupole magnet system of the ABS can be calculated by a tracking program. As the decoupling factor $x \simeq 28$ is large, the transmissions depend only on the value of $m_S = \pm\frac{1}{2}$ [2]. The calculated transmission probabilities in case of deuterium are

$$\begin{aligned}
\sigma_{++} &= 0.450 \\
\sigma_{+-} &= 0.035 \\
\sigma_{-+} &= 0.009 \\
\sigma_{--} &= 0.000\ ,
\end{aligned} \tag{6.6}$$

where the indices refer to the sign of the quantum number m_S with the order of the indices corresponding to the order of sextupole subsystems.

The next step is to derive the efficiencies of the high frequency transitions in the ABS. For this purpose a complete data set giving the hyperfine population in dependence of the magnetic holding field of the target and the temperature of the target storage cell has been measured in October 1998 with deuterium. The magnetic holding field was varied between 0 and 335 mT and the temperatures between 38 and 212 K. The matching of the hyperfine population has been done using a least square fit. The results for the transition efficiencies necessary to describe the first five injection modes in table 3.2 are given in table 6.1. The modelling of the ABS WFT unit was performed using 7 separate efficiencies as described in [Bau 00]. The efficiencies of

[2]In case of hydrogen the decoupling factor $x \simeq 6.7$ is smaller. Here also the quantum number of the proton spin m_I influences the transmission.

the single-photon transitions can be assumed to be unity because they are the first transitions to saturate with increasing amplitude of the high frequency. The single-photon transitions are described by the efficiencies ε_{w14r12}, ε_{w14r23} and ε_{w14r34}. To get the injected polarization by the ABS for the injection of P_z^+ and P_z^- one can, as a first step, calculate the modifications to the hyperfine population of the atomic beam by the sextupole magnet systems including the strong field transition 3-5 (ε_{t35}) in between the two sextupole subsystems. The starting condition is an unnormalized equally populated atomic beam with respect to the different hyperfine states. Applying equation (3.3) and inserting the values from table 6.1 leads - after renormalizing the hyperfine population numbers - to

$$\begin{pmatrix} 1 \\ 1 \\ 1 \\ 1 \\ 1 \\ 1 \end{pmatrix} \overset{\text{sixpole}}{\Longrightarrow} \begin{pmatrix} \sigma_1 \\ \sigma_2 \\ \sigma_3 \\ \sigma_4 \\ \sigma_5 \\ \sigma_6 \end{pmatrix} \overset{\text{SFT 3-5}}{\Longrightarrow} \begin{pmatrix} \sigma_1 \\ \sigma_2 \\ \sigma_3(1-\varepsilon_{t35}) + \sigma_5\varepsilon_{t35} \\ \sigma_4 \\ \sigma_5(1-\varepsilon_{t35}) + \sigma_3\varepsilon_{t35} \\ \sigma_6 \end{pmatrix}$$
$$\overset{\text{sixpole}}{\Longrightarrow} \begin{pmatrix} \sigma_{11} \\ \sigma_{22} \\ \sigma_{33}(1-\varepsilon_{t35}) + \sigma_{53}\varepsilon_{t35} \\ \sigma_{44} \\ \sigma_{55}(1-\varepsilon_{t35}) + \sigma_{35}\varepsilon_{t35} \\ \sigma_{66} \end{pmatrix} \overset{\text{values}}{\Longrightarrow} \begin{pmatrix} 0.450 \\ 0.450 \\ 0.018 \\ 0.000 \\ 0.034 \\ 0.000 \end{pmatrix} \overset{\text{normalized}}{\Longrightarrow} \begin{pmatrix} 0.473 \\ 0.473 \\ 0.019 \\ 0.000 \\ 0.036 \\ 0.000 \end{pmatrix} . \tag{6.7}$$

From this result only the manipulation by the high frequency transitions in the ABS appendix needs to be calculated. In case of the injection of P_z^+ the strong field transition 2-6 in the appendix is used and the weak field transition 1-4/2-3 is used to achieve P_z^-. Applying the corresponding efficiencies from table 6.1 then leads to

$$\begin{pmatrix} 0.473 \\ 0.473 \\ 0.019 \\ 0.000 \\ 0.036 \\ 0.000 \end{pmatrix} \overset{\text{S26}}{\Longrightarrow} \begin{pmatrix} 0.473 \\ 0.003 \\ 0.019 \\ 0.000 \\ 0.036 \\ 0.470 \end{pmatrix} \overset{(2.18)}{\Longrightarrow} P^{\text{inj}}(P_z^+) = +0.924 \pm 0.013 \tag{6.8}$$

and

$$\begin{pmatrix} 0.473 \\ 0.473 \\ 0.019 \\ 0.000 \\ 0.036 \\ 0.000 \end{pmatrix} \overset{\text{W14}}{\Longrightarrow} \begin{pmatrix} 0.000 \\ 0.019 \\ 0.473 \\ 0.473 \\ 0.001 \\ 0.035 \end{pmatrix} \overset{(2.18)}{\Longrightarrow} P^{\text{inj}}(P_z^-) = -0.911 \pm 0.013 \tag{6.9}$$

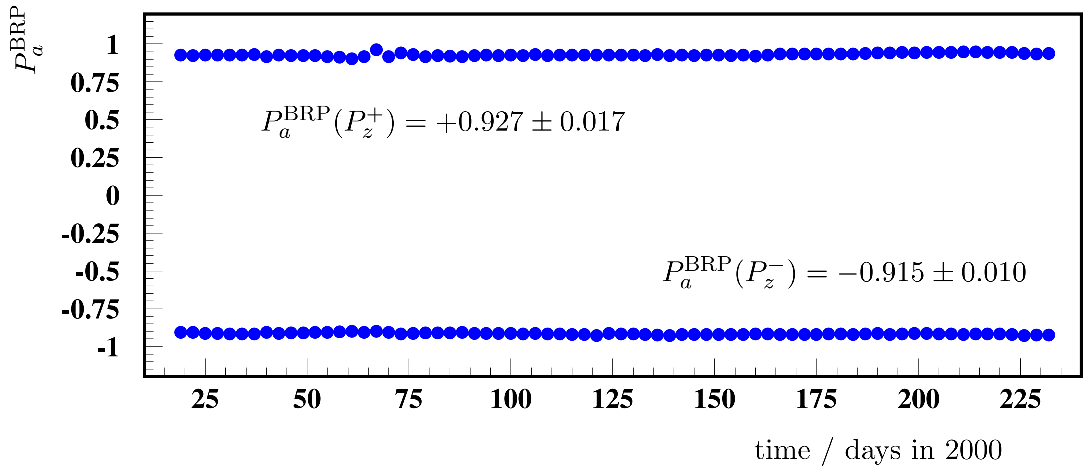

Figure 6.2: Behaviour of the measured atomic vector polarization by the BRP during the complete running period in 2000. The average values are given in the inlets. The data has been rebinned in bins of 60 hours each.

with the values for the injected polarizations calculated by equation (2.18) using a magnetic field value of $B = 335$ mT. The errors can be calculated from the uncertainties of the efficiencies and transmissions. The uncertainty of the transmissions, originating from systematical uncertainties by the Monte-Carlo simulation program, have been estimated to be 0.005 each.
The average of the measured atomic polarization by the BRP for these injection modes over the complete running period 2000 are:

$$P_a^{\mathrm{BRP}}(P_z^+) = +0.927 \pm 0.017 \quad \left(P^{\mathrm{inj}}(P_z^+) = +0.924 \pm 0.013\right) \tag{6.10}$$

$$P_a^{\mathrm{BRP}}(P_z^-) = -0.915 \pm 0.010 \quad \left(P^{\mathrm{inj}}(P_z^-) = -0.911 \pm 0.013\right) \tag{6.11}$$

and can be seen in figure 6.2, where the measurements have been rebinned so that one dot represents the average of about 60 hours. The calculation of the uncertainties has been explained in chapter 3.6 and was carried out using the results of the BRP calibration as given in table 3.5. Within the statistical uncertainty of the measurement the measured atomic polarization by the BRP does not differ within the one to two percent error from the calculated atomic polarization injected by the ABS (equations (6.8) and (6.9)). This fact together with the independece of P_z on the cell temperature leads to the conclusion that no nuclear depolarization can have occured between the injection of the atoms until their detection. A consequence of this special behaviour is that $p_{wd} = 1$ and hence the sampling correction equals unity ($c_p = 1$). The average

Inj. Mode	Inj. States	P_e	P_z	P_{zz}
P_z^+	$\vert 1\rangle + \vert 6\rangle$	0.0038 ± 0.0093	$+0.927 \pm 0.017$	$+0.871 \pm 0.011$
P_z^-	$\vert 3\rangle + \vert 4\rangle$	0.0040 ± 0.0100	-0.915 ± 0.010	$+0.929 \pm 0.012$
P_{zz}^+	$\vert 3\rangle + \vert 6\rangle$	-0.0028 ± 0.0020	-0.011 ± 0.003	$+0.971 \pm 0.010$
P_{zz}^-	$\vert 2\rangle + \vert 5\rangle$	0.0046 ± 0.0034	-0.011 ± 0.005	-1.803 ± 0.014

Table 6.2: All polarization values (P_e, P_z and P_{zz}) for deuterium averaged over the whole year 2000 for the injection modes P_z^+, P_z^-, P_{zz}^+ and P_{zz}^-. The injected hyperfine states are given in the second column. For details about the hardware configuration for each injection mode refer to table 3.2.

atomic polarization along the beam tube of the storage cell is then equal to the measured atomic polarization in the BRP:

$$P_a = P_a^{\mathrm{BRP}} \ . \tag{6.12}$$

The argumentation presented for the vector polarization also applies for the tensor polarization, where no temperature dependence could be measured and the measured values by the BRP were within the errors in agreement to the injected polarization as well.
Together with the dedicated tensor polarized deuterium data sets also taken in 2000, the complete set of atomic polarizations in the target for the HERMES main analysis are listed in table 6.2. The listed injection modes are explained in table 3.2 in more detail.

6.2 Total Atomic Fraction α_{tot}

The second factor - besides P_a - entering the calculation of the target polarization is the total atomic fraction α_{tot}, defined by equation (6.3):

$$\alpha_{\mathrm{tot}} = \alpha_0 \cdot (\alpha_r + (1 - \alpha_r) \cdot \beta) \ . \tag{6.13}$$

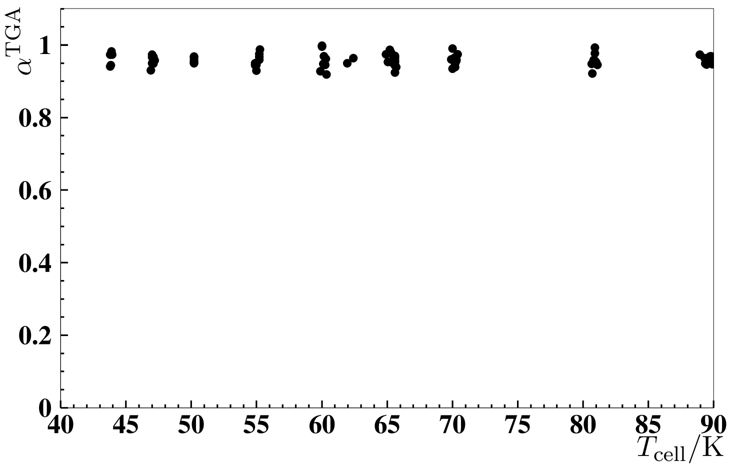

Figure 6.3: Measured atomic fraction α^{TGA} of deuterium as a function of the cell temperature T_{cell} measured in August 2000. No dependence of the atomic fraction on the cell temperature can be seen.

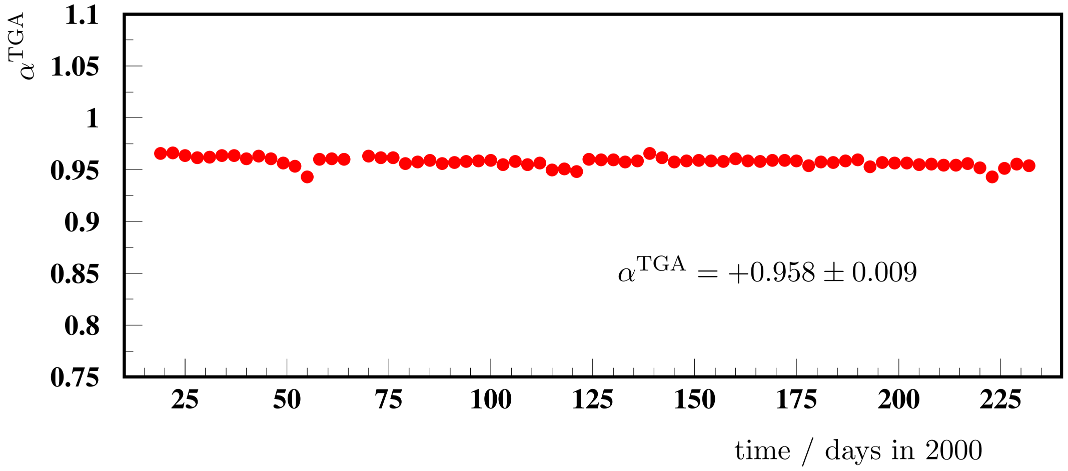

Figure 6.4: Behaviour of the measured atomic fraction by the TGA during the complete running period in 2000. The average value is given in the inlet. The data has been rebinned in bins of 60 hours each.

With the same reasoning as used in case of the atomic polarization, one can conclude from the independence of the measured atomic fraction $\alpha^{\rm TGA}$ on the storage cell temperature that no (or at least very little) recombination takes place on the storage cell walls, which would lead to $\alpha_r^{\rm TGA} \simeq 1$ and thus $\alpha_r \simeq 1$ as well. The sampling correction equals unity in case of absent recombination. The measured atomic fraction $\alpha^{\rm TGA}$ during the same temperature scan as for the atomic polarization in figure 6.1 is shown in figure 6.3. The behaviour of the measured atomic fraction over the complete running period in 2000 can be seen in figure 6.4. The data points in this plot have been rebinned so that one dot represents the average of about 60 hours. As the measured atomic fraction $\alpha^{\rm TGA}$ for 2000 is very stable with time one average value for the whole year can be given. This average is

$$\alpha^{\rm TGA} = 0.958 \pm 0.009 \ . \tag{6.14}$$

To be able to calculate α_0 from the measured fluxes ϕ_a, ϕ_m and the calculated fluxes ϕ_{rg}, ϕ_{ball} (for details see chapter 3.5.2), one can define α_0 similar to $\alpha_0^{\rm TGA}$ in equation (3.22) as

$$\alpha_0 = \frac{n_a + 2n_r}{n_a + 2n_r + 2n_{ball} + 2n_{rg}} \tag{6.15}$$

with the number of atoms n_a and the number of molecules from the different sources n_r, n_{ball} and n_{rg}. The normalized total density ρ_t is given by

$$\rho_t = \rho_a + \sqrt{2}\rho_m = \sqrt{2} - (\sqrt{2} - 1)\rho_a \tag{6.16}$$

as it is used as denominator in equation (1.5). Hence it follows that

$$n_a + 2n_r \propto \frac{\sqrt{2}}{1+(\sqrt{2}-1)\alpha_r} \cdot (\phi_a + \phi_r) \ . \tag{6.17}$$

The other fluxes ϕ_{ball} and ϕ_{rg} have to multiplied by a factor of $\sqrt{2}$ to give the corresponding density inside the storage cell. As the density of the residual gas contribution is equally distributed (instead of the triangular shape of the other densities), the molecular flux caused by residual gas has to be weighted twice. Transfering equation (6.15) to the measured fluxes by the TGA thus results in

$$\alpha_0 = \left(1 + (1+(\sqrt{2}-1)\alpha_r) \cdot \frac{\phi_{ball} + 2\phi_{rg}}{\phi_a + \phi_r}\right)^{-1} \tag{6.18}$$

and in case of low recombination as shown in figure 6.3 with $\alpha_r \simeq 1$:

$$\alpha_0 \simeq \frac{\phi_a + \phi_r}{\phi_a + \phi_r + \sqrt{2}(\phi_{ball} + 2\phi_{rg})} \ . \tag{6.19}$$

Applying the sampling correction for the small cell dimensions as valid for the year 2000 from equation (5.13) to equation (1.7), α_r is given by

$$\alpha_r = c_\alpha \cdot \alpha_r^{\mathrm{TGA}} = (x+1)\alpha_r^{\mathrm{TGA}} - x \tag{6.20}$$

with $x = 0.83 \pm 1.27$.

Substituting (6.20) in equation (6.3) and transposing the result leads to

$$\alpha_{\mathrm{tot}} = \alpha_0 \left(\beta + (x+1)(1-\beta)\alpha_r^{\mathrm{TGA}} - x(1-\beta)\right) \tag{6.21}$$

and hence using equation (6.19) and (3.21)

$$\alpha_{\mathrm{tot}} = \frac{\phi_a + (x(\beta-1)+\beta)\,(\phi_m - \phi_{ball} - \phi_{rg})}{\phi_a + \phi_m + (\sqrt{2}-1)\phi_{ball} + (2\sqrt{2}-1)\phi_{rg}} \tag{6.22}$$

follows after a few simplifications.

The calculation of the systematic uncertainty of α_{tot} depends on the measured fluxes and their uncertainties as well as the values and uncertainties of β, x and the calibration constant of the TGA κ. With the matrix T defined by

$$T = \left(\frac{\partial \alpha_{\mathrm{tot}}}{\partial \phi_i}, \ldots, \frac{\partial \alpha_{\mathrm{tot}}}{\partial \kappa}\right) \tag{6.23}$$

and the diagonal covariance matrix C of all calibration constants, the systematical uncertainty $\Delta\alpha_{\mathrm{tot}}$ is given by

$$\Delta\alpha_{\mathrm{tot}} = \sqrt{(T\,C\,T^T)} \ . \tag{6.24}$$

The matrix T contains in total 10 independent derivatives, i.e. for κ, β, x, c_{rg}, and two for each p_{TC}, ϕ_a and ϕ_m entering the calculation of ϕ_{ball} exclusively. Thus one may collect the uncertainties of these values in a reduced uncertainty $\Delta\phi_{ball}$ which excludes the uncertainty of c_{rg}. The remaining derivatives can be calculated from equation (6.22) by

$$\frac{\partial\alpha_{\text{tot}}}{\partial\kappa} = \frac{(x(\beta-1)+\beta-\alpha_{\text{tot}})\,(\phi_m-\phi_{ball}-\phi_{rg}) - \sqrt{2}\,\alpha_{\text{tot}}(2\phi_{rg}+\phi_{ball})}{\kappa\left(\phi_a+\phi_m+(\sqrt{2}-1)\phi_{ball}+(2\sqrt{2}-1)\phi_{rg}\right)} \tag{6.25}$$

$$\frac{\partial\alpha_{\text{tot}}}{\partial\beta} = \frac{(x+1)\,(\phi_m-\phi_{ball}-\phi_{rg})}{\phi_a+\phi_m+(\sqrt{2}-1)\phi_{ball}+(2\sqrt{2}-1)\phi_{rg}} \tag{6.26}$$

$$\frac{\partial\alpha_{\text{tot}}}{\partial x} = \frac{(\beta-1)\,(\phi_m-\phi_{ball}-\phi_{rg})}{\phi_a+\phi_m+(\sqrt{2}-1)\phi_{ball}+(2\sqrt{2}-1)\phi_{rg}} \tag{6.27}$$

$$\frac{\partial\alpha_{\text{tot}}}{\partial\phi_{ball}} = -\frac{x(\beta-1)+\beta+(\sqrt{2}-1)\alpha_{\text{tot}}}{\phi_a+\phi_m+(\sqrt{2}-1)\phi_{ball}+(2\sqrt{2}-1)\phi_{rg}} \tag{6.28}$$

$$\frac{\partial\alpha_{\text{tot}}}{\partial c_{rg}} = -\frac{\left(x(\beta-1)+\beta+(\sqrt{2}-1)\alpha_{\text{tot}}\right)\left(p_{TC}+\frac{\partial\phi_{ball}}{\partial c_{rg}}\right)+\sqrt{2}\,\alpha_{\text{tot}}\,p_{TC}}{\phi_a+\phi_m+(\sqrt{2}-1)\phi_{ball}+(2\sqrt{2}-1)\phi_{rg}}\,, \tag{6.29}$$

with

$$\frac{\partial\phi_{ball}}{\partial c_{rg}} = -\frac{\phi_a^{(1)}\,p_{TC}^{(2)}-\phi_a^{(2)}\,p_{TC}^{(1)}}{\phi_a^{(1)}-\phi_a^{(2)}} \tag{6.30}$$

calculated from equation (3.27), which is also used to calculate the value of $\Delta\phi_{ball}$ given by

$$\Delta\phi_{ball} = \sqrt{\frac{\left(\begin{array}{r}\left(\phi_r^{(2)}\,\Delta\phi_a^{(1)}\right)^2+\left(\phi_r^{(1)}\,\Delta\phi_a^{(2)}\right)^2+\left(\phi_a^{(2)}\,\Delta\phi_m^{(1)}\right)^2+\left(\phi_a^{(1)}\,\Delta\phi_m^{(2)}\right)^2\\ +\left(\phi_a^{(2)}\,c_{rg}\,\Delta p_{TC}^{(1)}\right)^2+\left(\phi_a^{(1)}\,c_{rg}\,\Delta p_{TC}^{(2)}\right)^2\end{array}\right)}{\left(\phi_a^{(1)}-\phi_a^{(2)}\right)^2}}\,. \tag{6.31}$$

As seen in figure 6.2 and 6.4 the target performance was very stable during the year 2000. Thus only the averaged values may be taken into account calculating α_{tot} with equation (6.22) to get one averaged α_{tot} for the complete running period. The averaged values for 2000 are:

$$\begin{array}{rclrcl}
\phi_a &=& 39.92\pm3.50\,\frac{\text{kHz}}{\text{mA}} & \kappa &=& 0.849\pm0.029\\
\phi_m &=& 1.72\pm0.66\,\frac{\text{kHz}}{\text{mA}} & c_{rg} &=& (5.36\pm0.24)\cdot10^{-6}\,\frac{\text{kHz}}{\text{mA}\cdot\text{mbar}}\\
\phi_{rg} &=& 0.63\pm0.09\,\frac{\text{kHz}}{\text{mA}} & x &=& 0.83\pm1.27\\
\phi_{ball} &=& 0.31\pm0.08\,\frac{\text{kHz}}{\text{mA}} & \beta &=& 0.5\pm0.5
\end{array}\,. \tag{6.32}$$

The numbers given for $\beta = 0.5\pm0.5$ reflect the highest possible uncertainty on that quantity as β per definition (see chapter 1.4) is between 0 and 1. The polarization of molecules originating from a recombination of two polarized deuterium atoms on a drifilm coated aluminum surface is unknown[3]. In case of low recombination the uncertainty of β has a negligible influence on the

[3]Although values for β have been measured for hydrogen molecules [Wie 01] and for deuterium molecules [vBr 97], they can not be transfered to the experimental conditions of the HERMES experiment.

uncertainty of α_{tot}.
With the above given values one calculates an averaged

$$\alpha_{\mathrm{tot}} = 0.916 \pm 0.025 \tag{6.33}$$

for the running period in 2000.

6.3 Results

With the results for the atomic polarizations from table 6.2 and for the total atomic fraction from equation (6.33) it is now possible to calculate the corresponding target polarizations and their uncertainties using equations (6.1) and (6.4). The results for the average target polarization in 2000 are:

$$\begin{aligned} P^T_{z+} &= +0.849 \pm 0.027 \\ P^T_{z-} &= -0.838 \pm 0.024 \\ P^T_{zz+} &= +0.889 \pm 0.026 \\ P^T_{zz-} &= -1.652 \pm 0.046\ . \end{aligned} \tag{6.34}$$

Thus the relative uncertainties are for all four polarizations between 2.8% and 3.2%.
Due to the better quality of the storage cell surface and the high decoupling factor for deuterium, the factors that lead to a reduction of the target polarization are α_0 and P^{inj}. Therefore, the most dominant error contributions from the sampling corrections in case of measurable recombination and nuclear depolarization vanish and result in a total uncertainty of the target polarization of about 3% only.

Chapter 7

Discussion and Outlook

Within the present work all relevant technical and physical aspects of the HERMES target have been discussed in order to calculate and understand the target polarization and its uncertainty for the running period with deuterium gas in 2000.

A special remark should be made concerning the fact that the given polarization values are calibrated by using the complete analyzing apparatus of the target setup only. The only quantity entering the calculation of the target polarization, which is not (yet) derived from measurements of the HERMES target itself, is the spin exchange cross section σ_{se}. Measurements, making use of the magnetic field dependence of spin exchange relaxation, have been used to derive the atomic target density $\langle\, n\,\rangle$ with a given σ_{se} [Bau 00]. If $\langle\, n\,\rangle$ can be derived otherwise, σ_{se} becomes experimentally accessible at the HERMES target setup. Provided that the unpolarized gas feed system can be calibrated such as to allow an absolute knowledge of the target density[1] with a maximum uncertainty of about 2%, σ_{se} can be derived from spin relaxation measurements with a presumptive precision of 5%.

One reason for the general possibility to achieve the quoted precision of the target polarization, together with a complete understanding of the present spin relaxation processes, is that the Breit-Rabi polarimeter does not only measure the atomic nuclear and/or electron polarization but derives them from the measured hyperfine state population. The knowledge about the hyperfine state population of the sample beam is crucial for most of the relaxation studies that have been carried out at the HERMES target so far. Other methods of polarimetry of spin polarized atomic gases (e.g. using a Lamb shift polarimeter (LSP) [Zel 86, Lem 93, Ens 02]), which measure only the nuclear polarization, lose the information about the electron spin and thus the information about the exact hyperfine state population.

[1] Although polarized atomic gas is needed for spin relaxation measurements, the UGFS is needed to cross-calibrate the TGA to enable it not only to observe relative changes of the target density but also to give absolute values for $\langle\, n\,\rangle$.

On the way to the absolutely calibrated target polarization the calibrations of the target gas analyzer and the Breit-Rabi polarimeter have been discussed in detail. In that context the analysis of a BRP calibration measurement has been modified successfully to allow the simultaneous derivation of transition efficiencies and sextupole transmission ratios using the approximative optimization method of the variable size simplex algorithm. The calibration of the BRP has also been discussed in the context of the BRP as an absolute monitor of the temperature dependent total atomic beam intensity $I_{\mathrm{tot}}(T_{\mathrm{cell}})$. The temperature dependence, caused by the sextupole magnet system in the BRP, that transmits atoms within two certain velocity windows only, has been studied and calculated based on measurements. These measurements have been carried out with a new technique of pulse modulated high frequency transitions which allows to perform time of flight (TOF) measurements without a mechanical chopper. A high frequency transition is then effectively used as a beam chopper [Bau 02c]. The results of these measurements agree with simulations by means of a tracking program for atoms through the magnetic field of the sextupole magnets. Making use of these informations, a new sextupole magnet system has been designed to increase the total atomic beam intensity into the BRP [Bru 01]. The gain factor of this optimization is about 1.8 for $T_{\mathrm{cell}} \simeq 95$ K and about 4 for $T_{\mathrm{cell}} \simeq 60$ K. These temperatures are of major interest because they are the standard operating temperatures for hydrogen and deuterium at the HERMES target.

The same technique applied to the weak field transition in the appendix of the atomic beam source delivered a measurement of the time dependence of the hyperfine state population after a flip of the injection mode. The model to describe spin relaxation, the master equation, has been fitted to the measured time dependence. It was shown, that the master equation is able to describe the observed behaviour accurately. The fitted parameters are in agreement to other measurements and simulations.

For the running period in 2000 it has been shown that no detectable recombination or nuclear depolarization of the target gas atoms occured. Both recombination and depolarization showed no dependence on the temperature of the storage cell although there was a clear temperature dependence in previous years both for hydrogen and deuterium [Kol 98, Bau 00]. There are several explanations for this extraordinary behaviour:

- It could be shown that the activation energy for jump diffusion on the storage cell surface vanishes. Consequently, physisorbed atoms may freely diffuse on the surface without seeing locally fluctuating magnetic fields that could depolarize the nucleus.

- For the same reason the average time τ_c a physisorbed atom stays at a localized site is constant and equal to the high temperature limit τ_c^0 which is of the order of 10^{-13} seconds.

This might suppress the L-H type recombination processes between two physisorbed atoms as they spend only very little time at each surface site.

- The other process that can cause recombination at low temperatures, i.e. the recombination of physisorbed atoms with chemically bond atoms [Boh 98] that can be understood by tunneling through the barrier of the binding energy E_b, is completely suppressed by an ice layer on the storage cell surface. This ice layer grows onto the storage cell walls due to the fact, that the continueous irradiation by the HERA beam causes the Drifilm coating to lose its hydrophobic properties. It shields the surface from direct chemical attacks of the target gas radicals, and might have been even thicker than in the previous years because the operating temperature of the storage cell was $T_{\text{cell}} \simeq 60$ K only (compared to $T_{\text{cell}} \simeq 85$ K in 1998 and 1999).

- The storage cell has never warmed up to room temperature in 2000 as it had been the case several times in the previous running periods. Neither was the storage cell surface destroyed by an accidental HERA beam loss nor did any of the hardware inside the vacuum fail during the whole period.

The fact that the deuterium gas target was recombination and depolarization free in 2000 can be completely understood with the theoretical models presented in this study.
Another possible reason was found after the surface coating of the 2000 cell has been investigated. It was observed that the Drifilm coating was about twice as thick as for previous cells [Len 02]. Nevertheless, as studied after the 2000 run, the same storage cell did show significant recombination after its water coverage had been removed once and built-up again. That leads to the conclusion that also the lower operating cell temperature (compared to hydrogen) had a large effect on the good performance.
Questions for the future operation with storage cells in polarized atomic hydrogen and deuterium gas targets are, how to reproduce the thicker surface coating as it was observed for the cell used in 2000 and whether there are better coating materials than Drifilm. Baumgarten proposed tests with LiF or similar ionic crystals as coating material because they are promising with respect to recombination and spin relaxation. The binding energies of LiF for physisorbed hydrogen and deuterium are about half of those for Drifilm [Fin 75]. Additionally, LiF would not be attacked by gas radicals as the bond strength of LiF is larger than those of H-F, H-Li, H-H and the corresponding molecules containing deuterium instead of hydrogen [Dan 64].
For the coming running period of the HERMES target with transversely polarized hydrogen, most of the knowledge about recombination and spin relaxation can be transferred easily from the experience gained during the longitudinal running.
An additional strong field transition unit in the ABS allows a preciser determination of the bal-

listic flux of molecules ϕ_{ball} than in the running period 1996/97 with hydrogen. The improved systematical precision results from the possibility to defocus all hyperfine states with the help of high frequency transitions and two sets of sextupole magnets. Thus only molecules may be injected ballistically into the cell using this injection mode P_{no}, allowing a direct determination of ϕ_{ball}.

Further studies are required to measure the bunch field induced resonance conditions in the transversal magnetic field of the target magnet. These resonances need to be known in order to find an operating condition, where this spin relaxation channel can be suppressed. The spacing between the different resonances is much smaller than in a longitudinal magnetic field as a transverse field additionally allows for σ-transitions.

Another open question concerns the value of the polarization of molecules originating from a recombination of two polarized atoms. The large uncertainty of β quickly becomes relevant for the precision of the target polarization as soon as recombination takes place on the storage cell walls. It is highly desirable to perform measurements of β as in references [vBr 97, Wie 01] for hydrogen and deuterium on a cold, drifilm coated aluminum surface. A measurement of molecular polarization is impossible by using a Breit-Rabi type polarimeter. However, the recently developed Lamb shift polarimeter [Ens 02] for the ANKE target is supposed to be used also for the CELGAS project. The program of this project is to measure β for different types of surfaces and could be easily supplemented by measurements for the HERMES experimental conditions.

Appendix A

The Vacuum System of Breit-Rabi Polarimeter and Target Gas Analyzer

The target gas analyzer (TGA) and the Breit-Rabi polarimeter (BRP) share the vacuum system as shown in figure A.1. The two vacuum chambers are pumped differentially with a total nominal pumping speed of about 7000 l/s.

The first vacuum chamber consists of two connected chambers, where the *TGA chamber* contains the target gas analyzer (a beam chopper plus a quadrupole mass spectrometer (QMS) with a channel electron multiplier (CEM) for single ion detection, see also chapter 3.5) and a titanium sublimation pump with a nominal pumping speed of about 1000 l/s, whereas the so-called *sextupole chamber* contains the high frequncy transition (HFT) units and the sextupole magnet system of the Breit-Rabi polarimeter. The sextupole chamber is connected to two cryo pumps with a nominal pumping speed of about 2000 l/s each. Two forepump/turbo pump systems are used for the startup of the vacuum and regeneration of the cryo pumps.

This first vacuum chamber can be separated from the *detection chamber* using a valve. The detection chamber contains the detection system of the BRP (which is similar to the TGA) and a titanium sublimation pump with a nominal pumping speed of about 2000 l/s plus an ion getter pump with a pumping speed of about 60 l/s for heavier particles. Also this vacuum chamber is connected to a forepump/turbopump system for pumping down the detection chamber.

To decrease the residual gas pressure in the vacuum chambers the TGA chamber and the detection chamber can be baked out with temperatures of up to 220 °C after startup. The sextupole chamber must not be baked out as the sextupole magnets lose quality when they get too warm ($T_{\mathrm{sixpole}} < 40$ °C). To keep the magnets cold enough the sextupole chamber is even cooled by a waterflow of 18 °C.

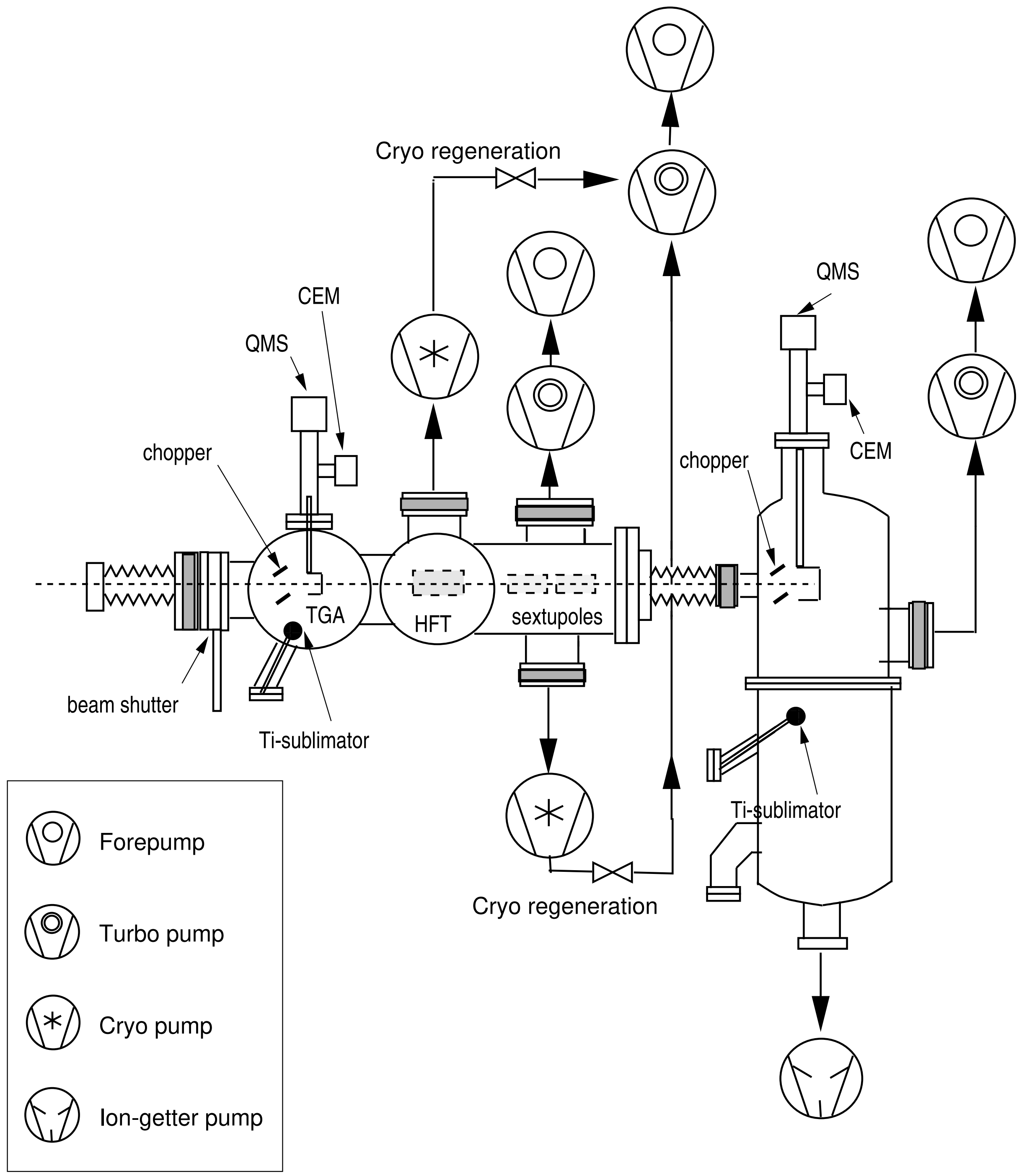

Figure A.1: Schematic of the vacuum system of the target gas analyzer (TGA) and the Breit-Rabi polarimeter (BRP).

Appendix B

Rules for Simplex Movements within the Variable Size Simplex Algorithm

If the factor space is of dimension k, a single simplex consists of $k + 1$ vertices (corner points). Each vertex is evaluated by a response function $f(x)$. This function is usually unknown in evolutionary operation, but the technique can also be used for known systems of high complexity. For the BRP calibration, this function is given by the negative of the definition of χ^2 from equation (3.50):

$$f(x) = -\chi^2 = -\sum_i \left(\frac{(S - M\,I)_i}{(\sigma_S)_i} \right)^2 \quad . \tag{B.1}$$

The unknown parameters x (consisting of the efficiencies ε and the transmission ratios σ) are included in the *measurement matrix M*. The number of unknowns and thus the dimension k of the factor space for the optimization of the parameters is $k = 43$ in case of deuterium (and $k = 11$ in case of hydrogen).

After all 44 start vertices are evaluated using equation (B.1), the vertex (factor combination) leading to the worst response (i.e. the highest χ^2-value) is marked with a **W** (wastebasket). The worst of the remaining vertices is marked with a **N** (next-to-wastebasket). The vertex with the best response is marked with a **B** (best). In the next simplex generation, the former **W**-vertex will be replaced by a new vertex. Like this, the simplex will move into a certain direction each step. The new vertex will be on the line connecting the **W**-vertex with the arithmetic average of the remaining vertices **M**. The position depends on the responses at the different vertices. One example for a two-dimensional factor space is given in figure B.1.

Before it is decided wheather the simplex will increase its size (expansion) or decrease it (contraction), the vertex **W** is reflected at **M**, resulting the new vertex **R**. The response $f(\mathbf{R})$ at this vertex may now be either worse than at the vertex **N**, better than at the vertex **B** or somewhere between both values. The first scenario will lead to a contraction ($\mathbf{C_W}$, if $f(\mathbf{R}) < f(\mathbf{W})$ and

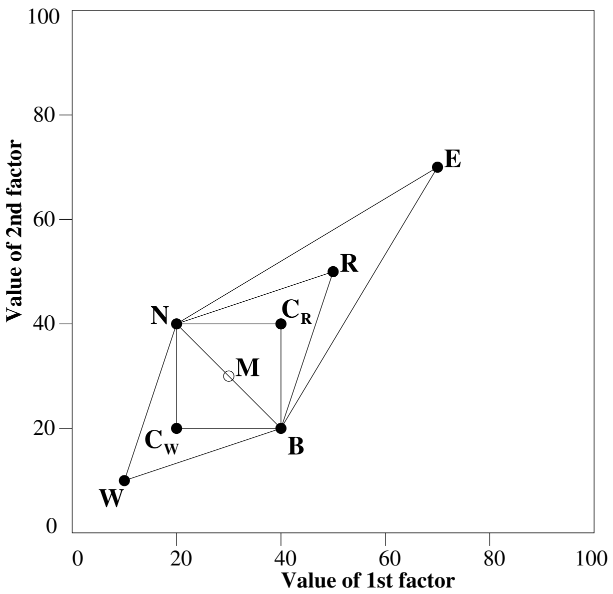

Figure B.1: Possible moves of a variable size simplex in a two-dimensional factor space. **W** (wastebasket) will be replaced by any of the vertices **E** (expansion), **R** (reflection), $\mathbf{C_R}$ or $\mathbf{C_W}$ (contraction) on the connecting straight line of **W** and the average **M** of the remaining vertices **N** (next-to-wastebasket) and **B** (best).

$\mathbf{C_R}$, if $f(\mathbf{R}) \geq f(\mathbf{W})$). The second scenario leads to a possible expansion (**E**), if $f(\mathbf{E}) \geq f(\mathbf{B})$ and to a simple reflection (**R**) in all other cases:

- $f(\mathbf{R}) < f(\mathbf{N}) \Longrightarrow$ Contraction:
  - $f(\mathbf{R}) < f(\mathbf{W}) : \mathbf{C_W}$
  - $f(\mathbf{R}) \geq f(\mathbf{W}) : \mathbf{C_R}$
- $f(\mathbf{N}) \leq f(\mathbf{R}) \leq f(\mathbf{B}) \Longrightarrow$ Reflection (keep **R**)
- $f(\mathbf{R}) > f(\mathbf{B}) \Longrightarrow$ Expansion:
  - $f(\mathbf{E}) < f(\mathbf{B})$: Reflection (keep **R**)
  - $f(\mathbf{E}) \geq f(\mathbf{B}) : \mathbf{E}$

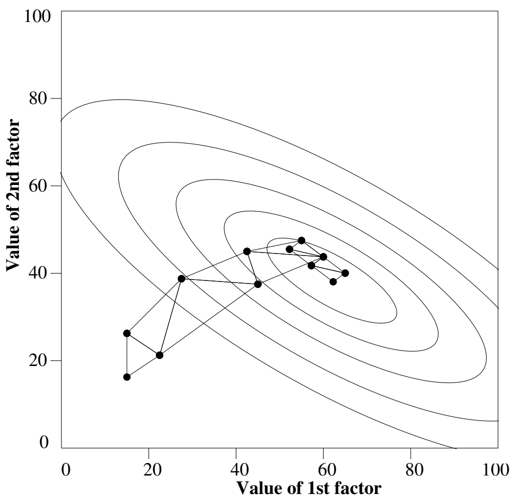

Figure B.2: A complete sequence of a possible optimization process with the variable size simplex algorithm for a simple case of $k = 2$. The points on each ellipse result the same value of the corresponding response function. One can see how the simplex moves towards the optimum and changes its size meanwhile.

The strength of both expansion and contraction can be varied. Studies on the convergence of the variable size simplex algorithm have been performed [Hen 02] and resulted the fastest convergence with an expansion strength of $c_{\text{exp}} = 2$ and a contraction strength of $c_{\text{con}} = 0.4$. These strengths are multiplied to the basic movement vector $(\mathbf{M} - \mathbf{W})$ to reach the vertex $\mathbf{E}$ in case of an expansion and $\mathbf{C_W}$ or $\mathbf{C_R}$ in case of a contraction. In both cases the starting vertex for the movement will be the vertex $\mathbf{M}$. For a simple two-dimensional example a complete sequence of simplex-movements during an optimization process can be seen in figure B.2.

Appendix C

Hardware Control and Online Monitoring

The data aquisition (DAQ) system of the HERMES target is integrated into the HERMES DAQ system. Two tasks have to be fulfilled by the target DAQ:

- The slow control (SC). The programs of the slow control system are read ADC (analog digital converter) modules via CAMAC interface (computer automated measurement and control) in time intervals of typically several seconds up to a minute. With the help of the slow control, values like vacuum pressures, pick up amplitudes, temperatures etc. are monitored.

- The *brpclient* program. This software controls the hyperfine transitions of the ABS and the BRP and therefore defines the target polarization status and controls the measurements of the TGA and BRP. To minimize the delay between the sending of a command and its execution, all necessary commands for one measurement are stored in a *front end list* (FEL). This FEL is then sent to the HERMES DAQ system[1], where the control signals for the power supplies etc. are distributed to DAC modules (digital analog converter). The measurements of the TGA and the BRP and optionally the evaluation of the spectra of the time resolving counter (TRC) is done by the multi scaler input (MSI) of the DSP (digital signal processor) board. This DSP is connected to the FEL via a Fastbus and therefore causes a minimal delay. When the measurement is finished, the results are transferred back to the *brpclient* as a list of BRP and TGA count rates for the chopper open and chopper closed position of each measured beam signal. From this data the *brpclient* then evaluates the beam signal by background subtraction and calculates the hyperfine population and

[1] The connection between the online computers, where the *brpclient* is running, and the HERMES DAQ is the bottleneck of the system.

atomic fraction of the sample beam.

All the data is then stored in ADAMO (ALEPH data model) tables and sent to the DAD server (distributed ADAMO database) [Wan 95]. The same data is also stored as *user events* in EPIO records (experimental physics input output).

The *brpclient* is controlled via the *brpclient control panel*, a PinK script, via the DAD server connection. PinK is a DAD extension of Tcl/Tk (tool command language / toolkit), which allows to write small monitoring and controlling tasks [Ack 95]. Major parts of the HERMES online monitoring system are written in PinK, which was developed together with DAD by the HERMES software group.

In figure C.1 the main relevant parts of the HERMES target controlling and monitoring system are shown.

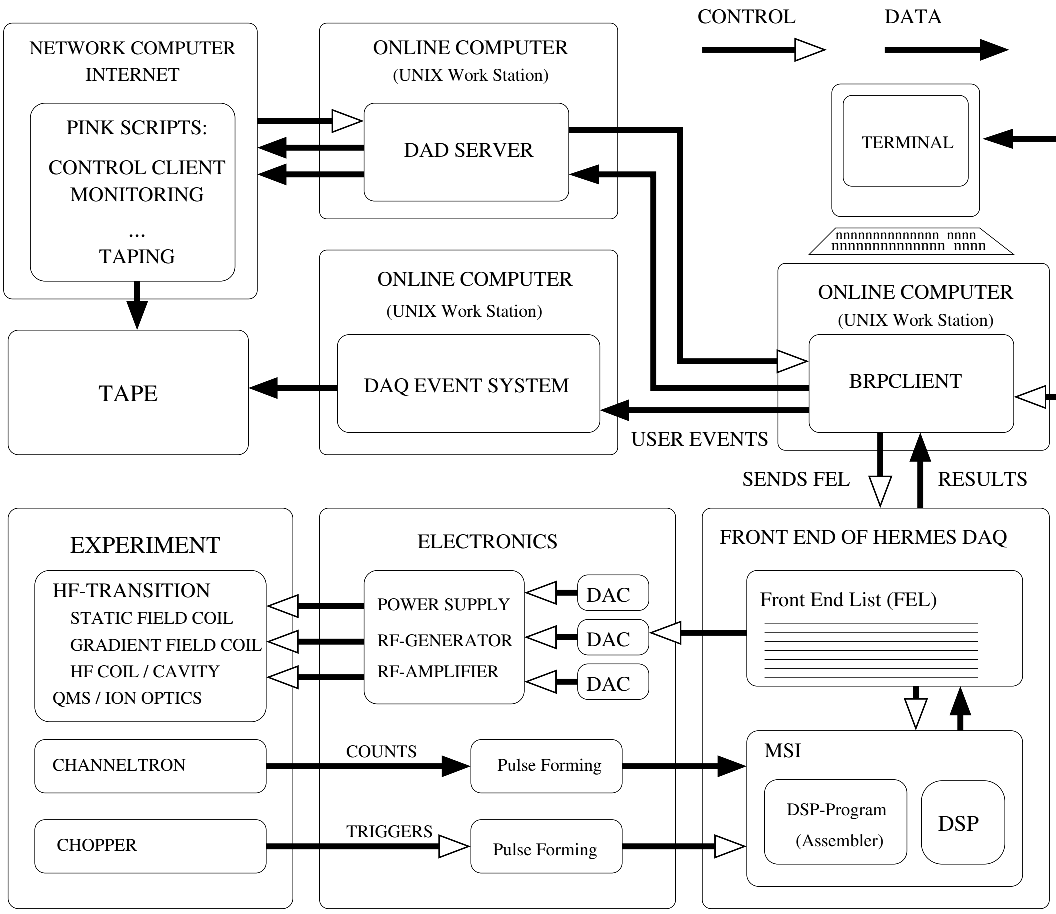

Figure C.1: Schematic of the HERMES target DAQ system, which is controlling the different components.

Appendix D

Glossary of Symbols

In the following, the most important symbols of this work, that occur in the context of calculating or understanding the target polarization, shall be listed and shortly explained.

$\vec{N}$	Vector of normalized hyperfine state population numbers. Each element N_i represents the probability of an atom to be in the corresponding state $\|\, i \,\rangle$ (hydrogen: $i = 1, \ldots, 4$; deuterium: $i = 1, \ldots, 6$).
$\theta, \theta_\pm$	Mixing angles for hydrogen and deuterium. For definitions see chapter 2.1.
x	Ratio of magnetic field and critical magnetic field for hydrogen or deuterium.
$\Phi_{a,m}$	Atomic (molecular) fluxes per unit time in $\frac{\text{atoms}}{\text{s}}$ ($\frac{\text{molecules}}{\text{s}}$).
$\tilde{\Phi}^{\text{TGA}}$	Effective flux of atoms in both atoms and molecules into the TGA (in $\frac{\text{atoms}}{\text{s}}$).
$S_{a,m}$	Detected atomic (molecular) beam rates by either TGA or BRP in $\frac{\text{atoms}}{\text{s}}$ ($\frac{\text{molecules}}{\text{s}}$).
$\phi_{a,m}$	Normalized flowrates for effective fluxes of atoms in both atoms and molecules (in $\frac{\text{atoms}}{\text{s}}$) after being corrected for the different sensitivity of the TGA.
κ	Relative sensitivity of the TGA for atomic and molecular beam (see chapter 3.5).
P^T	Effective average polarization of all nucleons inside the storage cell of the target along the beam tube, i.e. as seen by the HERA electron beam.
P_a	Polarization of atoms. A possible superscript refers to the position, where the polarization is measured, where no index denotes the average atomic polarization along the beam tube.
P_m	Polarization of molecules that originate from the recombination of two polarized atoms.
β	Ratio of P_m and P_a. The values are per definition limited by $0 \leq \beta \leq 1$.
P^{inj}	Injected atomic polarization by the atomic beam source.
P_e	Electron polarization of atoms. The values are per definition limited by $0 \leq P_e \leq 1$.
P_z	Nuclear vector polarization of atoms. A possible superscript refers to the sign of the injected polarization. The values are per definition limited by $-1 \leq P_z \leq 1$.
P_{zz}	Nuclear tensor polarization of atoms. A possible superscript refers to the sign of the injected polarization. The values are per definition limited by $-2 \leq P_{zz} \leq 1$.

p_{wd}	Polarization surviving wall relaxation. $(1 - p_{wd})$ is the polarization loss due to wall relaxation.
p_{se}	Polarization surviving spin exchange relaxation. $(1 - p_{se})$ is the polarization loss due to spin exchange relaxation.
α	Degree of dissociation (or atomic fraction), i.e. the number of nucleons in atoms devided by the total number of nucleons (in atoms *and* molecules).
α_0	Initial atomic fraction. $(1 - \alpha_0)$ is the amount of molecules, that enter the storage cell already as unpolarized molecules.
α_r	Atomic fraction surviving recombination. $(1 - \alpha_r)$ is the amount of molecules produced by recombination of two polarized atoms inside the storage cell.
I_{tot}	Total atomic intensity into a detector.
$P_\sigma(v)$	Velocity dependent transmission function of a sextupole magnet system.
c_α, c_p	Sampling corrections. They correlate the measured quantities by TGA and BRP to the average value along the beam tube of the storage cell.
τ_d	*Time of diffusion*, i.e. the average time that an atom spends in the storage cell.
τ_s	*Sticking time*, i.e. the average time that an adsorbed atom spends on the wall before desorbing again.
τ_c	*Correlation time*, i.e. the average time that an adsorbed atom spends on each site of the wall during its surface diffusion process.
τ_f	*Time of flight*, i.e. the average time that an atom is in the gas phase between two wall collisions.
τ_{se}	The average time between two spin exchange collisions.
γ_r	Recombination probability per wall collision.
γ_e	Probability of electron depolarization per wall collision.
γ_z	Probability of nuclear (vector) depolarization per wall collision.
γ_{zz}	Probability of nuclear (tensor) depolarization per wall collision.
R_{jk}	Wall relaxation matrix (see chapter 4.3).
M^i_{jk}	Spin exchange relaxation tensor (see chapter 4.3).

List of Figures

List of Tables

Bibliography

[Abr 58] A. Abragam and J.M. Winter; *Phys. Rev. Lett. Vol. 1* **No. 10** pg. 374 (1958).

[Abr 61] A. Abragam; *The Principles of Nuclear Magnetism*; Oxford At the Clarendon Pres (1961).

[Ack 95] K. Ackerstaff et al.; *HERMES Int. Report* **41** (1995).

[Alb 97] D. Albers et al.; *Phys. Rev. Lett.* **78** pg. 1652 (1997).

[All 72] A.C. Allison; *Phys. Rev.* **A5** pg. 2695 (1972).

[And 63] P.W. Anderson in *Magnetism Vol. I*; G.T. Rado and H. Suhl (Edts.); Academic Press N.Y. (1963).

[Aud 71] C. Audoin et al.; *Adv. in At. and Mol. Phys. Vol. 7*; Academic Press N.Y. (1971).

[Bar 93] D.P. Barber et al.; *Nucl. Instr. Meth.* **A329** pg. 79 (1993).

[Bar 94] D.P. Barber et al.; *Nucl. Instr. Meth.* **A338** pg. 166 (1994).

[Bau 96] C. Baumgarten; *Diploma thesis*; Univ. Hamburg (1996).

[Bau 00] C. Baumgarten; *Ph.D. thesis*; Univ. München (2000).

[Bau 02a] C. Baumgarten et al.; *Eur. Phys. J.* **D18** pg. 37 (2002).

[Bau 02b] C. Baumgarten et al.; *Nucl. Instr. Meth* **A482** pg. 606 (2002).

[Bau 02c] C. Baumgarten et al.; *to be published by Nucl. Instr. Meth* **A** (2002).

[Ber 65] H.C. Berg; *Phys. Rev.* **A137** pg. 1621 (1965).

[Bir 94] G. Bird; *Mol. Gas Dyn. and the Direct Sim. if Gas Flows*; Clarendon Press Oxford (1994).

[Bjo 66] J.D. Bjorken; *Phys. Rev.* **148** pg. 1467 (1966).

[Bjo 70] J.D. Bjorken; *Phys. Rev.* **D1** pg. 1376 (1970).

[Boh 98] J. Boh, G. Eilmsteiner, K.D. Rendulic and A. Winkler; *Surf. Sci.* **395**, pg. 98 (1998).

[Bou 63a] M.A. Bouchiat; *J. Phys. Radium* **24**, pg. 379 (1963).

[Bou 63b] M.A. Bouchiat; *J. Phys. Radium* **24**, pg. 611 (1963).

[Bou 65] M.A. Bouchiat and J. Brossel; *Phys. Rev.* **147**, No. 1 pg. 41 (1965).

[Box 57] G.E.P. Box; *Appl. Statistics* **6** pg. 81 (1957).

[Bur 70] H. Burkhardt and W.N. Cottingham; *Ann. Phys.* **56** pg. 453 (1970).

[Bra 95] B. Braun; *Ph.D. thesis*; Univ. München (1995).

[Brn 92] S. Brandt; *Datenanalyse*; BI-Wissenschaftsverlag (1992).

[Bru 01] I. Brunn; *Diploma thesis*; Univ. Erlangen-Nürnberg (2001).

[Cam 87] J.C. Camparo; *J. Chem. Phys.* **86**, Vol. 3 pg. 1533 (1987).

[Coh 77] C. Cohen-Tannoudji, B. Dui and F. Laloë; *Quantum Mechanics Vol. II* (1977).

[Com 85] G. Comsa and R. David; *Surf. Sci. Rep.* **5** pg. 145 (1985).

[Con 78] H. Conrad, G. Ertl and J. Küppers; *Surf. Sci.* **76** pg. 323 (1978).

[Cou 92] K. Coulter et al.; *Phys. Rev. Lett.* **68** pg. 174 (1992).

[Dal 65] A. Dalgarno and M.R.H. Rudge; *Proc. Roy. Soc.* **A286** pg. 519 (1965).

[Dan 64] J. d'Ans and E. Lax; *Handbook of Chemistry and Physics* **II** pg. 1045 (1964).

[Des 76] M. Desaintfuscien and C. Audoin; *Phys. Rev.* **A13** pg. 2070 (1976).

[Dym 92] A. Dymanus; *Atomic and Molecular Beam Methods Vol. 2*; Oxford University Press (1992).

[E_{142} 93] SLAC E142-Collaboration; *Phys. Rev. Lett.* **71** pg. 959 (1993).

[E_{143} 95] SLAC E143-Collaboration; *Phys. Rev. Lett.* **74** pg. 346 (1995).

[E_{154} 97] SLAC E154-Collaboration; *Phys. Rev. Lett.* **79** pg. 26 (1997).

[E_{155} 98] H. Borel for the SLAC E155-Collaboration; *Proc. Int. Worksh. on DIS and QCD, DIS 98*; World Scientific pg. 346 (1998).

[Ell 74] J. Ellis and R. Jaffe; *Phys. Rev.* **D9** pg. 1444 (1974).

[EMC 88] European Muon Collaboration; *Phys. Lett.* **B206** pg. 364 (1988).

[EMC 89] European Muon Collaboration; *Nucl. Phys.* **B328** pg. 1 (1989).

[Eng 78] T. Engel and G. Ertl; *J. Chem. Phys.* **69** pg. 1267 (1978).

[Ens 02] R. Engels; *Ph.D. thesis*; Univ. Köln (2002).

[Fed 97] J.A. Fedchak et al.; *Nucl. Instr. Meth.* **A391** pg. 405 (1997).

[Fic 55] A.E. Fick; *Ann. Phys.* **94** pg. 59 (1855).

[Fik 71] D. Fick; *Einführung in die Physik mit polarisierten Teilchen*; Vol. 755a, BI Mannheim (1971).

[Fin 75] H.U. Finzel et al.; *Surf. Sci.* **49** pg. 577 (1975).

[Gau 92] H.G. Gaul and E. Steffens; *Nucl. Instr. Meth.* **A316** pg. 297 (1992).

[Ger 21] W. Gerlach and O. Stern; *Z. Physik* **8** pg. 110 (1921).

[God 58] L.J.B. Goldfarb; *Nucl. Phys.* **7** pg. 622 (1958).

[Gol 61] H.M. Goldenberg, D. Kleppner and N.F. Ramsey; *Phys. Rev.* **123** pg. 530 (1961).

[Hae 67] W. Haeberli; *Ann. Rev. Nucl. Sci.* **17** pg. 373 (1967).

[Hal 80] K. Halbach; *Nucl. Instr.* **169** pg. 1 (1980).

[Hel 70] H. Hellwig et al.; *IEEE Trans. Instr. Meas.* **IM19** pg. 200 (1970).

[Hen 98] M. Henoch; *Diploma thesis*; Univ. Münster (1998).

[Hen 02] M. Henoch; *Diploma thesis*; Fern-Univ. Hagen (2002).

[HER 90] HERMES-Collaboration; *HERMES-Proposal* (1990).

[HER 93] HERMES-Collaboration; *HERMES Technical Design Report* (1993).

[HER 98a] HERMES-Collaboration; *Nucl. Instr. Meth.* **A417** pg. 230 (1998).

[HER 98b] HERMES-Collaboration; *Phys. Rev. Lett.* **82** pg. 1164 (1998).

[Hol 94] S. Holloway; *Surf. Sci.* **299/300** pg. 656 (1994).

[Jaf 90] R. Jaffe and A. Manohar; *Nucl. Phys.* **B337** pg. 509 (1990).

[Kin 91a] E.R. Kinney; *Simulations of the Atomic Polarization and Density in the HERMES Polarized Internal Target*; HERMES internal report **3/90** (1991).

[Kin 91b] E.R. Kinney; *Proc. Pol. Gas Targets and Storage Rings*; Heidelberg (1991).

[Kin 93] E.R. Kinney; *Proc. Pol. Ion Sources and Pol. Gas Targets*; Madison (1993).

[Kni 88] R.J. Knize, Z. Wu and W. Happer; *Adv. in At. and Mol. Phys.* Vol. 24; Academic Press N.Y. (1991).

[Knu 09] M. Knudsen; *Ann. Phys.* **28** pg. 999 (1909).

[Knu 15] M. Knudsen; *Ann. Phys.* **48** pg. 1113 (1915).

[Koc 99] N. Koch; *Ph.D. thesis*; Univ. Erlangen-Nürnberg (1999).

[Kol 98] H. Kolster; *Ph.D. thesis*; Univ. München (1998).

[Kor 90] W. Korsch; *Ph.D. thesis*; Univ. Bonn (1990).

[Kui 91] E.W. Kuipers et al.; *Phys. Rev. Lett.* **66** pg. 116 (1991).

[Kus 59] P. Kusch and V.W. Hughes; *Handbuch der Physik*; **37/1**, Springer-Verlag, Berlin (1959).

[Lem 93] S.K. Lemieux, T.B. Clegg, H.J. Karwowski and W.J. Thompson; *Nucl. Instr. Meth.* **A333** pg. 434 (1993).

[Len 02] P. Lenisa; *private communication* (2002).

[Lev 88] C.D.P. Levy and P.W. Schmor; *J. Appl. Phys.* **63**, No. 10 pg. 4819 (1988).

[Loz 93] B. Lorentz; *Diploma thesis*; Univ. Heidelberg (1993).

[Lor 97] W. Lorenzon; *7th Int. Workshop on Pol. Gas Targets and Pol. Beams*; AIP Conf. Proc. pg. 181; Urbana-Champaign (1997).

[Mas 34] H.S.W. Massey and C.B.O. Mohr; *Proc. Roy. Soc.* **A144** pg. 188 (1934).

[Mei 92] H.H. Meinke and F.W. Gundlach; *Pocketbook of high frequency technology* 5th release, ISBN 3-540-54717-7, Springer-Verlag, Berlin (1992).

[Mey 98] H.O. Meyer et al.; *Phys. Rev. Lett.* **81** pg. 3096 (1998).

[Nas 02] A. Nass; *Ph.D. thesis*; Univ. Erlangen-Nürnberg (2002).

[Oh 70] Saewoong Oh; *Nucl. Instr.* **82** pg. 189 (1970).

[Phi 87] R.J. Philpott; *Nucl. Instr. Meth.* **A259** pg. 317 (1987).

[Pri 93] J.S. Price and W. Haeberli; *Nucl. Instr. Meth.* **A326** pg. 416 (1993).

[Pri 94] J.S. Price and W. Haeberli; *Nucl. Instr. Meth.* **A349** pg. 321 (1994).

[Prz 98] B. v. Przewoski et al.; *Phys. Rev.* **C58** pg. 1897 (1998).

[Pur 56] E.M. Purcell and G.B. Fields; *Astrophys. J.* **124** pg. 542 (1956).

[Rab 39] I.I. Rabi et al.; *Phys. Rev.* **55** pg. 526 (1939).

[Rap 65] D. Rapp and P.E. Golden; *J. Chem. Phys.* **43** pg. 1464 (1965).

[Rat 98] F. Rathmann et al.; *Phys. Rev.* **C58** pg. 658 (1998).

[Ret 92] C.T. Rettner; *Phys. Rev. Lett.* **69** pg. 383 (1992).

[Sch 91] P. Schiemenz, A. Ross and G. Graw; *Nucl. Instr. Meth.* **A305** pg. 15 (1991).

[Sha 87] M.B. Shah, D.S. Elliott and H.B. Gilbody; *J. Phys.* **B20** pg. 3501 (1987).

[SMC 94a] Spin Muon Collaboration; *Phys. Lett.* **B329** pg. 399 (1994).

[SMC 94b] Spin Muon Collaboration; *Phys. Lett.* **B336** pg. 125 (1994).

[SMC 97a] Spin Muon Collaboration; *Phys. Lett.* **B396** pg. 338 (1997).

[SMC 97b] Spin Muon Collaboration; *Phys. Rev.* **D56** pg. 5330 (1997).

[Sok 64] A.A. Sokolov and I.M. Ternov; *Sov. Phys. Docl.* **8** pg. 1203 (1964).

[Spe 62] W. Spendley, G.R. Hext and F.R. Himsworth; *Technometrics* **4** pg. 441 (1962).

[Ste 94] M. Stephens, R. Rhodes and C. Wieman; *J. Appl. Phys.* **76**, Vol. 6 pg. 3479 (1994).

[Stn 95] J. Stenger; *Ph.D. thesis*; Univ. Erlangen-Nürnberg (1995).

[Sto 94] F. Stock et al.; *Nucl. Instr. Meth.* **A343** pg. 334 (1994).

[Stw 95] J. Stewart; *6th Int. Workshop on Pol. Gas Targets and Pol. Beams*; Cologne (1995); World Scientific (1996).

[Stw 97] J. Stewart; *7th Int. Workshop on Pol. Gas Targets and Pol. Beams*; AIP Conf. Proc. 421 pg. 69; Urbana-Champaign (1997).

[Swe 85] D.R. Swenson, D.Tupa and L.W. Anderson; *J. Phys. B: At. Mol. Phys.* **18** pg. 4433 (1985).

[Swe 88] D.R. Swenson and L.W. Anderson; *Nucl. Instr. Meth.* **B29** pg. 627 (1988).

[Tho 87] G.E. Thomas et al.; *Nucl. Instr. Meth.* **A257** pg. 32 (1987).

[vBr 97] J.F.J van den Brand et al.; *Phys. Rev. Lett.* **78** pg. 1235 (1997).

[Wal 93] T. Walker and L.W. Anderson; *Nucl. Instr. Meth.* **A334** pg. 313 (1993).

[Wan 95] W. Wander et al.; *HERMES Int. Report* **40** (1995).

[Wei 98] C. Weiskopf; *Diploma thesis*; Univ. Erlangen-Nürnberg (1998).

[Wis 64] H. Wise, C.M. Ablow and K.M. Sancier; *Chem. Phys.* **44** pg. 3569 (1964).

[Wie 01] T. Wise et al.; *Phys. Rev. Lett.* **87** pg. 3569 (2001).

[Wit 56] J.P Wittke and R.H. Dicke; *Phys. Rev.* **103** pg. 620 (1956).

[Wlt 91] F.H. Walters, S.L. Morgan, L.R. Parker and S.N. Deming; *Sequential Simplex Optimization*; CRC Press LLC, Boca Raton (1991).

[Zel 86] A.N. Zelenski, S.A. Kokhanovskii, V.M. Lobashev and V.G. Polushkin; *Nucl. Instr. Meth.* **A245** pg. 223 (1986).

Acknowledgements

Preparing a doctoral thesis is a challenging and fascinating but also time consuming and sometimes even stressful task. Fortunately, the physics at the HERMES experiment is very much a team effort. Thus I want to express my gratefulness to all the collaborators, too many to mention individually, for creating a friendly working atmosphere with many possibilities for physical discussion and advice.

I am particularly thankful to my supervisor, Prof. Dr. E. Steffens from the University of Erlangen–Nürnberg, for providing me with his confidence and support throughout the past years, during which his advice and experience has in many discussions proven to be very fruitful. Besides supporting me in matters of physics he often went well beyond his call of duty to help me with the adminstrative problems I encountered within the seemingly infinite meander of bureaucracy. For the proofreading of this work I express my gratitude to Prof. Dr. E. Steffens and to P. Tait whose linguistic profiency has been of great help.

This thesis owes an additional great debt to Dr. C. Baumgarten and Dr. B. Braun who took their time out to explain things rather detailed to me and have usually been patient with my stupid questions. Both set – with their PhD theses – a basis that I could enhance for the presented work.

Thanks to the complete list of target group members during my (already) 5 years with the HERMES experiment for the group cohesion and the nice atmosphere. Another big thankyou to the crew which tried to keep the disorder of the data aquisition system controllable.

Thanks to all the people who made my time in Erlangen enjoyable. I am grateful for the possibilities to teach physics within the scopes of the laboratories and to supervise I. Brunn as a diploma student.

Thanks to all the companions in building 55a for the coffee and the laughter. Finally, I would like to thank D. Adams for the fish.

I want to dedicate this thesis to my wife Nina and my son Nicolas. Thank you for the vitally important love, trust, distraction and motivation you gave me.